INAUGURAL - DISSERTATION

zur

Erlangung der Doktorwürde

der

Naturwissenschaftlich-Mathematischen
Gesamtfakultät

der

Ruprecht-Karls-Universität
Heidelberg

vorgelegt von

Dipl.-Phys. Swen Schuster
aus Sindelfingen

Tag der mündlichen Prüfung: 3. November 2015

Work Function Tuning at Interfaces by Monomolecular Films

Gutachter:

Prof. Dr. Michael Zharnikov

Prof. Dr. Petra Tegeder

“Everything should be made as simple as possible, but not one bit simpler.”

Albert Einstein

Zusammenfassung

Die Kontrolle der Austrittsarbeit von Oberflächen und Grenzflächen gehört zu den wichtigsten Aspekten der modernen Oberflächenphysik und Nanotechnologie, z.B. in Bezug zur organischen Elektronik und Photovoltaik. Das Ziel dieser Arbeit war es, neue Wege zu finden, um die Austrittsarbeit von Metalloberflächen unter Verwendung von molekularer selbstorganisierender Filme zu steuern. Um dies zu erreichen, wurden zwei Strategien angewandt. Die erste Strategie war es, aliphatische und aromatische Moleküle zu verwenden, die einen eingebetteten Dipol (Funktionalisierung innerhalb des Molekülgerüsts) enthalten. Die sogenannten selbstorganisierten Monoschichten (SAMs) ermöglichen es, die Austrittsarbeit des Substrats zu kontrollieren, unabhängig von der Art der Adsorption der Moleküle, und, was am wichtigsten ist, ohne Modifikation der Grenzfläche. Im Falle von aliphatischen Filmen verwendeten wir Alkanthiole mit einem eingebetteten Ester-Dipol, wobei die Länge des oberen und unteren Segments sowie der Richtung des eingebetteten Dipols variiert werden kann. Im Fall von aromatischen Systemen verwendeten wir auf Terphenyl basierende Moleküle mit einer eingebetteten Pyrimidin-Funktionalisierung, wobei die Richtung des Dipols geändert werden kann. Die elektronischen und strukturellen Eigenschaften dieser Monolagen wurden unter Verwendung einer Reihe von komplementären Charakterisierungsmethoden analysiert (in Kombination mit quantenmechanischer Modellierung). Ergebnisse zeigen, dass solche Monoschichten, aus anwendungsspezifischen Gesichtspunkten betrachtet, grundsätzlich sehr interessant sind, da es sich gezeigt hat, dass die eingebetteten Dipole eine mögliche Diskontinuität innerhalb der Monoschicht, und damit auch eine elektrostatische Verschiebung der Bindungsenergien in den Bereichen ober- und unterhalb der Dipole relativ zueinander verursachen. Besonders wichtig ist (in Zusammenhang mit der vorliegenden Arbeit) die Tatsache, dass die Monolagen, welche eingebettete Funktionalisierungen beinhalten, gut geeignet sind, um die Austrittsarbeit von Metalloberflächen zu kontrollieren. In der zweiten Strategie verwendeten wir mit Azobenzol (AZO) funktionalisierte Alkanthiole mit einer speziell entwickelten Architektur, welche die Variation der Packungsdichte und eine zusätzliche Funktionalisierung ermöglicht. Diese neuen SAMs wurden mithilfe spektroskopischer und mikroskopischer Techniken untersucht. Photoisomerisierungsexperimente zeigten eine reproduzierbare

Änderung der Austrittsarbeit, welche in gewissem Maße durch die starke sterische Hinderung eingeschränkt wurde. Um diesen Effekt zu verringern, wurden die Azobenzol-Moleküle mit kurzen Spacer-Molekülen verdünnt, was zu einer Verbesserung der Schalter-Eigenschaften der Azobenzol-Moleküle führte.

Abstract

The control over the work function of surfaces and interfaces is one of the most important issues of modern surface science and nanotechnology, e.g. in context of organic electronics and photovoltaics. The goal of this work was to look for new ways to control the work function of metal substrates by using molecular self-assembly. Two different strategies were used. The first strategy was to use aliphatic and aromatic molecules which contain an embedded dipolar group (mid-chain functionalization). Such self-assembled monolayers (SAMs) allow for tuning the substrate work function in a controlled manner, independent of the docking chemistry and, most importantly, without modifying the SAM-ambient interface. In the case of aliphatic films, we used alkanethiols functionalized with an embedded ester dipole, with the length of both top and bottom segments as well as the direction of the embedded dipole being varied. In the case of aromatic systems, we used terphenyl based thiols functionalized with an embedded pyrimidine dipolar group, with the direction of the dipole being varied. The electronic and structural properties of these embedded-dipole SAMs were thoroughly analyzed using a number of complementary characterization techniques combined with quantum-mechanical modeling. It is shown that such mid-chain-substituted monolayers are highly interesting from both fundamental and application viewpoints, as the dipolar groups are found to induce a potential discontinuity inside the monolayer, electrostatically shifting the core-level energies in the regions above and below the dipoles relative to one another. Particularly imptortant, in context of the present work, is the fact that the mid-chain functionalized films are indeed well suited to adjust the work function of metal substrates. This could be e.g. done by varying the orientation of the dipolar group but also by mixing the molecules with differently oriented dipoles as was demonstrated in the present work. Within the second strategy, we used photoresponsive systems, viz. azobenzene substituted alkanethiols, having a specially designed architecture to control the packing density and carrying an additional dipolar tail group. These novel SAMs were studied in detail by using spectroscopic and microscopic techniques. Performing photoisomerization experiments we obtained a reproducible, stimuli-responsive change in the work function which was, however, limited to some extent due to the strong steric hindrance effects. In order to reduce these effects, we diluted the azobenzene molecules with short spacer molecules, which resulted in an improvement in the photoswitching behavior.

Contents

Zusammenfassung iii

Abstract v

Contents vii

List of Figures xi

List of Tables xiii

Abbreviations xv

Physical Constants xvii

Symbols xix

1 Introduction 1

2 Theoretical Basics and Background 9
- 2.1 Characterization methods . . . 9
  - 2.1.1 X-ray photoelectron spectroscopy (XPS) . . . 9
  - 2.1.2 Near-edge X-ray absorption fine-structure spectroscopy . . . 13
  - 2.1.3 Kelvin Probe . . . 17
  - 2.1.4 Ultraviolet photoelectron spectroscopy (UPS) . . . 19
- 2.2 Self-assembled monolayers . . . 20
  - 2.2.1 Odd-even effect . . . 21
- 2.3 Molecular dipole and work function . . . 23
- 2.4 Photoisomerization . . . 23
  - 2.4.1 Work function change . . . 23

3 Materials and Methods 25
- 3.1 Compounds and Chemicals . . . 25
  - 3.1.1 Embedded Ester . . . 25
  - 3.1.2 Embedded pyrmidine . . . 25
  - 3.1.3 Azobenzenealkanethiols . . . 26

3.2 Preparation of the SAMs . . . 27
  3.2.1 Embedded ester . . . 27
  3.2.2 Embedded pyrmimidine . . . 28
  3.2.3 Embedded pyrimidine mixed films . . . 28
  3.2.4 Azobenzenealkanethiols . . . 28
  3.2.5 Azobenzenealkanethiols diluted with spacer molecules . . . 28
3.3 Characterization of the SAMs . . . 29
  3.3.1 XPS and HRXPS . . . 30
  3.3.2 NEXAFS spectroscopy . . . 31
  3.3.3 Determination of the work function . . . 31
3.4 Photoisomerization experiments . . . 32
  3.4.1 Photoisomerization of H-azo-Cn . . . 32

4 Results and Discussion **35**
4.1 Embedded dipoles in aliphatic self-assembled monolayers . . . 35
  4.1.1 Basic characterization . . . 35
  4.1.2 Electrostatic effects . . . 37
    4.1.2.1 Photoemission . . . 37
      Binding energy shift . . . 37
      Variation of the bottom segment . . . 39
      Variation of the top segment . . . 41
      Inversion of the dipole direction . . . 41
    4.1.2.2 Work function . . . 43
  4.1.3 Theoretical calculations . . . 44
    4.1.3.1 C 1s core level energies . . . 45
    4.1.3.2 Electrostatic potential . . . 45
    4.1.3.3 Comparison to the experimental results . . . 46
4.2 Embedded dipoles in aromatic self-assembled monolayers . . . 47
  4.2.1 Basic characterization . . . 47
    4.2.1.1 XPS and HRXPS . . . 47
    4.2.1.2 NEXAFS spectroscopy . . . 49
    4.2.1.3 Additional characterization . . . 52
  4.2.2 Electrostatic effects . . . 53
    4.2.2.1 Photoemission . . . 53
    4.2.2.2 Work function . . . 55
    4.2.2.3 Band-Structure-Calculations . . . 56
  4.2.3 Mixed films . . . 59
  4.2.4 Discussion . . . 60
4.3 Azobenzene-Substituted Alkanethiolate Self-Assembled Monolayers 65
  4.3.1 High-Resolution X-ray Photoelectron Spectroscopy . . . 65
  4.3.2 NEXAFS Spectroscopy . . . 66
  4.3.3 Scanning tunneling microscopy . . . 71
  4.3.4 SAMs on Ag(111) . . . 71
4.4 Photoisomerization . . . 72

4.4.1 H-azo-C3/C4 . . . 72
4.4.2 H-azo-C3/C4 diluted with the spacer molecules . . . 73
4.4.2.1 Short alkanethiols . . . 73
4.4.2.2 Phenylthiol . . . 74
4.4.2.3 WF change vs. concentration . . . 75
4.4.3 CH_3-azo-C3/C4 . . . 76
4.4.4 CH_3-azo-C3/C4 diluted with spacer molecules . . . 78
4.4.4.1 WF change vs. concentration . . . 79
4.4.5 Discussion . . . 80

5 Conclusions **81**

A Additional Data **85**
A.1 Reference HRXPS data for 2-MPM . . . 85

B Experimental Setups **87**
B.1 Kelvin Probe . . . 87
B.2 LED irradiation setup . . . 89

C Lists **91**
C.1 List of Publications . . . 91
C.2 List of conference contributions . . . 92

Bibliography **95**

Acknowledgements **113**

List of Figures

1.1 Embedded ester dipole . . . 3
1.2 Schematic drawing of TP1-n molecules . . . 5
1.3 Azobenzene alkanethiols functional groups . . . 6

2.1 XPS energy scheme . . . 10
2.2 NEXAFS molecular potential . . . 14
2.3 Orbitals described by a vector or a plane . . . 17
2.4 Schematic diagram of Kelvin Probe physics . . . 18
2.5 Schematic energy diagrams . . . 19
2.6 UP spectrum of Au surface . . . 20
2.7 Schematic diagram of ideal SAM on a gold single crystal . . . 21
2.8 Illustration of the odd-even effect . . . 22
2.9 Azobenzene molecule . . . 23
2.10 H-azo conformation change . . . 24

3.1 Synthesis of TP1-n thiolates . . . 27
3.2 Preparation of H-azo-Cn mixed with spacer molecules . . . 29
3.3 Spacer molecules . . . 29
3.4 Schematic drawing of H-azo-Cn diluted with AT . . . 33
3.5 Schematic drawing of H-azo-Cn diluted with PT . . . 33

4.1 IR spectra and best fit simulations . . . 36
4.2 AFM images of the C10EC10 and C10E*C10 . . . 37
4.3 C10C10 Ester SAM . . . 38
4.4 HRXPS peak fit components . . . 38
4.5 C 1s HRXP spectra of CXEC5 . . . 39
4.6 C 1s HRXP spectra of CXEC10 . . . 40
4.7 C 1s HRXP spectra of CXEC1 . . . 40
4.8 C 1s HRXP specrta of C10ECX . . . 41
4.9 C 1s HRXP spectra of C15ECX . . . 42
4.10 C 1s HRXP spectra of C10EC10, C10EC10 rev. and C16 ref. . . . 43
4.11 Work function data of embedded ester SAMs . . . 44
4.12 C 1s core level energies of C10EC10 and C10EC10 reverse . . . 45
4.13 Electrostatic potential of C10EC10 and C10EC10 reverse . . . 46
4.14 HRXP spectra of TP1-n SAMs . . . 48
4.15 NEXAFS spectra of TP1-n . . . 50

4.16 C 1s HRXP spectra of TP1-n SAMs 54
4.17 Work function of TP1-n SAMs 56
4.18 Band structure calculations of TP1-n SAMs 58
4.19 Work function of TP1-up/down mixed films 60
4.20 HRXP spectra of the TP1-up/down mixed films 61
4.21 HRXP spectra of H-AZO 66
4.22 NEXAFS C K-edge spectra of H-AZO 67
4.23 N K-edge NEXAFS spectra of H-AZO 68
4.24 Scheme of H-azo-C3 molecule orientation 69
4.25 HRXP and NEXAFS spectra of H-AZO on Ag 72
4.26 H-azo-Cn isomerization and WF change 74
4.27 Azobenze alkanethiols in C8 matrix WF change 75
4.28 Azobenze alkanethiols in PT matrix WF change 76
4.29 Azobenzene alkanethiols WF vs conc. 77
4.30 CH_3-azo-Cn 77
4.31 CH_3-azo-Cn in PT matrix 78
4.32 CH_3-azo-Cn WF vs. conc. 79

A.1 Schematic drawing of 2-MPM 85
A.2 HRXP spectra of the 2-MPM SAM 86

B.1 UHV Kelvin Probe 87
B.2 UHV Kelvin Probe 87
B.3 Schematic drawing of Kelvin Probe principles 88
B.4 LED setup 89
B.5 LED lamps 89

List of Tables

3.1 Ester compunds 26

4.1 WF and BE shifts 47
4.2 TP1-n thickness and packing density 49
4.3 Work function values of TP1-n SAMs 56
4.4 Properties of H-AZO molecules on Au and Ag 70

Abbreviations

SAM	**S**elf-**A**ssembled **M**onolayer
AZO	**Azo**benzene
AT	**A**lkane**t**hiol
HDT	**H**exa**d**ecane**t**hiol
PT	**P**henyl**t**hiol
TPT	**T**er**p**henyl**t**hiol
EtOH	**Et**hanol
THF	**T**etra**h**ydro**f**uran
XPS	**X**-ray **P**hotoelectron **S**pectroscopy
HRXPS	**H**igh **R**esolution **XPS**
NEXAFS	**N**ear **E**dge **X**-ray **A**bsorption **F**ine **S**tructure
IRRAS	**I**nfra**r**ed **R**eflection **A**bsorption **S**pectroscopy
AFM	**A**tomic **F**orce **M**icroscopy
STM	**S**canning **T**unneling **M**icroscopy
UHV	**U**ltra **H**igh **V**acuum
KP	**K**elvin **P**robe
WF	**W**ork **F**unction
CPD	**C**ontact **P**otential **D**ifference
BE	**B**inding **E**nergy
KE	**K**inetic **E**nergy
PE	**P**hoton **E**nergy
DFT	**D**ensity **F**unctional **T**heory
DOS	**D**ensity **o**f **S**tates

Physical Constants

Elementary charge	e	$=$	$1.602\ 176\ 565\ 35 \times 10^{-19}$ C
Planck constant	h	$=$	$6.626\ 069\ 572\ 9 \times 10^{-34}$ Js
Dirac constant	$\hbar$	$=$	$1.054\ 571\ 726\ 47 \times 10^{-26}$ Js
Permittivity (vacuum)	ε_0	$=$	$8.854\ 187\ 817\ 6.. \times 10^{-12}$ Fm^{-1}
Permittivity (relative)	ε_r		

Symbols

P	Surfce power density	W/cm^2
E_P	Photon energy	eV
E_B	Binding energy	eV
E_K	Kinetic energy	eV
E_F	Fermi energy	eV
Φ	Work function	eV
$\Delta\Phi$	Relative work function	eV
$\vec{\mu}$	Dipole moment	D
λ	Attenuation length	Å
d	Film thickness	Å
θ	Incidence angle	$^\circ$
α	Tilt angle	$^\circ$
γ	Twist angle	$^\circ$

Meinen Eltern

Chapter 1

Introduction

The control of physical and chemical properties of surfaces and interfaces is one of the most important issues of modern surface science, physical chemistry, and nanotechnology. Highly relevant systems in this context are self-assembled monolayers (SAMs), which are 2D polycrystalline films of semi-rigid molecules that are chemically anchored to a substrate by a suitable head group [1, 2]. These systems have attracted considerable interest for more than three decades [3]. They have been used, e.g., for controlling wettability [4, 5], cell adhesion [6, 7], and for corrosion protection [8, 9]. They have also attracted considerable attention in the area of organic electronics, where they are, in particular, used to modify gate dielectrics in organic transistors to enhance their performance [10–12], to realize devices with novel functionalities like memories [13] or sensors [14], or even to act as the active layer of the device [15]. When bonded to electrodes, SAMs can be used to manipulate charge carrier injection barriers, to provide a better electronic coupling, and/or to act as an intermediate layer for the growth of the active organic material [16–23]. The key issues in this context are (i) the conductive properties of the SAM itself, affecting the performance of the entire device, (ii) control of the SAM-ambient interface, defining the nucleation and growth mode of the organic semiconductor, and (iii) introduction of a specific dipole moment to manipulate charge carrier injection barriers. So far, characteristics of the SAM-ambient interface and adjustment of dipole moment were entangled since the common way to manipulate the entire electrostatic parameters of SAMs is the selection of a proper dipolar terminal tail group comprising the SAM-ambient interface [24, 25]. This strategy, however, also affects the nucleation chemistry, making optimization of a particular system a highly difficult task. While a system has recently been reported in which the mixing of two different, short molecules with almost opposing dipole moments led to layers with an adjustable dipole moment and unaltered surface energy[22], a more general solution to this dilemma would be the incorporation of a suitable functional group into the backbone of the molecules forming the SAM such that a layer with buried dipole moments can be realized. This leaves open options for the independent optimization of the SAM-ambient interface, e.g., via suitable tail-group substitutions. Thus, the interfacial dipole and nucleation chemistry can be tuned separately, making it highly interesting for applications, e.g. when the SAM is used as intermediate, charge-injection promoting layer between a metal electrode and adjacent organic electronic material. In addition, one avoids potentially reactive functional groups at the exterior of the SAM that could be chemically modified during the growth of an organic film, which is clearly of advantage for the stability of the entire system. Beyond these practically relevant aspects, embedded groups can be used to introduce deliberately chosen chemical and physical perturbations within the monolayer. The extent of these perturbations can be precisely controlled by selectively choosing the functional dipolar moieties and the positions and orientations in which they are introduced within the chain. This opens up new and unique avenues for investigating fundamental aspects of SAM electrostatics and for designing SAMs with desired properties. Embedding functional groups into SAMs has been a widely used strategy for obtaining additional functionalities, such as preferred cleaving [26–28] or providing (switchable) molecular dipole moments [29]. In addition, these groups also had significant influence on the layer order, either by steric constraints [26, 27, 29] or by formation of intermolecular hydrogen bonds [29].

Recently, as a first attempt to build a system with embedded dipoles, ester groups, R-(C=O)-O-R, were introduced into the alkanethiolate molecules on gold as a representative test case [30]. In this system as, shown in Figure 1.1, indeed a variety of novel phenomena have been observed. From a fundamental point of view, the most interesting observation was a strong electrostatic effect in the X-ray photoelectron spectra. In the presence of embedded esters, the C 1s photoelectron kinetic energies were found to be consistently shifted by 0.85 eV between the chemically identical -(CH_2)- alkyl segments above and below the ester moiety, regardless of the relative lengths of the segments. This shift correlates well with simple electrostatic estimates based on dipole moment of the ester groups at their orientation in the SAMs. Significantly, this observation, along with few others [31–34], contradicts the generally accepted assumption that the photoemission spectra

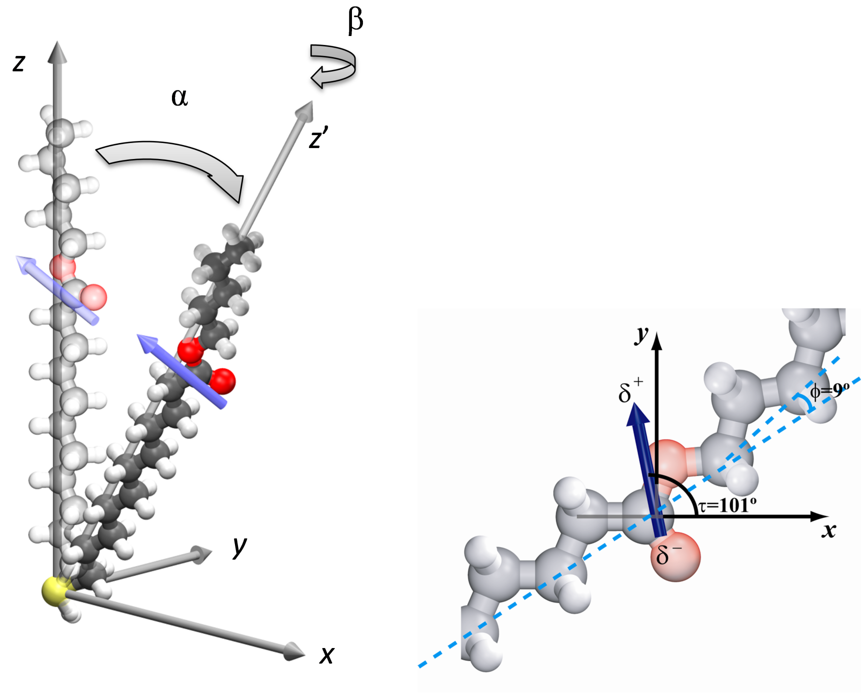

(a) Embedded ester alkanethiol (b) Ester dipole

FIGURE 1.1: Schematic drawing of (a) the mid-chain ester functionalized alkanethiol [having variations in bottom and top segments] and of (b) the ester dipole [30].

of SAMs can be described entirely within the general concept of a chemical shift [35].

As will be discussed in more detail below, this would indeed be the case for conductive samples but not for relatively poorly conductive organic layers of upright ”standing” molecules that are in the focus of the present study. Further, it suggests that the electronic levels and the electrostatic potential distribution within a SAM can be controlled to a certain extent by the introduction of an embedded dipole layer.

To prove a generality of this concept and also in view of the theoretical predictions [36], we designed and studied aromatic SAMs that contain an embedded dipolar functional group. Note that aromatic monolayers are superior to aliphatic ones in terms of electrical conductance [37–39], which makes them more suitable intermediate layers in organic electronics and photovoltaics assemblies. Also, these films are better suited as interfacial layers for the deposition of most organic semiconductors, which generally contain aromatic functional units [40]. Here, we report a rational approach for adjusting the dipole moments without significantly altering the molecular structure or the interface chemistry. Starting from terphenyl-4-methanethiol C_6H_5-C_6H_4-C_6H_4-CH_2-SH (TP1), the monolayers of which on Au(111) are well-investigated [41–45], we substituted the central phenylene ring by a 2,5-pyrimidine group, in the two possible orientations (Figure 1.2). Since the pyrimidine group has a noticeable dipole moment (2.3 D) [46, 47], this architecture allows for an arrangement of embedded dipoles pointing either upwards or downwards with respect to the substrate, assuming an upright molecular orientation. These SAM precursors are accordingly denoted as TP1-up and TP1-down, as shown in Figure 1.2. Their respective SAMs were characterized in detail by a number of complementary surface-analytical techniques, viz. X-ray photoelectron spectroscopy (XPS), high-resolution XPS (HRXPS), ellipsometry, infrared reflection absorption spectroscopy (IRRAS), near-edge X-ray absorption fine structure (NEXAFS) spectroscopy, and scanning tunneling microscopy (STM), to study the effect of embedded dipoles on the molecular organization and to ensure film quality and, thus, the reliability of our conclusions regarding the specific electrostatic effects of embedded dipoles. The latter effects were addressed by dedicated experimental tools and theoretical simulations. Further in view of the results for the TP1-up/down system, we have revisited the ester-based aliphatic films (see Figure 1.1) extending the range of the SAM precursors, studying the effect of the embedded ester on the work function, and combining the experimental results with the theory.

In addition to the embedded dipole strategy, we tried to design molecular films to control the work function dynamically, following an external stimulus. As such systems azobenzene-functionalized alkanethiols were used, carrying dipolar functional groups and having a variable length of the aliphatic linker between the thiol anchor a photoresponsive moiety. This moiety is much more attractive in context of stimuli-responsive systems and potential applications in molecular electronics - as far as azobenzene-bearing molecules can be assembled on a solid substrate in a suitable fashion, in view of its well-known photochromic behavior [48, 49] via light-induced *trans-cis* conformational changes. Along these lines, a variety of azobenzene functionalized thiol SAMs were studied, including purely aromatic monolayers based on biphenyl azobenzene [50–56], hybrid aliphatic-aromatic films [57–59] as well as mixed SAMs comprized of azobenzene functionalized molecules and short ”matrix” moieties [60–63]. The reason for the use of such mixed SAMs with the functional molecules “diluted” by the matrix molecules is to release possible steric hindrances imposed by the neighbor molecules in the densely packed films,

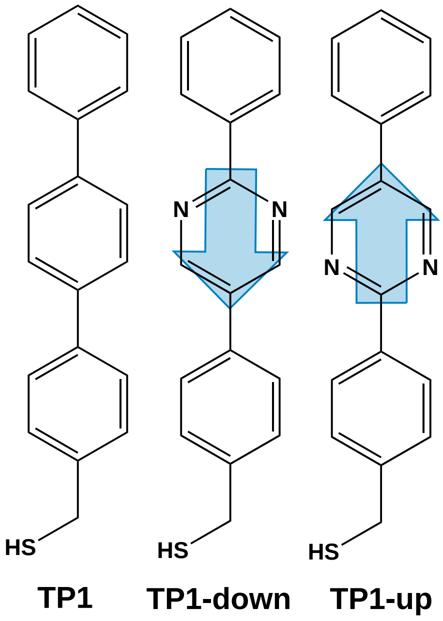

FIGURE 1.2: A schematic drawing of the pyrimidine-substituted molecules and major reference molecule along with their acronyms. The directions of the dipole moment associated with the embedded pyrimidine group are shown (the direction from the negative charge to the positive charge is considered as positive). The molecules are named accordingly. Individual rings will be named as ambient-adjacent, central, and substrate-adjacent ones, assuming an upright molecular geometry.

limiting the conformational transformations of the azobenzene units. Such steric hindrances are believed to be the major constraint preventing the fabrication of reliable, stimuli-responsive, azobenzene-based monolayers, along with the quenching of the isomerization-active, excited state by interaction with the substrate or excitonic coupling among the azobenzene chromophores, discussed also in this context. However, it has been demonstrated that for certain azobenzene-based SAMs, viz. for those with the rigid aromatic backbone biphenyl quite effective photoisomerization [50–55] is possible even for well-ordered and densely packed structure, due to a cooperative character of the switching process occurring, presumably, in a domino-like fashion [50–56]. Such strategy, relying on cooperative switching in well ordered densely packed films rather than that of isolated azobenzene-bearing molecules, implanted in an inert matrix, should be of course more efficient. The question is of course whether the observed cooperative isomerization behavior is a broad phenomenon for ordered molecular films or rather an exception, characteristic of specific molecular arrangement in few selected cases only. In contrast to the SAMs based on rigid, oligophenyl backbone with embedded azobenzene moiety [50, 56], the structural order of monolayers, where this moiety is linked

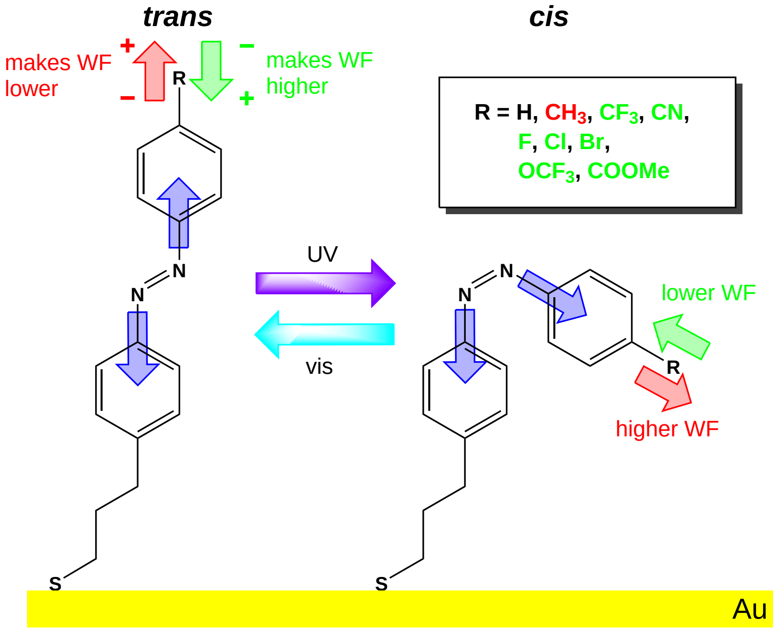

FIGURE 1.3: Azobenzene alkanethiols functional groups

to the thiol group via an aliphatic chain [58, 64] is usually much lower. In particular, this lack of the structural order is associated with much smaller changes in the work function upon the isomerization of such SAMs [57] as compared to those with the oligophenyl backbone [51]. Significantly - in context of the present study, poor structural quality of the SAMs where aliphatic chain is used to link azobenzene moiety to the substrate makes an impression that the odd-even effects characteristic of the biphenyl and terphenyl substitutions and having, at a proper n, positive effect on the film structure [45, 65–77] do not occur in azobenzene-bearing alkanethiol (AT) monolayers. However, there are two important aspects which question this seeming impression. First, in most cases addressed so far, alkyl chain was linked to azobenzene moiety not directly, as in the previous studies with biphenyl or therphenyl substitution, but via either ether [57, 58, 60–63] or the amide [59, 64] group which could distort the all-trans conformation, essential for the odd-even effects. Therefore, in the present study, we eliminate the above limitations and investigate the structure of SAMs where alkyl linker is short enough and directly attached to the azobenzene moiety, viz. monolayers formed from C_6H_4-N-N-C_6H_4-$(CH_2)_n$-SH (AZO-n)at $n = 3$ and 4 (see Figure 1.3). By performing structural analysis and stability tests for these SAMs on the Au(111) and the Ag(111) substrates we prove the applicability of the odd-even effect concept to azobenzene-substituted monolayers, with a particular emphasis on the possibility to form highly ordered molecular films.

The work presented in this thesis was a part of large collaboration projects, involving several experimental and theoretical groups. Our part was a general design of the system studied as well as X-ray spectroscopic and work function measurements on these systems.

The presented results from atomic force microscopy (AFM), scanning tunneling microscopy (STM), infrared reflection absorption spectroscopy (IRRAS), ellipsometry measurements and theoretical calculations (and simulations) were provided by our partner groups. Also the synthesis of the SAM precursors was performed by our partners.

Chapter 2

Theoretical Basics and Background

2.1 Characterization methods

2.1.1 X-ray photoelectron spectroscopy (XPS)

X-ray photoelectron spectroscopy (XPS) as surface analytical method provides the detection of all chemical elements (except hydrogen) from a concentration of about 1%. It also provides information on the chemical environment, bonding and oxidation state of the elements [78, 79]. This method is of great importance for determining the constitution of compounds in the outer surfaces of solids, e.g. to identify the type and thickness of corrosion layers to investigate solid catalysts, passivation phenomena, adsorption effects and processes in the surface treatment. XPS is based on the photoelectric effect. Accordingly, an electron of a certain binding energy E_b absorbs a photon of the energy $E_p = h\nu$ and is emitted with the kinteic energy E_k.

$$E_k = h\nu - E_b - \Phi_A \tag{2.1}$$

The kinetic energy E_k which is measrued by the analyzer and is independent from the work function of the sample (Φ_S); ϕ_A is the work function of the analyzer which is different from the work function of the sample. Due to the fact that the analyzer is electrically connected to the sample itself, the common Fermi level E_F is the only suitable reference system for the binding energies. The binding energies

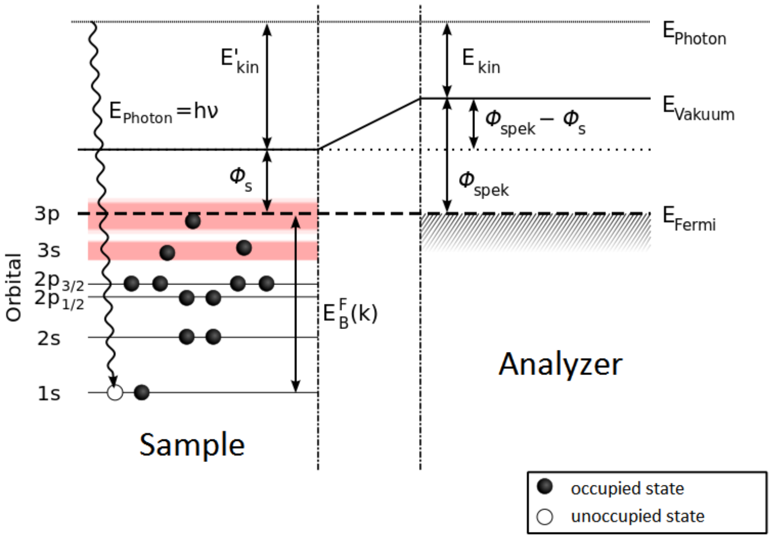

FIGURE 2.1: Energetic scheme of photoelectron spectroscopy

of the core levels of interest are determined by comparing their position to the one of Au $4f_{7/2}$, as well as their known binding energy of $E_b^{Au} = E^{Au} - E_F \approx 84$ eV [67, 80, 81].

$$E_b = E_b^{Au} + (E_k^{Au} - E_k) \tag{2.2}$$

Line shape The finite core hole level life times create a Lorentz shaped broadening of the XPS lines. Aditionally, a broadening is caused by low energy vibrational excitations and the instrument function of light source and analyzer (this kind of broadening can be fitted by using Gauß curves). Due to this XPS peaks are fitted by using a Voigt profile (a combination of Gauß and Lorentz functions to reproduce broadenings in XP spectra). The contribution of inelstically scattered electrons can be expressed by using a Shirley background [82]. Binding energies are specific for each element. The effects of initial and final state, e.g. chemical shifts due to electronegative binding partners and the shielding of the core hole, depending on the electronic environment respectively lead to variations of the binding energy of an element of several eV. Once the power of the final states is known, the chemical composition of the sample can be determined from the shift of the XP lines. The determination of the chemical composition of the sample is called electron spectroscopy for chemical analysis (ESCA).

Shake-up energy loss In case of shake-up processes the valence electron receives only a part of the photon energy and it is excited to an unoccupied state. The kinetic energy of the emitted electron and with this the transition energy between occupied and unoccupied is reduced. Shake-up effects cause characteristic satellite peaks besides the main lines of the photoemission. The intensity of the satellite peaks is defined by the overlap of the shake-up final state and the initial state.

Intensity and quantification For a homogeneous sample the intensity which is measured as a count rate for a certain peak in the spectrum is given by

$$I_i = N_i \cdot \sigma_i \cdot y_i \cdot \lambda_i \cdot f \cdot \theta \cdot A \cdot T \tag{2.3}$$

with

N_i: density of atoms [m^3] of an element
σ_i: ionization cross-section
y_i: photoelectron yield
λ_i: mean attenuation length of the photoelectrons [m]
f: X-ray flux density [photons/m^{2}s]
θ: efficiency factor (depending on take-off angle)
A: area of X-ray beam spot [m^2]
T: transmission

From equation 2.3 the atomic density N_i is given by

$$N_i = \frac{I_i}{\sigma_i \cdot y_i \cdot \lambda_i \cdot f \cdot \theta \cdot A \cdot T} = \frac{I_i}{S_i} \tag{2.4}$$

In equation 2.4 S_i is the sensitivity factor. In case there are emission lines of two elements in one spectrum following equation is valid

$$\frac{N_1}{N_2} = \frac{I_1/S_1}{I_2/S_2} \tag{2.5}$$

The concentration of an element x (c$_x$) can then be written as

$$c_x = \frac{N_x}{\sum N_i} = \frac{I_x/S_x}{\sum I_i/S_i} \tag{2.6}$$

The use of atomic sensitivity factors usually provides results with a relative error of about 10-20%.

Attenuation length and film thickness The attenuation length λ [83] is defined as the average distance of an electron traveled between two inelastic collisions [35]. It is derived using a model where elastic collicons can be neglected and with this differs from the inelastic mean free path (IMFP) [84]. The attenuation length of photoelectrons through a self-assembled monolayer of alkanethiols [85] is given by

$$\lambda = k \times E_k^p \tag{2.7}$$

where k and p are empirically derived contants. For thiols on gold k was determined to be 0.3 and p was estimated to be 0.64 [86, 87].

To calculate the film thickness of a monolayer on a gold surface, either the intensity ratio of the gold signal of clean gold substrate and sample $\frac{I^{Au(4f)}}{I_0^{Au(4f)}}$

$$\frac{I^{Au(4f)}}{I_0^{Au(4f)}} = exp\left(-\frac{d}{\lambda\ sin\theta}\right) \tag{2.8}$$

or the intensity of carbon signal and the gold signal of the sample $\frac{I_{C(1s)}}{I_{Au(4f)}}$

$$\frac{I_{C(1s)}}{I_{Au(4f)}} = \frac{N_C}{N_{Au}} \frac{\sigma_{C(1s)}}{\sigma_{Au(4f)}} \frac{T_{C(1s)}}{T_{Au(4f)}} \frac{\lambda_{C(1s)}}{\lambda_{Au(4f)}} \frac{1 - exp\left(\frac{d_C}{\lambda_C}\right)}{exp\left(\frac{d_{CS}}{\lambda_{Au}}\right)} \tag{2.9}$$

with

I: integrated peak area
N: density of atoms of an element
σ: ionization cross-section
T: transmission
λ_C: attenuation length of the C 1s photoelectrons through carbon layer
λ_{Au}: attenuation length of the Au 4f photoelectrons through thiolate layer
d_C: thickness of the carbon layer
d_{CS}: thickness of the thiolate layer

need to be taken into account. The attenuation length of the photoelectrons is directly related to these ratios in the following way [88]: Using the attenuation of the Au 4f signal shown in equation 2.8 the film thickness can be calculated by

$$d = -\lambda\ sin\theta\ ln\left(\frac{I^{Au(4f)}}{I_0^{Au(4f)}}\right) \tag{2.10}$$

In case of using the carbon to gold signal ratio (see equation 2.9) the film thickness was calculated by a software developed in our research group (by Martin Schmid) solving equation 2.9.

Using the intrument specific constant k, equation 2.9 can be written as

$$\frac{I_{C(1s)}}{I_{Au(4f)}} = k\frac{1 - exp\left(\frac{d_C}{\lambda_C}\right)}{exp\left(\frac{d_{CS}}{\lambda_{Au}}\right)} \tag{2.11}$$

with $k = \dfrac{N_C}{N_{Au}}\dfrac{\sigma_{C(1s)}}{\sigma_{Au(4f)}}\dfrac{T_{C(1s)}}{T_{Au(4f)}}\dfrac{\lambda_{C(1s)}}{\lambda_{Au(4f)}}$ as specific instrument constant.

2.1.2 Near-edge X-ray absorption fine-structure spectroscopy

In case of the absorption of an X-ray photon, a photoelectron can be emitted (XPS) or it can be excited to unoccupied valence states when the photon energies are close to the ionization potential (IP) of a particular core level [89] (see Figure 2.2). In the near-edge X-ray absorption spectroscopy (*Near-Edge X-ray Absorption Fine-Structure*, NEXAFS) the absorption probability is measured as a function of the energy and the polarization of the X-rays. Due to the excitations of core electrons NEXAFS spectroscopy is element-specific. Furthermore, orbital and absorption geometries can be studied via synchrotron irradiation with a high degree of polarization and the use of the selection rules [89]. By using Fermi's golden rule, the transition probability P_{im} between the initial state $|i\rangle$ and the intermediate state $|m\rangle$ can be described as

$$P_{im} = \frac{2\pi}{\hbar}|\langle m|\overline{V}|i\rangle|^2\rho_m(E_i + h\nu) \tag{2.12}$$

Here $\overline{V}(t) = \overline{V}e^{-i\omega t}$ is the harmonic interference caused by the electric field of the photon and $\rho_m(E)$ is the density of states of the final state. By using the dipole approximation, the absorption cross section can be described as

$$\sigma_x = \frac{4\pi\hbar^2}{m_e^2}\frac{e^2}{\hbar c}\frac{1}{\hbar\omega}|\langle m|\overline{e}\cdot\overline{p}|i\rangle|^2\rho_m(E_i + h\nu) \tag{2.13}$$

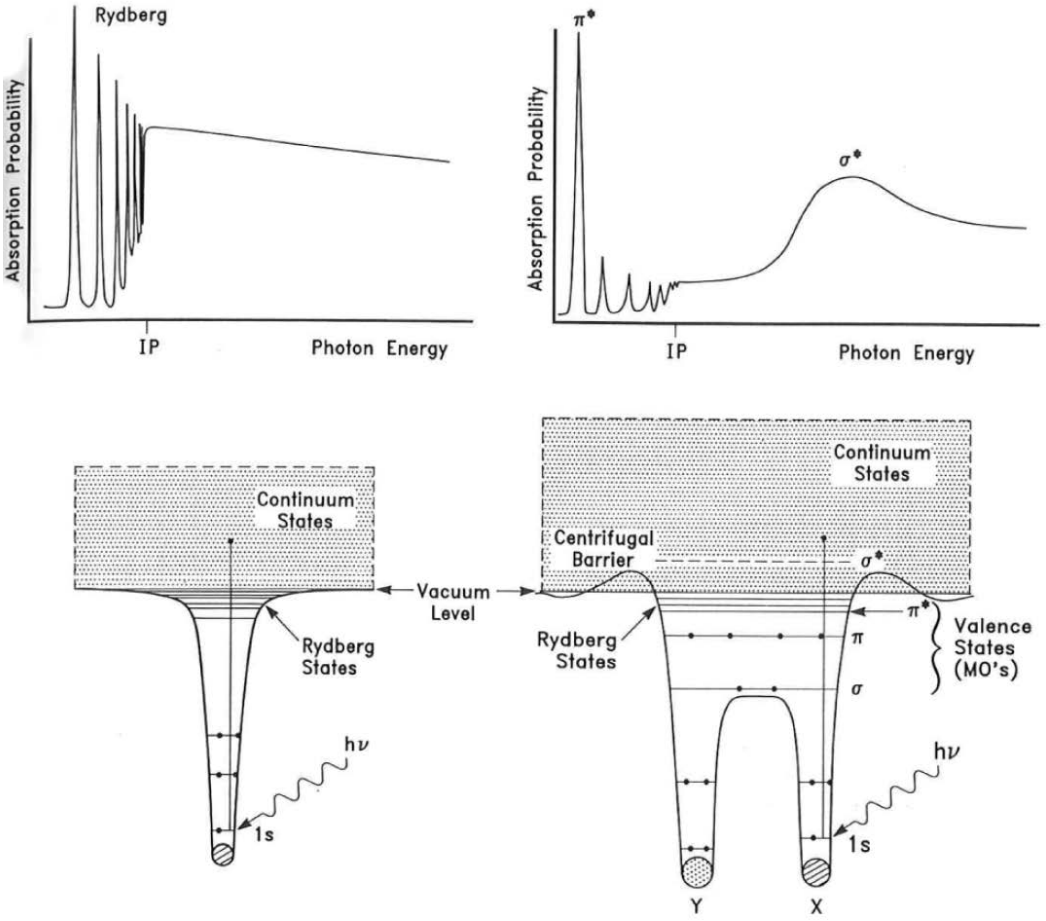
Rydberg
Absorption Probability
IP
Photon Energy
π*
Absorption Probability
σ*
IP
Photon Energy
Continuum States
Vacuum Level
Rydberg States
hν
1s
Continuum States
Centrifugal Barrier
σ*
π*
π
σ
Valence States (MO's)
Rydberg States
hν
1s
Y
X

FIGURE 2.2: Scheme of the potential of an atom and a molecule consisting of two atoms and their resulting NEXAFS spectra [89].

The absorption cross section is mainly influenced by the overlap of the unoccupied orbital $|m\rangle$ and the core level $|i\rangle$ [89].
The absorption of X-ray quanta can be quantified by the decay of the excitation. In case of elements with low atomic numbers (Z<10), 99% of all core levels decay in terms of Auger effects [89]. These can be proved by showing the equalizing current through the sample holder or by measuring the emitted Auger electrons [90].

Resonance types and line shapes The electric potential of a diatomic molecule is shown in a schematic drawing in Figure 2.2. It follows from the Coulomb interaction between atomic nucleus and electrons combined with exchange interaction and a barrier of the angular momentum [89]. In spherical coordinates of the nucleus system (center of gravity system) the angular momentum barrier can be described as $\frac{l(l+1)\hbar^2}{2mr^2}$ and splits the potential into a deep potential well near to the

core and a (external) flat potential well.
The low-energy resonances correlate with the electronic dipole transition from the core level into unoccupied molecular orbitals having, most frequently, a π^* or σ^* symmetry. The line shape of the molecular resonances is given by the spectral energy distribution of the exciting synchrotron irradiation and the lifetime broadening τ_{res} of the excited state. From the Heisenberg uncertainty principle the lifetime broadening is composed of the lifetime τ_e of an excited electron in the molecular potential and the lifetime τ_h of the core hole [91].

$$\Gamma \cong \frac{\hbar}{\tau_{res}} = \frac{\hbar}{\tau_e} + \frac{\hbar}{\tau_h} \tag{2.14}$$

The lifetime broadening τ_{res} (in Lorentz shape) of lightweight elements is about 0.1 eV. Additional broadenings may appear from vibrations caused by dipole excitation and ionization. In heterogeneous samples the excitation energies of the same element may be different due to chemical shifts. Aditionally the lines can be broadened due to averaging over bigger $\mathrm{k}_{\|}$ areas, especially in case of dispersion of the observed states [92].
In the region below the ionization potential (IP) there are the Rydberg states R^*. The ones of highest energy expand to the external potential well. Due to the low overlap with the core level the NEXAFS intensity is lower than the ones from orbitals with a stronger bonding. Additionally the delocalized states R^* have a higher interaction with their environment and are highly suppressed (e.g. in case of chemisorption of alkanes on metals) [93].
Above the ionization potential (IP) there are σ^* shape resonances. The spectral shape and the photon energy $h\nu$ corresponding to these resonances is given by the shape of the potential barrier. The potential barrier stabilizes the quasi-bound states avoiding instantaneous decay in vacuum states. With increasing excitation energy the tunnelling process becomes more effective and the lifetime broadening of the shape resonances increases. The asymmetry of the resonances comes from the oscillation excitation during electric transmission. The periodic change of the nuclear distances causes a periodic shift of the resonance energy. The intensity distribution of the shape resonances describe the weighting of the nuclear distances during the scattering process. Short distances cause a strong short-term shift in the resonance energy. From the mean resonance energies, the average core distances of diatomic and quasi-diatomic molecules can be derived with high accuracy [89].

Above the shape resonances there is a direct photoemission. Since there is always a vacuum level that fulfills the selection rules, the absorption is independent from the orientation of the direction of the electric field vector.

Angle dependence The intensity of the absorption resonance depends on the orientation of the electric field vector of the synchrotron light with respect to the molecular orbital of interest (see Figure 2.3). This intensity is proportional to the square of the scalar product of the electric field vector $\vec{E}$ and the orbital vector $\vec{O}$ shown in equation 2.15

$$I \propto |\vec{E} \cdot \vec{O}| \tag{2.15}$$

The resonance absorption intensity is evaluated according to the theoretical expression (for a vector-type orbital) [89]

$$I(\alpha, \theta) = A\left\{P \times \frac{1}{3}\left[1 + \frac{1}{2}\left(3cos^2(\theta) - 1\right)\left(3cos^2(\alpha) - 1\right)\right] + (1-P)\frac{1}{2}sin^2(\alpha)\right\} \tag{2.16}$$

with

A: constant
P: polarization factor of the X-rays
θ: incidence angle of the X-rays
α: average tilt angle of the molecular orbital

For π^* orbitals, where the transition dipole moment (TDM) is perpendicular to the plane of the respective phenyl ring, the tilt angle of the orbital α is directly related to the tilt angle of the molecular backbone β in the following equation [94]

$$cos(\alpha) = sin(\beta)cos(\gamma) \tag{2.17}$$

where γ is the twist angle of the corresponding phenyl ring with respect to the plane spanned by the surface normal and the molecular axis. At θ=0 the TDM lies in this plane [94].

Linear dichroism The linear dichroism is a fingerprint of the orientation of the molecular orbitals. The dependence of the intensity of the absorption resonance on the orientation of the electric field vector of the X-rays with respect to the

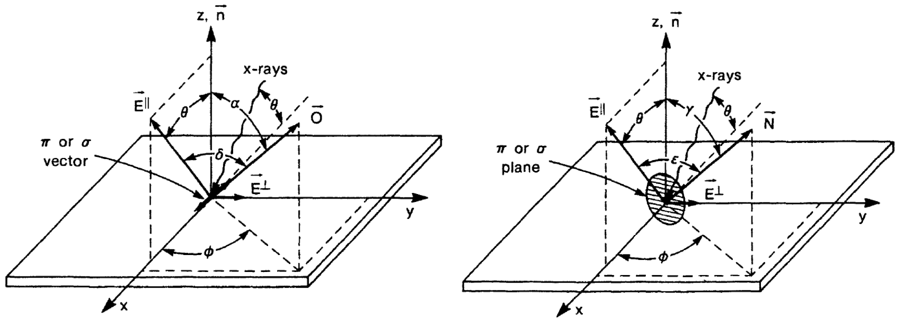

(a) Vectorial orbital (b) Planar orbital

FIGURE 2.3: (a) Coordinate system defining the geometry of a σ^* or π^* vector orbital on the surface. The orientation of the orbital, i.e. of the vector $\vec{O}$, is characterized by a polar angle α and an azimuthal angle ϕ. The X-rays are incident in the (x,z) orbit plane of the storage ring which contains the major electric field vector component $\vec{E}^{\parallel}$. The X-ray incidence angle θ is changed by rotating the crystal about the y-axis. The weaker component $\vec{E}^{\perp}$ lies in the surface plane, along the y-axis. The z-axis is the surface normal. (b) same for a π^* or σ^* plane. The plane is characterized by the polar (γ) and azimuthal (ϕ) orientation of its normal $\vec{N}$. The plane is tilted from the surface by γ. [89]

molecular orbital of interest. The linear dichroism can be conveniently monitored by plotting the difference of the NEXAFS spectra aquired at 90° (normal angle) and 20° (grazing angle) of X-ray incidence. For comparison, a spectrum aquired at 55° (so-called magic angle) gives only information about the chemical identity of the samples of interest due to the fact that a spectrum aquired at this angle is not affected by any effects related to the molecular orientation [89]. Additionally the angle of the molecular orbital of interest can be determined by using the ratio $I(\theta)/I(20°)$. In this work an angle of 90° was used in equation 2.17. Finally, the tilt angle of a molecule can then be determined.

2.1.3 Kelvin Probe

To measure the work function of surfaces the Kelvin Probe (KP) was used. The basic principle is to measure the contact potential difference (CPD) between two metals brought close to each other (~1mm). Due to the fact that these two metals do not touch each other they form a capacitor [95]. One of these electrodes is then the tip of the Kelvin Probe itself and the other one is the substrate/sample of interest (Figure 2.4a). In case of electrical contact between the sample and the tip, their Fermi levels are equalized due to the contact potential difference V_{CPD} generated by the electrical charging of the tip and the sample (Figure 2.4b). To

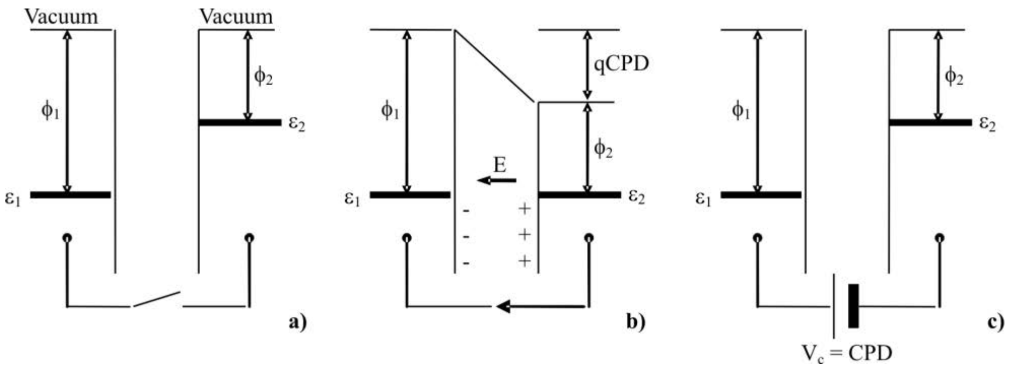

Figure 2.4: Schematic diagram of Kelvin Probe physics. a) Two materials 1 and 2 with different work functions ϕ_1 and ϕ_2, corresponding to the energy difference between the Fermi level ϵ and the vacuum level. b) When the two materials are electrically contacted, electrons flow from 2 to 1 until the Fermi levels are aligned, leading to a contact potential V_b. The charges present in the two materials causes an electric field E. q: electron charge; CPD: contact potential difference. c) The electric field is removed by applying an external potential Vc which equals the contact potential. Adapted from [95].

nullify the electric field between sample and tip an external voltage V_b (backing potential) is applied (Figure 2.4c) [95]. The work function of a sample can be determined by the following equation (with the known work functiuon of the Kelvin Probe)

$$\phi_{Sample} = \phi_{ref} - qV_b \tag{2.18}$$

Kelvin Probe work function measurements only provide relative work function values compared to a reference (work function difference $\Delta\phi$). Absolute values can be determined by using already known standard references like, i.e. clean gold substrates.

The mechanical oscillation of the Kelvin Probe tip induces a periodical change in the capacitance

$$C_K = \epsilon_0 \epsilon_r \frac{A}{d(t)} \tag{2.19}$$

assuming that the periodical tip-sample spacing is given by $d(t) = d_0 + d1sin(\omega t)$ the capacitance can be described by

$$C_K(t) = \frac{C_0}{1 + \epsilon\ sin(\omega t)} \tag{2.20}$$

where C_0 represents the mean capacity and ϵ is the modulation index $\left(\frac{d_1}{d_0}\right)$.

The change in capacitance generates a small alternating current

$$i(t) = V_C \omega \Delta C\ cos\omega \tag{2.21}$$

where V_C is the contact potential difference (CPD), ω the frequency and ΔC the change in capacitance. To nullify the electric field and thus the current i(t), an external voltage $V_b = -V_C$ is applied [95].

2.1.4 Ultraviolet photoelectron spectroscopy (UPS)

The ultraviolet photoelectron spectroscopy (UPS) is related to the X-ray photoelectron spectroscopy (XPS). The main difference between UPS and XPS is the energy of the excitation radiation. As light source a He lamps ($h\nu$ =21.21eV) are generally used in laboratories. Alternatively, synchrotron irradiation can be used (it shows good stability and is tunable with a monochromator); the photon energy can be varied between approximately 10-100 eV (depending on the beamline setup). At these low energies only the valence levels can be probed (valence band spaectra). In case of solid interfaces, the energy distribution of the photoemitted electrons may vary to small extents with the direction of the emission. This technique is sensitive to surfaces and does not provide informations about the bulk. By using UPS the work function of metal surfaces can be determined. Thus, it is necessary to know that the work function corresponds to the minimum amount of energy needed to remove an electron from the metal (see Figure 2.5). The value of the work function of a certain metal (here: Au) can be determined by the difference between the photon energy ($h\nu$=21.21 eV) and the secondary cutoff E_{cutoff}

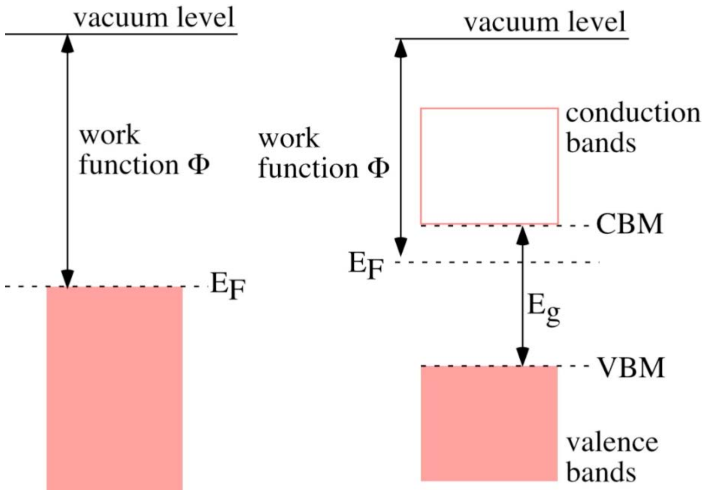

(a) Metal (b) Semiconductor

FIGURE 2.5: Schematic energy diagram of a metal (a) and a semiconductor (b). Adapted from "Tutorial on Work Function" by Dr. Rudy Schlaf.

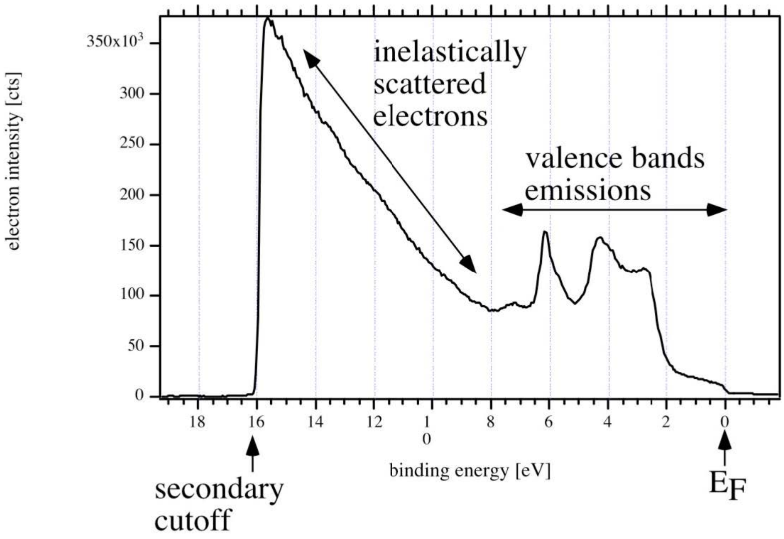

FIGURE 2.6: UP spectrum of gold surface. Adapted from ”Tutorial on Work Function” by Dr. Rudy Schlaf.

in the UP spectrum (see Figure 2.6)

$$\Phi_{Au} = h\nu - E_{cutoff} \tag{2.22}$$

2.2 Self-assembled monolayers

Self-assembled monolayers (SAMs) are monomolecular films consisting of molecules that are able to bind and order on a surface independently if they are in gas phase or in solution. There are many publications, on these systems, which can not all be reviewed in detail here [2, 96–99]. SAM constituents consist usually of three essential parts:

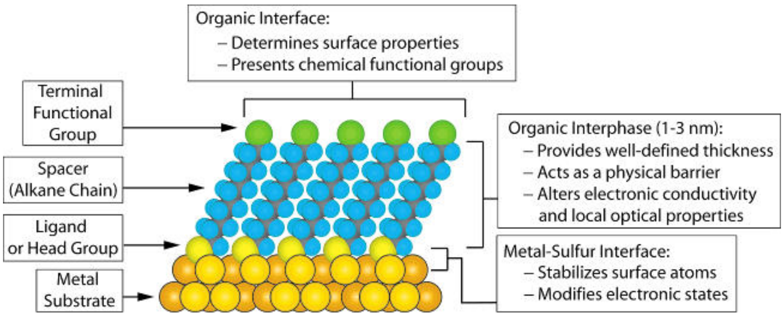
Organic Interface:
– Determines surface properties
– Presents chemical functional groups
Terminal Functional Group
Spacer (Alkane Chain)
Ligand or Head Group
Metal Substrate
Organic Interphase (1-3 nm):
– Provides well-defined thickness
– Acts as a physical barrier
– Alters electronic conductivity and local optical properties
Metal-Sulfur Interface:
– Stabilizes surface atoms
– Modifies electronic states

FIGURE 2.7: Schematic diagram of an ideal, single-crystalline SAM of alkanethiolates supported on a gold surface with a (111) texture. The anatomy and characteristics of the SAM are highlighted. Adapted from [2].

- head (docking) group (binding to the substrate)
- spacer (molecular chain; connects head group with the functional group)
- functional (tail) group

like it is shown in Figure 2.7. Different molecular chains can be used as spacer. The most common one is the alkane chain combined with a head group on top of the molecule determining the surface properties of the SAMs. There are various other spacers that are used for different substrates and different purposes. Being used as so-called model system are the silane groups [100]. Another one used as a model system is the thiol group, which can form very stable bonds on coinage metal substrates like gold or silver. Thiol bonds have a certain lateral mobility, which helps to get a regular molecular arrangement studied systematically for alkanethiols [3]. On Au(111) substrates, they adopt a $(\sqrt{3} \times \sqrt{3})R30°$ structure with a possible superlattice termed c(4×2), corresponding to a ~0.5 nm spacing between the molecules and an area per molecule of 21.6 Å^2 [101–106].

2.2.1 Odd-even effect

The so called odd-even effect causes periodic changes in the packing density and the film thickness due to the number of methylene units in the aliphatic linker. A higher packing density associated with smaller inclination of the SAM constituents is observed for the films with an odd number of methylene units on Au subtrates and an even number of methylene units on Ag substrates (see Figure 2.8) [107].

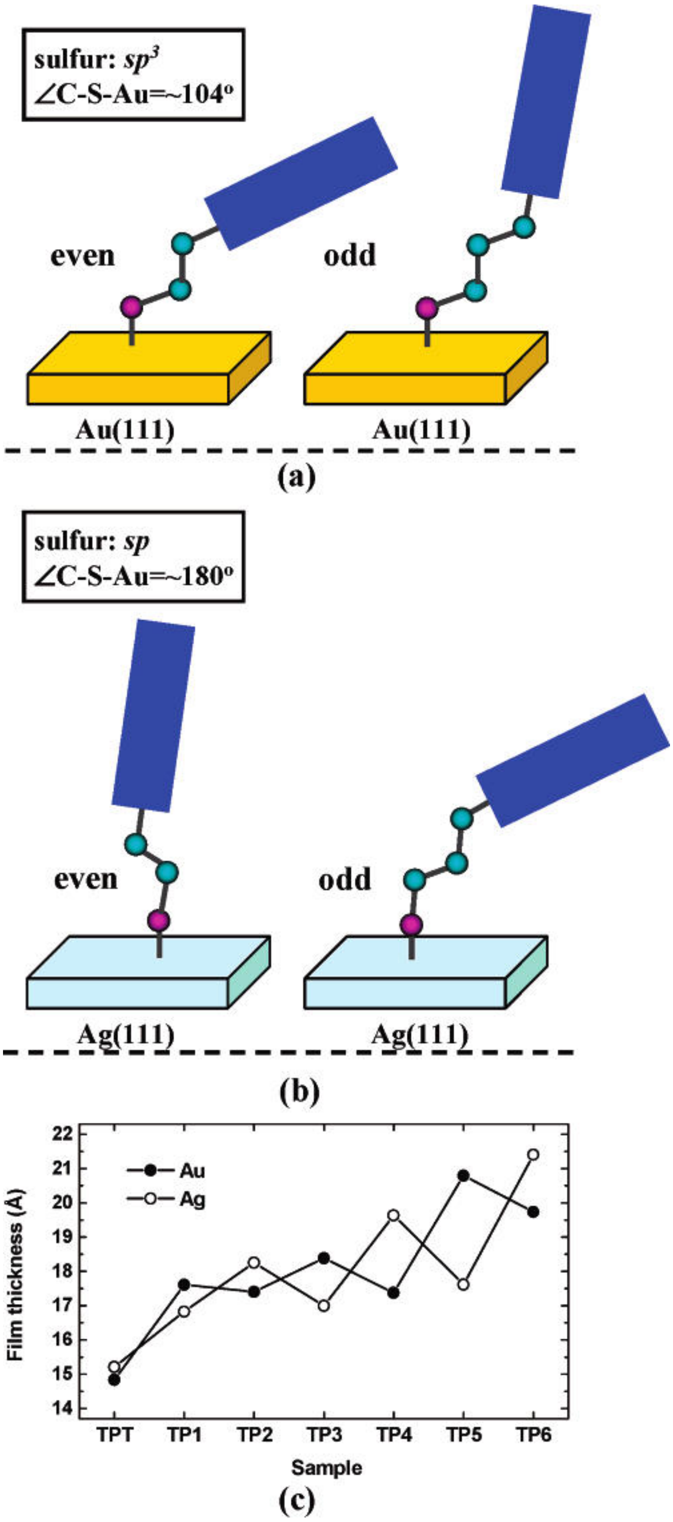
sulfur: sp³
∠C-S-Au=~104°
even
odd
Au(111)
Au(111)
(a)
sulfur: sp
∠C-S-Au=~180°
even
odd
Ag(111)
Ag(111)
(b)
Au
Ag
Film thickness (Å)
22
21
20
19
18
17
16
15
14
TPT
TP1
TP2
TP3
TP4
TP5
TP6
Sample
(c)

FIGURE 2.8: Schemes showing the orientation of the terminal terphenyl rings and the binding geometry of TP$_n$ monolayers on Au(111) (a) and Ag(111) (b). (c) Effective film thickness of TP$_n$/Au(111) and TP$_n$/Ag(111) derived from the ellipsometry data. Adapted from [107].

2.3 Molecular dipole and work function

The molecular dipole is the key factor controlling the work function at interfaces. One of the most important characteristics of surfaces and interfaces is the work function. It is equal to the surface potential which is dependent on the value and direction of the molecular dipole moment μ.

2.4 Photoisomerization

Photoisomerization is a conformational change induced by optical radiation. In case of azobenzene molecules it is the conformation change from *trans* to *cis* conformation and vice versa (see Figure 2.9). This photochemical process is caused by irradiation with UV or visible light. Irradiating azobenzene molecules with UV light leads to a conformation change from *trans* to *cis*; irradiation with visible light leads to a conformation change from *cis* to *trans*. Due to the fact that the *trans* conformation is the thermodynamically more stable one, azobenzene molecules is *cis* conformation perform a so called backisomerization from *cis* to *trans* after a certain time (in the dark).

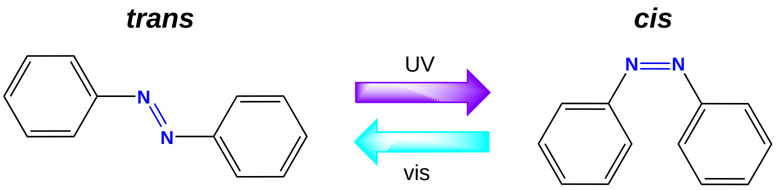

FIGURE 2.9: Azobenzene molecule

2.4.1 Work function change

The conformation change of the azobenzene molecules assembled on a solid surface may cause a change of the molecular dipole, which can be directly monitored measuring the work function. The molecular dipole of the azobenzene molecule in *trans* conformation is almost zero, while it has a certain value in *cis* conformation. Along these lines the work function of assembled azobenzene molecules in *cis* conformation is higher than in *trans* conformation.

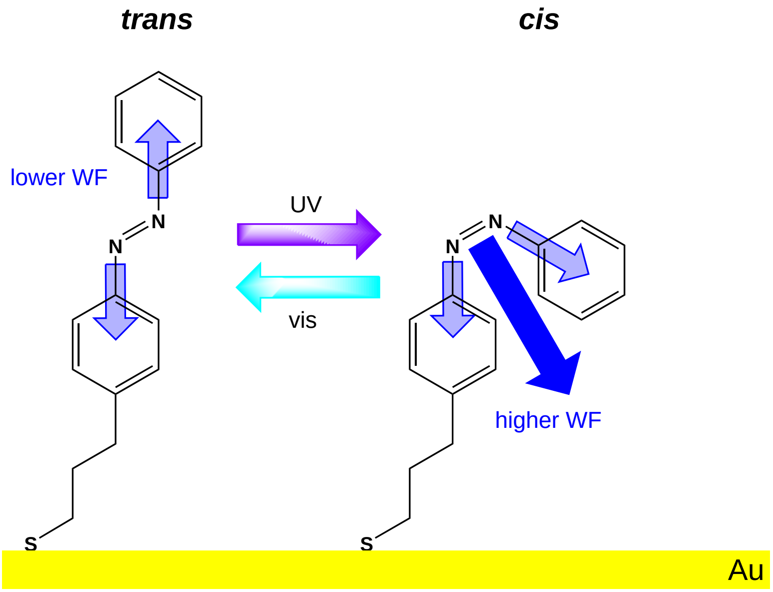
trans
cis
lower WF
UV
vis
N
N
N
N
S
S
higher WF
Au

Figure 2.10: Schematic drawing of H-azo isomerization and its influence on the molecular dipole and the work function

Chapter 3

Materials and Methods

In this chapter the chemical compounds, materials and characterization techniques are presented which were used in this work. Starting with the compounds, the sample preparation, their characterization methods and additional performed experiments are described in the following sections.

3.1 Compounds and Chemicals

In this section the compounds and partially their synthesis are presented. The used compounds were all synthesized by our partner groups.

3.1.1 Embedded Ester

The compounds were synthesized by the group of Prof. Jean-François Morin from the Univerité Laval (Québec City, Canada) and the group of Prof. David L. Allara from the Pennsylvania State University (USA) using standard methods [30]. A list of the molecules and ebbeviations for the SAMs is shown in table 3.1.

3.1.2 Embedded pyrmidine

The compounds were synthesized by Tarek Abu-Husein and Tobias Santowski from the group of Prof. Andreas Terfort from the Frankfurt University [108]. While

Compound	Abbreviation
SH-$(CH_2)_{15}$-CH_3	C16
SH-$(CH_2)_{10}$-COO-CH_3	C10EC1
SH-$(CH_2)_{12}$-COO-CH_3	C12EC1
SH-$(CH_2)_{10}$-COO-CH_3	C15EC1
SH-$(CH_2)_5$-COO-$(CH_2)_9$-CH_3	C5EC10
SH-$(CH_2)_{10}$-COO-$(CH_2)_4$-CH_3	C10EC5
SH-$(CH_2)_{10}$-COO-$(CH_2)_9$-CH_3	C10EC10
SH-$(CH_2)_{10}$-OOC-$(CH_2)_9$-CH_3	C10E*C10
SH-$(CH_2)_{10}$-COO-$(CH_2)_{14}$-CH_3	C10EC15
SH-$(CH_2)_{15}$-COO-$(CH_2)_4$-CH_3	C15EC5
SH-$(CH_2)_{15}$-COO-$(CH_2)_9$-CH_3	C15EC10
SH-$(CH_2)_{20}$-COO-$(CH_2)_4$-CH_3	C20EC5

TABLE 3.1: Compounds used and abbreviations for their SAMs

the synthesis of TP1 has been described in the literature and was performed accordingly [42, 109], the procedure for the pyrimidine containing molecules, TP1-up and TP1-down, had to be developed. The strategy to synthesize these molecules is summarized in Figure 3.1. The Kumada coupling of the Grignard reagent 3, formed from 4 bromobenzyl(triisopropylsilyl)sulfide, with amino- or pyridine-terminated bromophenyl-derivatives has been developed and optimized previously [110]. The synthesis of the coupling partners, 5-bromo-2-phenylpyrimidine (1) and 2-chloro-5-phenylpyrimidine (2), via Suzuki coupling reactions has been described in the literature [111, 112]. The resulting triisopropylsilyl (TIPS) protected compounds 4 and 5 were deprotected protolytically using aqueous HCl in methanol. The final TP1-up and TP1-down substances are air-stable as crystalline compounds but become easily oxidized to the less soluble disulfides in solution. All other chemicals, including 2-MPM, 1 dodecanethiol (DDT) and 1 hexadecanethiol (HDT) were purchased from Sigma-Aldrich and used as received.

3.1.3 Azobenzenealkanethiols

H-azo-Cn (C_6H_4-N-N-C_6H_4-$(CH_2)_n$-SH, n = 3,4) compounds were synthesized by Simone Krakert from the group of Prof. Andreas Terfort from the Frankfurt University [28].

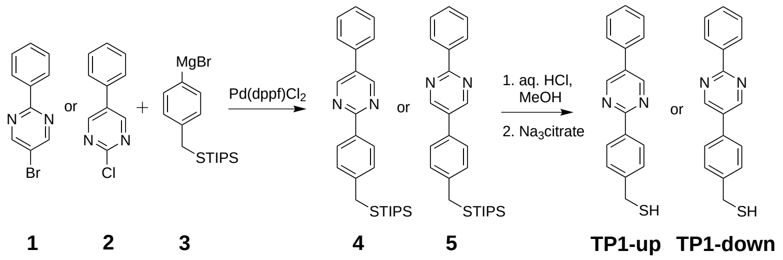

FIGURE 3.1: Outline of the syntheses of the dipolar molecules, TP1-up and TP1-down. [courtesy of Tarek Abu-Husein, Tobias Santowski and Prof. Andreas Terfort from the Frankfurt University]

3.2 Preparation of the SAMs

The gold substrates were, in most cases, purchased from Georg Albert PVD-Beschichtungen and used as received. They were prepared by thermal evaporation of 100-200 nm of gold (99.99% purity) onto polished single-crystal Si(100) wafers (Silicon Sense) primed with a 5 nm adhesion layer of titanium or chromium. The resulting substrates were polycrystalline, with predominant (111) orientation and a grain or terrace size of 20-50 nm as observed by atomic force microscopy (AFM) and scanning tunneling microscopy (STM). For the STM studies of the SAMs (see below), 200 nm Au films on mica were purchased from Phasis (Geneva).

3.2.1 Embedded ester

The SAMs were prepared at room temperature. The freshly prepared gold substrates (200 nm Au on 10 nm Cr on Si wafer) were characterized by ellipsometry and placed in the appropriate thiol solution for ∼18-24 h. Upon removal, each sample was thoroughly rinsed with acetone and ethanol (C_2H_6O) and then blown dry under a stream of dry N_2. All solutions were prepared with absolute anhydrous ethanol (Aldrich), and typical solution concentrations ranged from 0.01 to 1 mM depending on the amount of compound available.

3.2.2 Embedded pyrmimidine

The SAMs were formed by immersion of the substrates into solutions of the SAM precursors in tetrahydrofuran (C_4H_8O) (concentration range 10 - 1000 μM) under nitrogen at ambient temperature for 24 h. After immersion, the samples were carefully rinsed with pure solvent and blown dry with a stream of N_2 or Ar. In addition to the target TP1-up and TP1-down films, we also prepared reference SAMs of TP1 and 2-MPM.

We also prepared alkanethiolate monolayers, viz. those of dodecanethiol (CH_3-$(CH_2)_{11}$-SH) and hexadecanethiol (CH_3-$(CH_2)_{15}$-SH), as references for the measurement of the effective thicknesses and packing densities, applying the standard preparation procedure [2].

3.2.3 Embedded pyrimidine mixed films

The mixed SAMs were formed by immersion of the substrates into mixed solutions of TP1-down and TP1-up in tetrahydrofuran (THF) with a concentration of about 0.1 mM for ∼24h at RT. The used mixing volume ratios were 50:50, 25:75, 75:25.

3.2.4 Azobenzenealkanethiols

The SAMs were formed by immersion of freshly prepared substrates into a 1 mM solution of H-azo-Cn in absolute ethanol at room temperature for 24 h at either room (21°C) or elevated (60°C) temperature, denoted as RT and ET below. After immersion, the samples were carefully rinsed with pure ethanol, blown dry with argon, and kept, in the case of the experiments at the synchrotron (see below), for several days in argon-filled glass containers until the characterization. No evidence for impurities or oxidative degradation products was found.

3.2.5 Azobenzenealkanethiols diluted with spacer molecules

We used a two-step procedure. First, SAMs of spacer molecules (octanethiol or phenylthiol) were formed by immersion of the substrate into a 1mM ethanolic solution of C8 or PT as a matrix (for 24 h at RT). After immersion, the samples were carefully rinsed with ethanol and blown dry with argon. The mixed SAMs

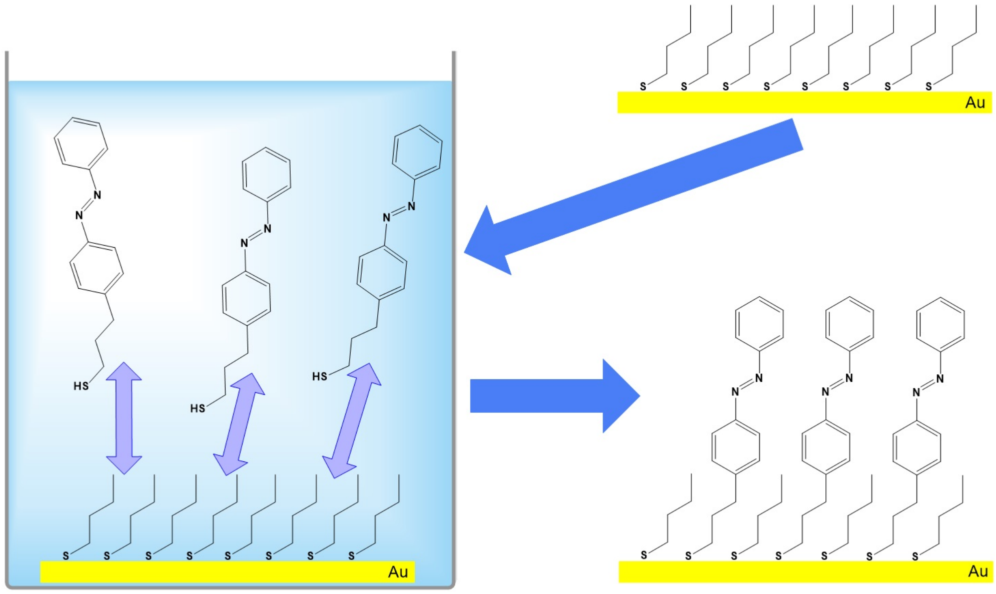

FIGURE 3.2: Schematic drawing of the praparation of azobenzene-substituted alkanethiols (H-azo-C3/C4) diluted with a short spacer molecule on a Au(111) substrate

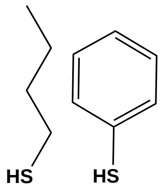

(a) (b)

FIGURE 3.3: Two types of short molecules used as a spacer for diluting azobenzenealkanethiols on a Au substrate: (a) short alkanethiols (AT) and (b) phenylthiol (PT)

were then formed by re-immersion of the above matrix film into 1 mM ethanolic H-azo-Cn solution for certain times (1 h, 3 h, 6 h, 12 h) at RT. After re-immersion the samples were carefully rinsed with ethanol and blown dry with argon, kept in argon-filled glass containers until experiments.

3.3 Characterization of the SAMs

The target and reference SAMs were characterized by XPS, high resolution XPS (HRXPS) and NEXAFS spectroscopy. All experiments were performed at room temperature. The XPS, HRXPS, and NEXAFS spectroscopy measurements were conducted under ultra-high vacuum (UHV) conditions at a base pressure better than 1.5×10^{-9} mbar. Special care was taken to minimize and avoid damage to the samples induced by X-rays during the measurements [68, 113].

3.3.1 XPS and HRXPS

The XPS measurements were performed using a laboratory spectrometer equipped with a Mg Kα X-ray source and an LHS11 analyzer. The spectra acquisition was carried out in normal emission geometry with an energy resolution of ∼0.9 eV. The X-ray source was operated at 260 W power and positioned ∼1 cm away from the samples. The BE scale was referenced to the Au $4f_{7/2}$ peak at a BE of 84.0 eV [114]. Since the quality of the XP spectra was inferior to the HRXPS data, they only were used to determine the effective thickness and packing density in the TP1, TP1-up and TP1-down monolayers. HRXPS measurements were conducted at the bending magnet beamline D1011 of the MAX-IV synchrotron radiation facility in Lund, Sweden, using a SCIENTA SES200 electron energy analyzer. The spectra were recorded in the Au 4f, S 2p, C 1s, N 1s, and O 1s regions. The spectra acquisition was performed in normal emission geometry and at PEs ranging from 350 to 580 eV. The BE scale of every spectrum was individually calibrated to the Au $4f_{7/2}$ emission of the gold substrate at 84.0 eV [115]. The energy resolution was better than 100 meV (mostly around 70 meV), which is noticeably smaller than the full width at half maximum (fwhm) of the spectral features relevant in this study. Both XP and HRXP spectra were fitted by symmetric Voigt functions and either Shirley-type or linear backgrounds. To fit the S $2p_{3/2,1/2}$ doublet, we used two peaks with the same fwhm, the standard [114] spin-orbit splitting of ∼1.18 eV (verified by fit), and a branching ratio of 2 (S $2p_{3/2}$/S $2p_{1/2}$). For all samples, the same fit parameters were used for identical spectral regions for a given photon energy. The effective film thicknesses were calculated by evaluating the intensity ratios of the C 1s and Au 4f emissions [88], and using a DDT SAM – a film of well-defined thickness (1.5 nm) [116] - as a reference system. A standard, exponential attenuation of the photoemission signal was assumed; attenuation lengths determined for a series of non-substituted alkanethiolate SAMs were used [85]. Further, the packing densities were coarsely estimated from the intensity ratios of the S 2p and Au 4f emissions, following the approach of refs [117] and [118]. As reference systems of reproducible quality and with well-known packing density (0.216 nm^2/molecule; 4.63×10^{14} molecules/cm^{-2}) [96, 119] DDT and HDT SAMs on Au(111) were used.

3.3.2 NEXAFS spectroscopy

NEXAFS spectroscopy experiments were performed at the same beamline as the HRXPS measurements. The spectra were acquired at the carbon and nitrogen K-edges in the partial electron yield acquisition mode with retarding voltages of -150 and -300 V, respectively. Linear-polarized synchrotron light with a polarization factor of ~95% was used. The energy resolution was better than 100 meV at the C K-edge and ~100 meV at the N K-edge. The incidence angle of the X-rays was varied from 90° (E vector in surface plane) to 20° (E vector nearly parallel to surface normal) in steps of $10-20°$ to monitor the orientational order in the SAMs. This approach is based on the linear dichroism in X-ray absorption, i.e. the dependence of the cross-section of the resonant photoexcitation process on the orientation of the electric field vector of the synchrotron light with respect to the molecular orbital of interest [89]. Raw NEXAFS spectra were normalized to the incident photon flux determined from the spectrum of a clean, freshly sputtered gold sample. Subsequently, they were reduced to the standard form by subtracting a linear pre-edge background and by normalizing to the unity edge jump. The energy scale was calibrated by means of the most intense π^* resonance of highly oriented pyrolytic graphite at 285.38 eV[120] in combination with the well-known $\Delta h\nu \propto (h\nu)^{3/2}$ behavior of plane grating monochromators [121].

3.3.3 Determination of the work function

Two alternative methods were used. First, the WF was determined by measuring the secondary electron cutoff of the UP spectra following a standard approach [31]. The experiments were performed at the Max IV facility, using the same beamline and experimental station as in the case of the HRXPS and NEXAFS measurements. The photon energy was set to 50 eV. UPS was performed by biasing the samples -25.6 V relative to ground so that the low energy portion of the spectrum could be observed. The positions of the cutoff in the target samples were referenced to those of HDT/Au and freshly sputtered gold. Second, WF measurements were carried out using a UHV Kelvin Probe 2001 system (KP technology Ltd., UK). The pressure in the UHV chamber was $\sim 10^{-10}$ mbar. The positions of the cutoff in the target samples were referenced to those of HDT/Au and freshly sputtered gold.

3.4 Photoisomerization experiments

The photoisomerization experiments were performed under UHV conditions at a pressure of $\sim 10^{-10}$mbar. After preparation of the samples they were loaded into UHV chamber and then transfered into the preparation chamber where the Kelvin Probe is installed. Before the irradiation experiments the work function of the sample in the dark was measured in the following way: The tip of the Kelvin Probe was moved close to the sample (~1mm) and the distance to the sample was adjusted with the Kelvin Probe software to obtain the required gradient (300) to measure the work function. After measuring the work function of the pristine SAM in the dark it was irradiated for ~15min with UV light. For this a UV LED lamp was used with a wavelength of 365nm and an intensity of ~6.5 mW/cm^2 on the sample. After ~15min UV irradiation the work function was measured like described before. During the measurement the UV light was kept irradiating the sample due to the shadow appearing on the sample while approaching to the surface.

The same procedure was performed for visible (blue) light irradiation where a blue LED lamp with a wavelength of 440nm and an intensity of ~3.0 mW/cm^2 on the sample was used.

This irradiation cycle (UV irradiation, WF measurement, vis. irradiation, WF measurement) was performed several times to obtain, in ideal case, a clear and significant work function variation due to the conformation change.

3.4.1 Photoisomerization of H-azo-Cn

Like shown in Figure 2.10, the azobenzene molecule changes its conformation from *trans* to *cis* after UV light irradiation. After irradiation with visible light the conformation is changing from cis to trans. The conformation also changes from *cis* to *trans* after a certain time in the dark, following the thermodynamic drive.

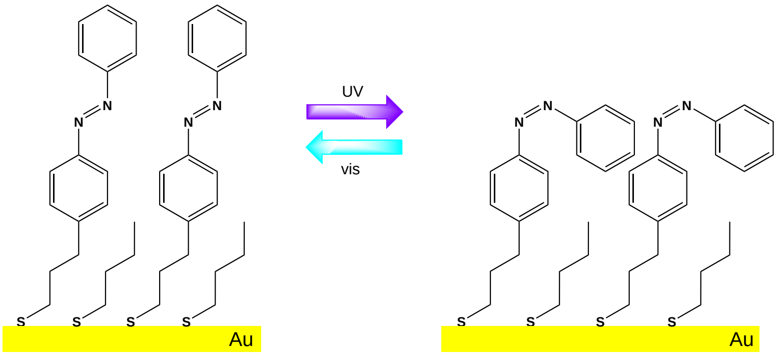
UV
vis
N
N
S
Au

Figure 3.4: Schematic drawing of H-azo-Cn diluted with AT, assembled on Au substrate.

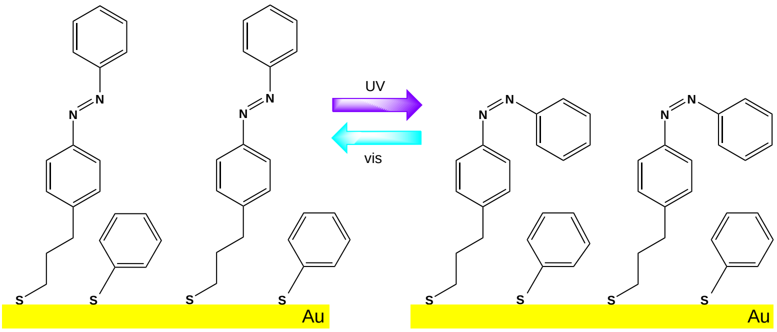
UV
vis
N
N
S
Au

Figure 3.5: Schematic drawing of H-azo-Cn diluted with PT, assembled on Au substrate.

Chapter 4

Results and Discussion

4.1 Embedded dipoles in aliphatic self-assembled monolayers

The mid-chain ester functionalized alkanethiols were characterized by infrared reflection absorption spectroscopy (IRRAS), atomic force microscopy (AFM), high resolution X-ray photoelectron spectroscopy and work function measurements. In the discussion we mainly focus on the characteristics in the HRXP spectra and the work function compared with the theoretical calculations. The IR and AFM measurements were performed by Orlando Cabarcos and Nichole Sullivan from the group of Prof. David L. Allara from the Pennsylvania State University (USA).

4.1.1 Basic characterization

In our previous study, the orientation of the alkyl chain segments and the embedded ester moiety in alkanethiolate SAMs were deduced from the best fits of spectral simulations, based on classical electromagnetic theory, to experimental IR data along with NEXAFS spectral analysis [30]. Both analyses agreed within experimental error to give an overall average of alkyl chain tilt from the surface normal of 31°(±4°) and a chain twist around the long axis of 60°(±5°). These values further are, within experimental error, identical to those reported previously for the alkyl chains in standard alkanethiolate SAMs and in the terminal ester SAM $HS(CH_2)_{15}CO_2CH_3/Au\{111\}$ SAM (C15EC1 ester in our terminology). In the present study all the IR spectra of the embedded esters with the same standard ester group chain attachment of Au-S$(CH_2)_m$E$(CH_2)_n$$CH_3$ (see Table 3.1) have nearly identical patterns to those in the previous study. Applying the same methods of analysis as used previously gives chain orientations within experimental error of the values above. Since the IR spectral pattern of the reversed ester (C10E*C10), however, was slightly different than for the E SAMs the orientation analysis for this SAM was done in more detail. The experimental spectra and best fit simulations of are shown in Figure 4.1. The overall result is that the average chain orientation of the reverse ester is tilted from the surface normal at 32°(±4°) with a chain twist around the long axis of 120°(±4°). These values are within the error ranges of the previously reported orientations for the set of embedded E ester SAMs and establish that inverting the ester group attachment on the alkyl chain has a negligible effect on the overall SAM orientation.

In order to definitively establish if there is a uniform arrangement of the reverse

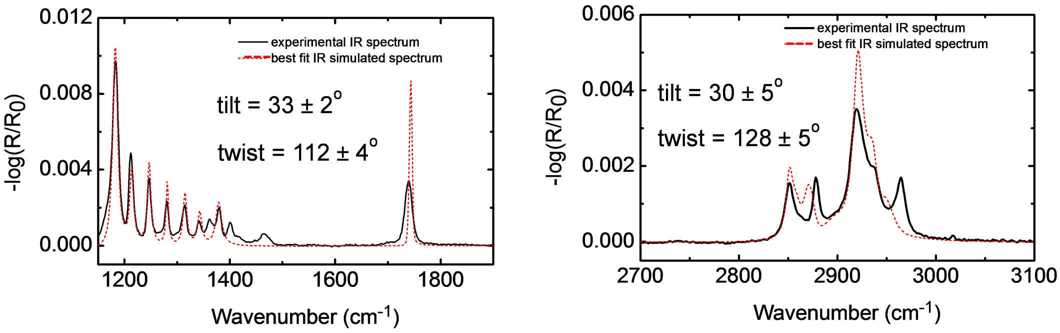

FIGURE 4.1: IR spectra for the C10E*C10 reverse ester SAM: experimental data and best-fit simulation. The best fit chain tilt and twist angles with estimated errors are shown in the graphs. The low frequency data (left) show modes for both the alkyl chains and the ester group while the high frequency data show the C-H stretch modes. The best fits represent global fits so not all modes have equal errors as noted particularly for the C=O stretch near 1730 cm^{-1}. [courtesy of Orlando Cabarcos, Nichole Sullivan and Prof. David L. Allara from the Pennsylvania State University]

ester SAM on the substrate surface, lateral force AFM microscopy was done. The result for the C10E*C10E SAM surface is shown in Figure 4.2 along with a comparison for the standard ester C10EC10. Both images confirm an ordered arrangement with the adsorbates in a hexagonal lattice with the expected ∼0.50 nm nearest neighbor spacing which corresponds to a surface density of 4.60 molecules/nm^{-2}. These data show that the reverse ester SAM has a virtually identical arrangement

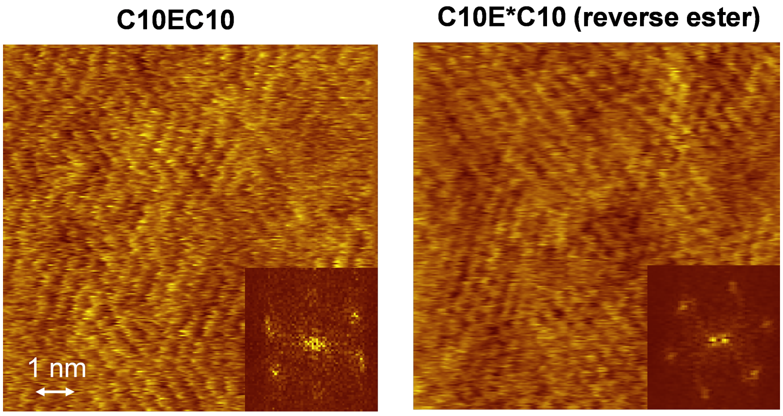

FIGURE 4.2: Lateral force AFM topography images of the C10EC10 and C10E*C10 SAMs with 2-D Fourier transforms shown in the insets. Both images clearly show a hexagonal pattern which consists of the standard $\sqrt{3} \times \sqrt{3}, R30$ pattern with lattice spacing of ∼0.50 nm. [courtesy of Orlando Cabarcos, Nichole Sullivan and Prof. David L. Allara from the Pennsylvania State University]

on the Au{111} surface as the standard embedded ester SAM, which is expected given the identical average chain orientation of the two types of SAMs.

4.1.2 Electrostatic effects

4.1.2.1 Photoemission

Binding energy shift The most important issue of our XPS analysis is the so-called peak splitting of the backbone in the C 1s spectra. This effect appears due to the embedded ester dipole, which exhibits a strong electrostatic effect which leads to this bind energy (BE) shift (∼0.85 eV between bottom and top segment). In Figure 4.4 the different components of the molecule (in this case C10EC10 shown also in Figure 4.3) are highlighted. Each of them lead to certain peaks in the C 1s spectrum as illustrated. The main peak (backbone) in this spectrum has a significant sholder. The reason for this is obviously a second peak as desribed before, which is caused by the embedded ester dipole. Usually alkanethiols show just one photoemission peak (from the backbone). But here we obtain a so-called binding energy shift between the two main components, the top segment (at ∼284.6 eV) and bottom segment (∼285.5 eV). The peak of the top segment is more intense due to the fact that it is located in the upper part of the monolayer (even if both segments have same length). Additionally the peaks of the ether carbon (at ∼286.8 eV) and the carbonyl carbon (at ∼289 eV) are visible. There

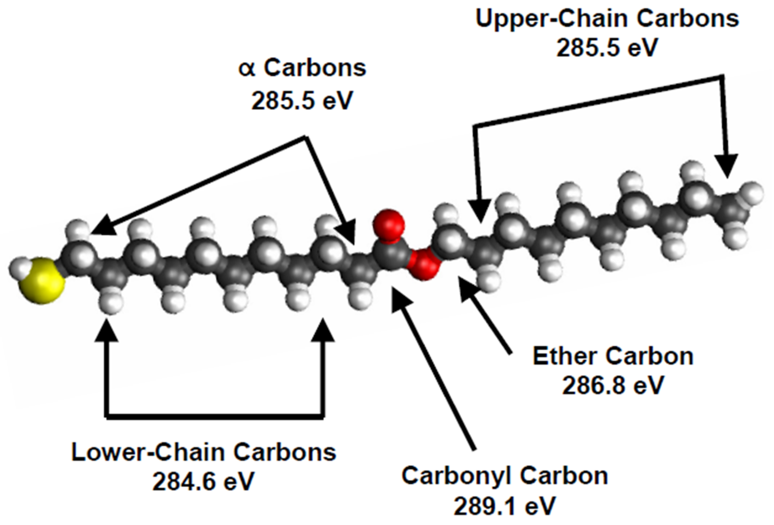
Upper-Chain Carbons
285.5 eV
α Carbons
285.5 eV
Ether Carbon
286.8 eV
Lower-Chain Carbons
284.6 eV
Carbonyl Carbon
289.1 eV

FIGURE 4.3: Assignment of C 1s features in the representative C10C10 ester SAM spectrum. All binding energies are referenced to the observed Au $4f_{7/2}$ peak set at 84.0 eV in the SAM spectrum. [30]

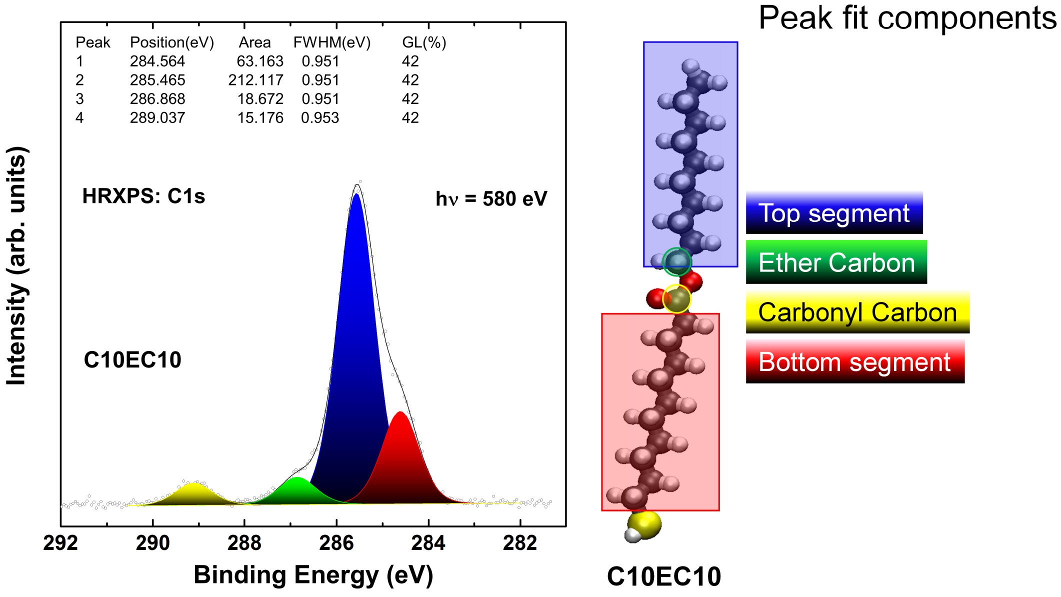

Peak	Position(eV)	Area	FWHM(eV)	GL(%)
1	284.564	63.163	0.951	42
2	285.465	212.117	0.951	42
3	286.868	18.672	0.951	42
4	289.037	15.176	0.953	42

FIGURE 4.4: HRXPS peak fit components due to peak splitting

should also be a feature of the α carbons (at ~285.5 eV) like shown in Figure 4.3; one of them is located at the sulfur atom another one next to the carbonyl carbon. But due to the fact that the peak of the top segment has same binding energy position, the corresponding peak is not visible. The information is important for a special type of the embedded ester systems which were anaylzed. In the following sections, the different types of embedded ester systems are compared to each other,

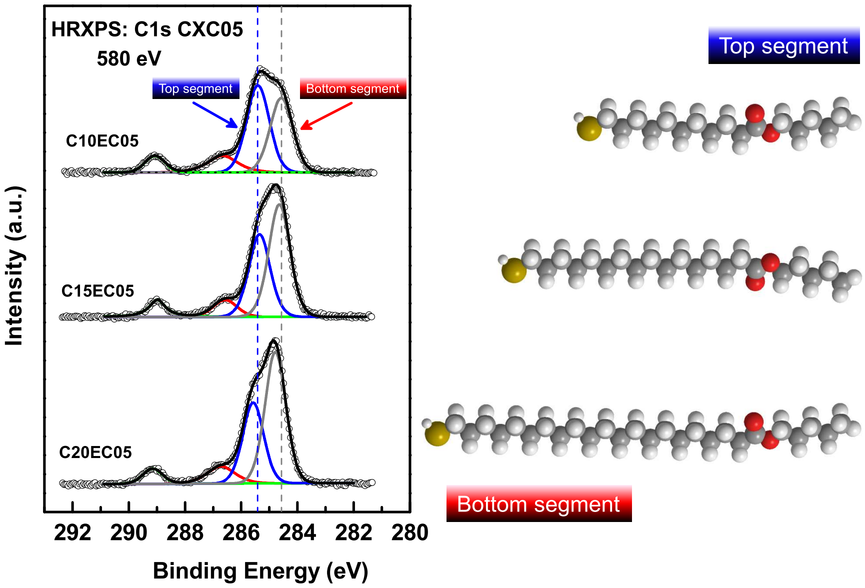

FIGURE 4.5: C 1s HRXP spectra of mid-chain ester funbctionalized alkanethiols of varied bottom segment and fixed top segment (5 methylene groups).

on one hand with fixed length of the top or bottom segment and, on the other hand, with inversed ester dipole.

Variation of the bottom segment In the first example as shown in Figure 4.5 we compared the systems having a fixed length of the top segment of five methylene groups. Here, a clear increase in the intensity of the bottom segment feature is visible upon the increase in its length, as can be expected in view of the molecular architecture. The second example shows the comparison between the systems having a fixed length of the top segment of 10 methylene groups (see Figure 4.6). Here, we also see the increase of the intensity of the bottom segment feature with increasing length of this segment, similar to the CXEC5 case. Another example, presented in Figure 4.7, shows the comparison between systems having one methyl group in the top segment (ether carbon). In this case, we can not really define the ether carbon as the top segment because the ether carbon peak has a different position compared to the top segment feature in all the other systems. The feature visible here (at ∼285.5 eV) comes from the α carbon atoms. As described before, their peak position is the same like the top segment in case of CXEC5 and CXEC10 (like shown in Figure 4.3).

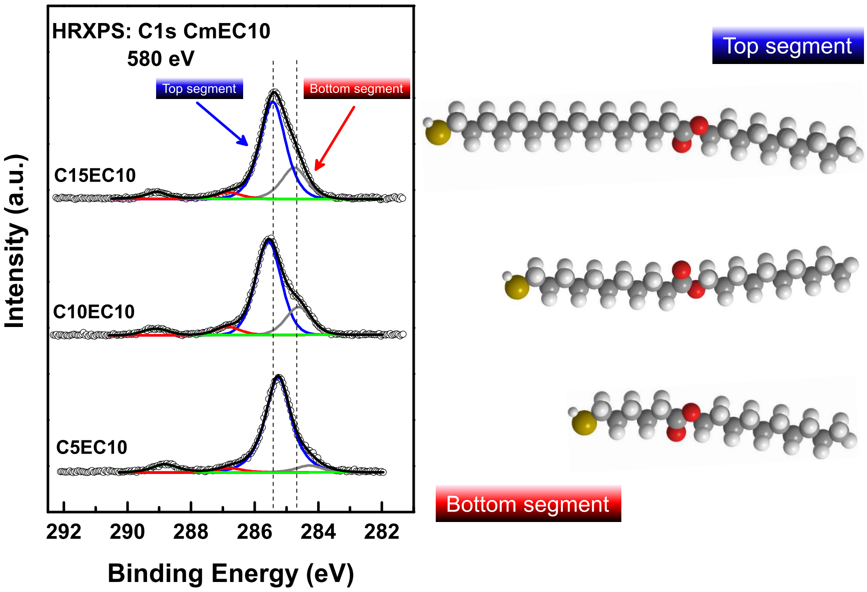

FIGURE 4.6: C 1s HRXP spectra of mid-chain ester functionalized alkanethiols of varied bottom segment and fixed top segment (10 methylene groups).

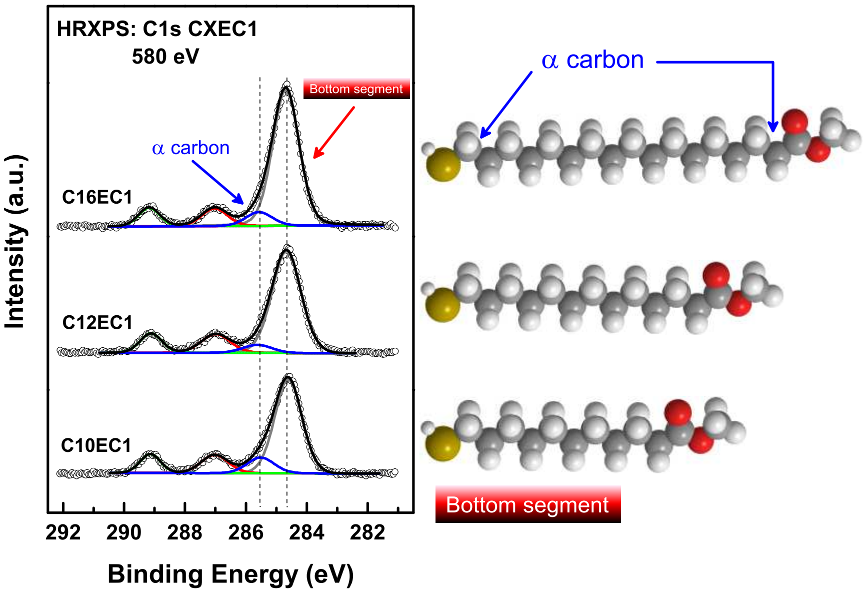

FIGURE 4.7: C 1s HRXP spectra of mid-chain ester functionalized alkanethiols of varied bottom segment and fixed top segment (ether carbon).

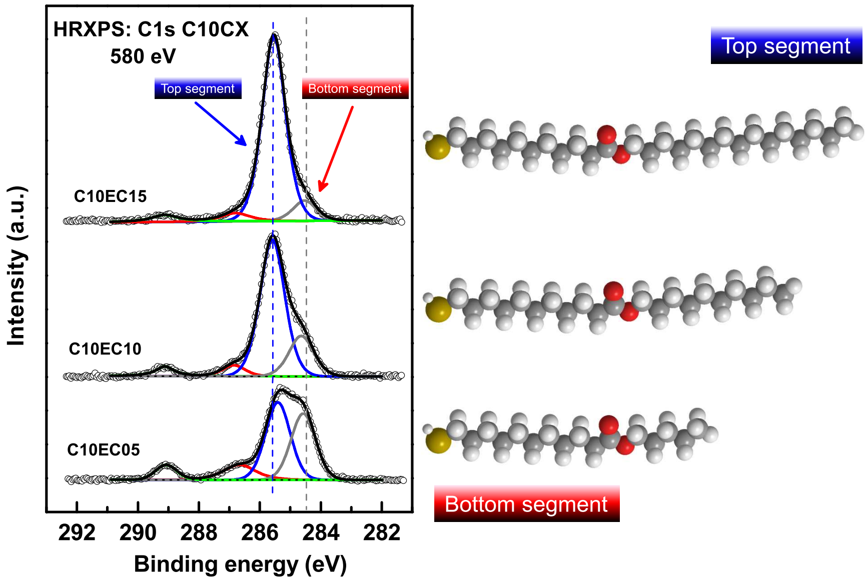

FIGURE 4.8: C 1s HRXP spectra of mid-chain ester functionalized alkanethiols of varied top segment

Variation of the top segment One of two representative examples of the embedded ester systems having a variation in the length of the top segment is shown in Figure 4.8. It has a bottom segment consisting of 10 methylene units and a top segment of variable length. The relations between the peaks related to the top and bottom segment look reasonable. With increasing length of the top segment, the inensity of the respective feature increases significantly. On the other hand, the intensity of the feature related to the bottom segment decreases with increasing length of the top segment, as can be expected. The second example regarding the length of the top segment is the system having a bottom segment of a fixed length of 15 methylene units (see Figure 4.9). Looking at the behavior of both peak components (related to the top and bottom segment) it is again obvious that the peak intensity associated with the top segment is increasing with its length whereas the peak intensity related to the bottom segment decreases with increasing length of the top segment because of the stronger attenuation of the respective signal.

Inversion of the dipole direction Here, we compare two systems having same length of both top and bottom segments but an embedded dipole of two different (opposite) directions. In the C 1s spectrum of C10EC10 all chracteristic

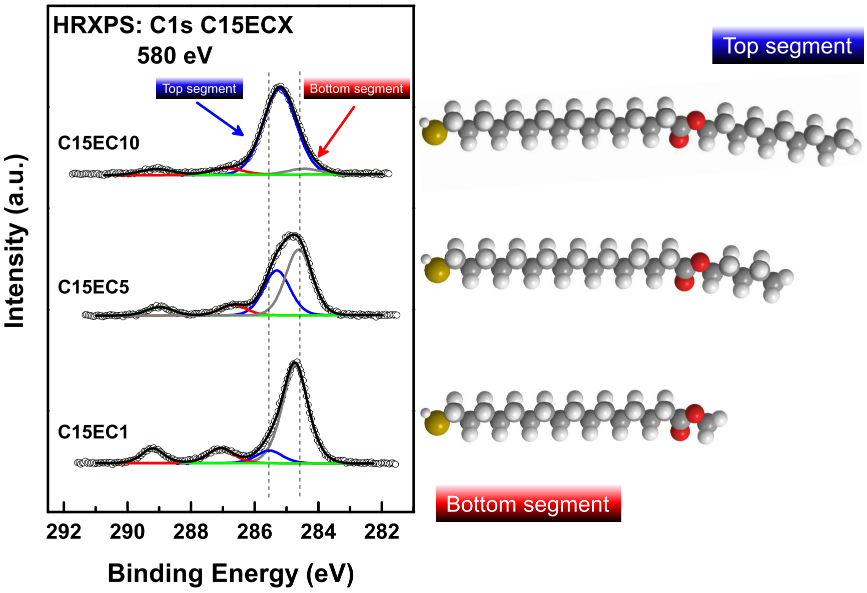

FIGURE 4.9: C 1s HRXP spectra of mid-chain ester functionalized alkanethiols of varied top segment

peak components are clearly visible. In case of the system with the reversed dipole (C10EC10 reverse) the effect of peak splitting is not clearly visible. Instead we see one main peak of the backbone shifted to lower binding energies compared to our C16 reference (-0.4 eV) (see Figure 4.10). The main C 1s backbone peak of C10EC10 is shifted to higher binding energies of about +0.57 eV compared to our C16 reference.

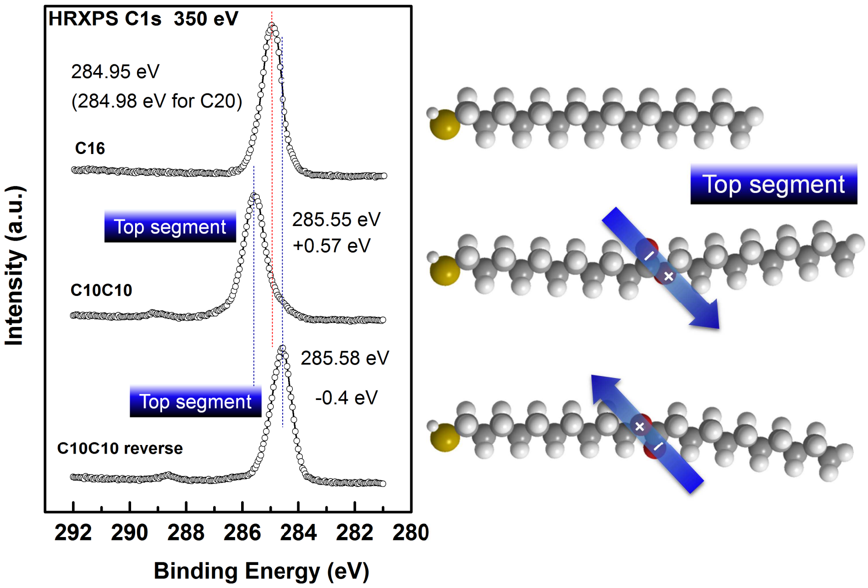

FIGURE 4.10: C 1s HRXP spectra of C10EC10, C10EC10 reverse ester and C16 reference.

4.1.2.2 Work function

An important advantage of the embedded dipole system is the possibility to vary the work function at the persistant chemistry at the SAM-ambient interface. It is essential when SAMs are used as intermediate layers to adjust the injection barrier between an electrode and organic semiconductor. The work function of each embedded ester system studied was measured by both methods. The results presented in Figure 4.11 show that there is a good agreement between the work function measured by UPS and Kelvin Probe. Overall there is a variation of the work function from +0.6 eV to -0.62 eV if we compare all measured systems. Focussing on the dipole direction inversion, i.e. comparing C10EC10 with C10EC10 reverse ester, we obtain a work function inversion, which is reasonable. The simple n-alkanethiolate adsorbates follow a linear trend of $\Delta\phi$ with number of C atoms, as observed in Figure 4.11, with a slope of -17.5 meV/C. Given the definitively established SAM structures and the well characterized and constant ester group dipole moment magnitude and direction, the variables to consider for explaining the $\Delta\phi/\Delta n$ effects are quite limited. The primary possibility involves polarizability and screening effects of the alkyl chains [122]. Alkyl chains have a dielectric constant ε=2.26 [18] and will respond to the presence of an applied bias to by

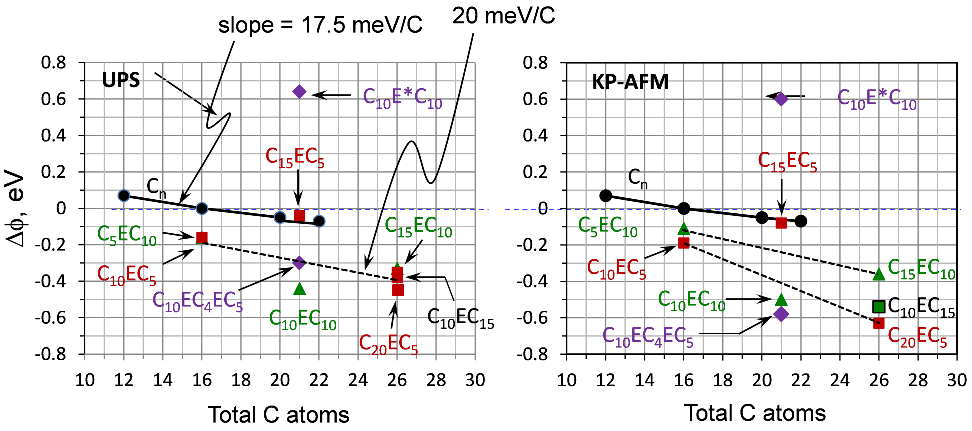

FIGURE 4.11: Graphical summary of work function data. In both panels the values of ϕ are given in terms of $\Delta\phi$, defined as the difference between the ϕ value of each SAM of a given total chain C atom number and ϕ of the corresponding unsubstituted alkanethiolate SAM. Thus for SAMs with values along $\Delta\phi = 0$ there is no shift relative to the alkanethiolate CAM while values with $\Delta\phi < 0$ correspond to SAMs with lower work functions than the alkanethiolate SAMs. The black circle points represent unsubstituted alkanethiolate SAMs and the other data points are labelled with the specific ester functionalized SAM. Left panel: the major set of data which was obtained by PES measurements at two different photon energies (see text for details). The slopes of the two main linear correlations are shown by arrows. Right panel: the smaller set of data obtained from surface potential AFM measurements. The KP-AFM data in the right panel were obtained by Orlando Cabarcos, Nichole Sullivan and Prof. David L. Allara from the Pennsylvania State University.

creating induced dipoles to screen the electric field from the ester moieties. We can view this as an effect in the z-direction (perpendicular to the surface). In the xy-direction the charge distribution also will be affected by interactions between neighboring molecules over some distance, an in-plane depolarization effect. Both of these effects, in principle, can give rise to chain length dependencies and thus need to be considered. We also can consider variations in the electrical character of the Au-S interface regions as a function of the SAM structure, but for purposes of this simple analysis we assume the interface dipole remains constant throughout the series of alkanethiolate SAM.

4.1.3 Theoretical calculations

In order to analyze and better understand the experimental results, as occuring in the photoemission spectra, calculations were performed, on the one hand, the C 1s core level energies, to compare the binding energy shift and, on the other hand, the electrostatic potential, to compare the work function values. The calculations were performed by Iris Hehn from the group of Prof. Egbert Zojer from the Graz University of Technology (Austria).

4.1.3.1 C 1s core level energies

In general the binding energy shift in the C 1s HRXP spectra could be reproduced well by the calculations of the C 1s core level energies as far as electrostatic effects are considered. Allover it can be said that the calculations mostly confirm the experimental results, except C10E*C10 reverse ester. Due to the fact that it is not clear why there is no binding energy shift in case of C10E*C10 reverse ester, we put our focus on this system. From the C 1s core level calculations a binding energy shift of ~0.7eV was found between the bottom and top segments (from HRXPS it was hardly perceptible).

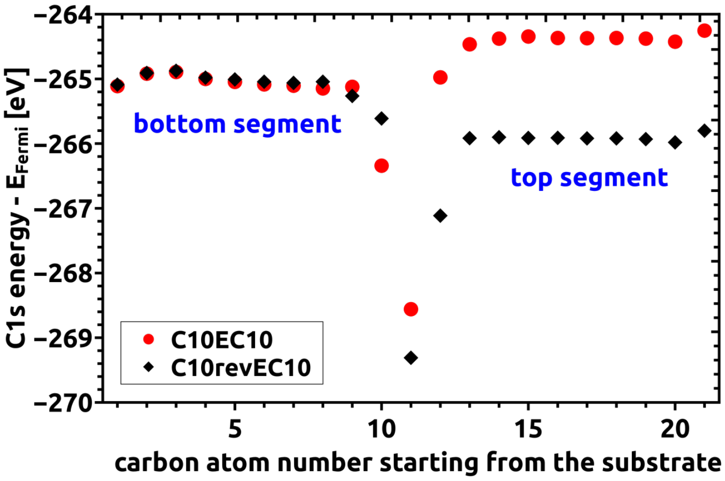

FIGURE 4.12: C 1s core level energies of C10EC10 and C10EC10 reverse relative to the Fermi energy of a full coverage C10EC10 SAM and a full coverage C10EC10 reverse SAM. [courtesy of Iris Hehn and Prof. Egbert Zojer from the Graz University of Technology]

4.1.3.2 Electrostatic potential

The calculation of the electrostatic potential could partially confirm experimental results regarding the work function. But the behavior is not fully systematic. The so-called odd-even effect with respect to the length of the bottom segment could be observed; this may be a possible explanation for the non-systematic behavior.

Focussing on C10E*C10 reverse ester we see a good correlation with the work function measurements.

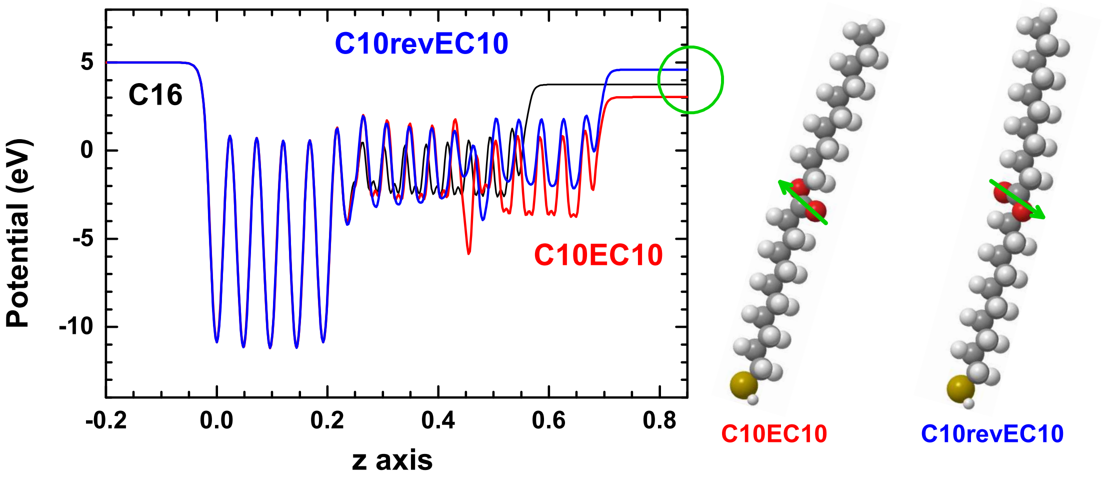

FIGURE 4.13: Electrostatic potential of 3 different systems. A C10EC10 SAM (red), a C10revEC10 SAM with reverse ester dipole (blue) and a C16 reference SAM without ester group (black). All 3 SAMs are densely packed on a Au(111) surface. The first 5 distinct peaks show the 5 layers of gold substrate, the smaller peaks after that represent the SAM. The top of the SAM is reached at a z-axis position of about 25 Å above the top gold layer. [courtesy of Iris Hehn and Prof. Egbert Zojer from the Graz University of Technology]

4.1.3.3 Comparison to the experimental results

There is a good agreement between the calculated work function and the work function measured by Kelvin Probe (and UPS). The values are not identical, but they show the correct trend. Also, the calculated XPS shift (C_{top}-C16) is mostly in good correlation with the XPS shift determined from experimental results; there is one exception as already discussed two sections before. The inversed dipole in C10E*C10 (rev.) shows almost no XPS shift in the experimental results.

	Simulation		Experiment	
System	$\Delta\Phi$	C_{top}-C_{bot}	$\Delta\Phi$	C_{top}-C_{bot}
	[eV]	[eV]	[eV]	[eV]
		screened		$h\nu = 350$ eV
C16	0.00	0.01	-	-
C10EC5	-0.6	-0.86	-0.16	-0.84
C10EC10	-0.51	-0.85	-0.44	-1.02
C10E*C10 rev.	1.02	0.7	0.64	0.00

TABLE 4.1: Work function and binding energy shift determined by simulation and experiment compared with each other.

4.2 Embedded dipoles in aromatic self-assembled monolayers

4.2.1 Basic characterization

4.2.1.1 XPS and HRXPS

Au $4f_{7/2}$, S 2p, and N 1s HRXP spectra of the TP1-down and TP1-up SAMs are presented in Figure 4.14, along with the data for the reference TP1 monolayer. The S 2p spectra of all three SAMs in Figure 4.14b exhibit a sole S $2p_{3/2,1/2}$ doublet at a binding energy (BE) position of ~162.0 eV (S $2p_{3/2}$). This value corresponds to thiolate species bound to noble metal surfaces [113, 123, 124], which means that, within the sensitivity of the measurements, all molecules in the studied films are bound to the substrate via a thiolate-gold bond, as is expected for well-defined SAMs. No traces of other sulfur derived species such as atomic sulfur, disulfides, unbound thiols or sulfonates were observed. The TP1-down and TP1-up SAMs exhibit similar intensities of the S 2p signal, along with similar intensities of the Au $4f_{7/2}$ emission (Figure 4.14a), which suggest similar packing densities in these two monolayers. These densities appear, however, slightly lower than that in the TP1 SAM, as follows from the comparison of the Au $4f_{7/2}$ intensities in Figure 4.14a. This qualitative conclusion is supported by a numerical evaluation of the XPS and HRXPS data (see section 3 for details), resulting in the values of effective thicknesses and packing densities compiled in Table 4.2. Note that the values for the reference TP1 monolayer agree well with literature data [44, 45]. Note also

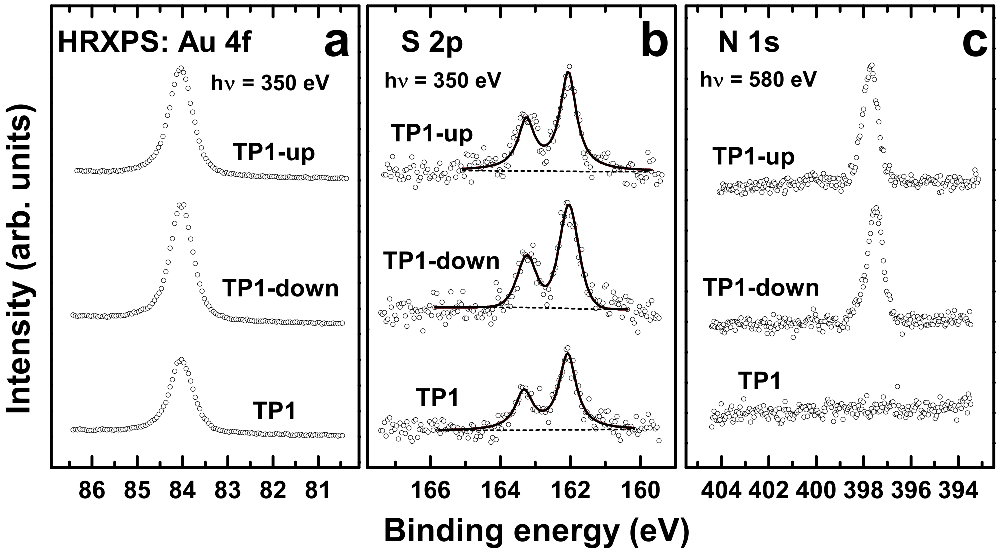

FIGURE 4.14: Au4f$_{7/2}$ (a), S 2p (b), and N 1s (c) HRXP spectra of the TP1, TP1-down and TP1-up SAMs. The spectra were acquired at photon energies of 350 eV (Au 4f7/2 and S 2p) and 580 eV (N 1s). The S 2p spectra are fitted by a single S 2p$_{3/2,1/2}$ doublet, characteristic of the thiolate.

that the effective thicknesses calculated from XPS agree with the ellipsometry data of our partners (Martin Kind from the group of Prof. Andreas Terfort from the Frankfurt University).

The N 1s HRXP spectra of the TP1-down and TP1-up SAMs in Figure 4.14c exhibit a single and sharp N 1s emission, in contrast to the expected, nitrogen-free "baseline" for the reference TP1 monolayer. This emission can be unequivocally assigned to the nitrogen atoms in the pyrimidine rings. The presence of the single and sharp peak suggests, in accordance with the S 2p data, a homogeneous and well-defined character of the target monolayers. Note that there is a small shift between the exact BE positions of the N 1s emissions for the TP1-down and TP1-up monolayers (397.5 and 397.7 eV, respectively). The C 1s HRXP spectra of the TP1-down and TP1-up films are characteristic of well-defined SAMs. These spectra are, however, strongly affected by electrostatic effects. Thus, they will be described in detail below, when discussing the electronic properties of the SAMs.

Monolayer	Effective thickness from XPS/HRXPS [nm]	Packing density [molecules/cm^2]
TP1	1.78±0.04	4.6×10^{14}
TP1-down	1.75±0.05	4.3×10^{14}
TP1-up	1.74±0.05	4.2×10^{14}

Table 4.2: XPS/HRXPS derived effective thickness of the TP1-down, TP1-up, and TP1 SAMs, along with the XPS/HRXPS derived packing density in these monolayers. The error bars of the packing density can be estimated at ±5%.

4.2.1.2 NEXAFS spectroscopy

The carbon and nitrogen K-edge NEXAFS spectra of the TP1, TP1-down and TP1-up SAMs are presented in Figure 4.15. Panels (a) and (c) compile the spectra acquired at an X-ray incidence angle of 55° while panels (b) and (d) represent the difference between the spectra acquired at X-ray incident angles of 90° and 20°. Note that 55° is the so-called "magic angle"; at this particular adjustment, the spectrum is not influenced by any effects related to molecular orientation and is, therefore, exclusively representative of the chemical composition of the samples [89]. In contrast, the difference of the spectra acquired at normal (90°) and grazing (20°) incidence of X-rays is a fingerprint of the linear dichroism and, thus, allows conclusions regarding the orientational order and molecular orientation in the systems. The 55° C K-edge spectrum of the reference TP1 monolayer in Figure 4.15a exhibits typical absorption signature of oligophenyls, in good agreement with literature data [44]. The spectrum is dominated by the intense π_1^* resonance of the phenyl rings (1) at 284.95 eV, accompanied by the respective π_2^* peak (3) at ∼288.8 eV and several σ^* resonances (4-6) at higher excitation energies [89, 125–127]. In addition, there are the R*/C-S* resonance (2) at ∼287.0 eV [44, 127] and a weak R^* feature at ∼287.8 eV (between 2 and 3). Apart from certain intensity differences, the spectra of the TP1-down and TP1-up SAMs exhibit similar resonance patterns (2-6) at high photon energies (PEs) as the TP1 monolayer. At the same time, the dominant π_1^* resonance splits in three lines at PEs of 284.85/285.0 eV (1a for TP1-down/TP1-up), 285.3 eV (1b) and 286.0 eV (1c), which is more obvious for TP1-down/Au. This splitting is associated with the effect of the embedded pyrimidine moiety. Indeed, a NEXAFS spectrum of the pyrimidine molecule is dominated by a split π_1^* resonance at PEs of 285.32 and 285.86 eV related to the

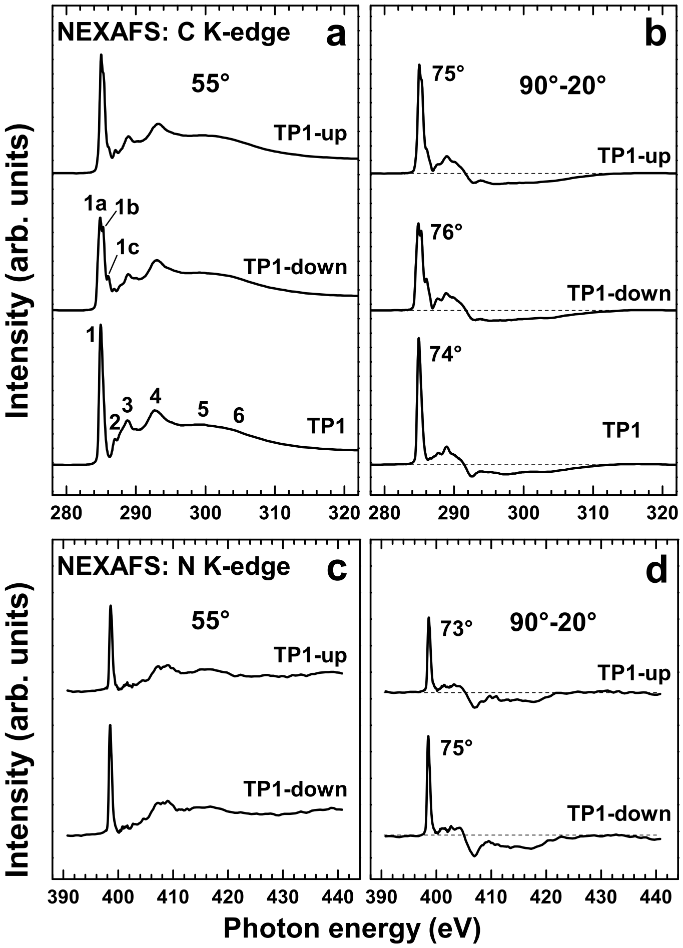

FIGURE 4.15: C (a,b) and N (c,d) K-edge NEXAFS spectra of the TP1, TP1-down and TP1-up SAMs acquired at an X-ray incident angle of 55° (a,c), along with the respective difference between the spectra collected under the normal (90°) and grazing (20°) incidence geometry (b,d). Individual absorption resonances are marked by numbers (see text for the assignments). The derived average tilt angles of the π^* orbitals of the phenyl rings (C K-edge) and embedded pyrimidine moiety (N K-edge) are given at the respective resonances. The horizontal dashed lines in panels b and d correspond to zero.

transitions from the non-equivalent carbon sites to the lowest unoccupied, antibonding, molecular orbital [128, 129]. A superposition of these features with the distinct π_1^* resonance of the phenyl rings can indeed result in the π^* resonances with the complex shapes observed for the TP1-down and TP1-up monolayers. The different relative intensities of the individual contributions within the joint π^*feature for TP1-down/Au and TP1-up/Au can be explained tentatively by the different orientations of the pyrimidine moiety with respect to the substrate. According to literature data [129], a substituent at either the 2 or the 5 position of pyrimidine results in different branching of the individual π^* resonances. The attachment to the substrate, even mediated by a phenyl ring and a thiolate group can provide a similar effect as a substitution at a particular site. Moreover, the highly localized core levels and the more delocalized frontier orbitals are affected to a different degree by the electrostatically-induced shifts that depend on the orientation of the pyrimidine groups (see below), which can also cause deviations between the NEXAFS spectra of TP1-up and TP1-down. The N K-edge 55° NEXAFS spectra of the TP1-down and TP1-up SAMs in Figure 4.15c are exclusively representative of the embedded pyrimidine moiety. They are dominated by a strong π^* resonance at 398.6 eV, accompanied by several weaker features. These spectra agree well with the spectrum of pyrimidine in the gas phase [129]. The assignments of the individual resonances can be found in reference [129]. Both C and N K-edge NEXAFS spectra of the TP1-down and TP1-up SAMs exhibit a pronounced linear dichroism, as seen in Figures 4.15b and 4.15d. This indicates a high orientational order in these films. Considering that the intensity of the π^* resonances is larger at normal than at grazing incidence (positive peaks in the difference spectra) and that the TDMs of these resonances are directed perpendicular to the phenyl and pyrimidine rings, an upright orientation of the molecular backbones in the target films can be concluded, in agreement with the XPS/HRXPS, ellipsometry, and IR data. This is supported by the numerical evaluation of the entire set of the NEXAFS spectra within the standard theoretical framework [89]. A similar procedure as for analogous aromatic SAMs was used to evaluate the dependencies of the intensity of the most prominent π^* resonances at the C and N K-edges on the incidence angle of the X-rays, fitting them to the theoretical curves for a vector-like orbital [127, 130]. The only fitting parameter was the average tilt angle of the respective molecular orbitals, α. The derived values of this parameter for the π^* resonances of the entire molecular backbone at the C K-edge and the π^* resonance of the pyrimidine moiety at the N K-edge are given in Figures 4.15b and 4.15d, at the respective absorption resonances. Significantly, the average tilt angles derived from the C and N K-edge data for both TP1-down and TP1-up SAMs are almost identical, suggesting a planar or close-to-planar molecular conformation of the aromatic backbones. Finally, based on the α values and a reasonable assumption for the twist angle, γ (32°)[131], the tilt angles of the entire molecular backbones in the target and reference SAMs, β, were calculated using the standard formula, $cos\alpha = sin\beta \times cos\gamma$[94]. They are 17°, 18°, and 18° for TP1-down/Au, TP1-up/Au, and TP1/Au, respectively; the error bars can be estimated at ±3°.

4.2.1.3 Additional characterization

In addition to our spectroscopic characterization, the TP1, TP1-up and TP1-down SAMs were characterized by complementary infrared spectroscopy and scanning tunneling microscopy measurements [108]. The corresponding measurements were performed by Martin Kind (IR) and Adrian Wiesner (STM) from the group of Prof. Andreas Terfort from the Frankfurt University. From the IR spectroscopy measurements of the TP1-down and TP1-up monolayers the tilt angles of 12° and 18° and twist angles of 28° and 37°, respectively, could be determinded, though with relatively large error bars (±5°) due to low intensities of the ⊥ and oop bands. This problem was exacerbated for the TP1 SAM to the extent that the values of twist angle β and tilt angle γ could not be derived. Note also that this discussion and the evaluation of tilt and twist angles assumes that the three aromatic rings are coplanar. This assumption is based on the fact that the dihedral rotation typical of biphenyls and terphenyls in the molecular state ($\sim$ 40°) [132, 133] is strongly reduced or even eliminated completely in densely packed 2D assemblies due to intermolecular interactions [131, 134–136], as supported by the literature data [137, 138] and corroborated, in this case, by the NEXAFS results discussed before.

From the STM measurements the molecules in the TP1 SAMs were found to adopt a commensurate $(2\sqrt{3} \times \sqrt{3})$R30° arrangement on the Au(111) terraces with the presence of etch pits of ~0.24 nm depth, corresponding to a local absence of a gold monolayer. The films formed by the TP1-up molecules look very similar to TP1/Au at first sight. In particular, many monoatomic etch pits can be found. However, these etch pits are on average smaller and more numerous than for TP1/Au, limiting the size of the ordered domains to 10 nm. Nevertheless, molecular resolution could be attained, revealing an approximately hexagonal pattern. In the case of the TP1-down structure the etch pit appearance is similar to TP1-up/Au, again limiting the size of the crystalline areas. While the dimensions of the unit cell are basically the same as for TP1/Au and TP1-up/Au, the arrangement of the molecules looks somewhat different. This arrangement can be derived from the TP1-up structure by moving every other row one binding site along the <11-2> direction (by 0.12 nm, from a formally hcp to a fcc site or vice versa). This results in an almost square placement of the adsorbates, which, however can again be described as a centered $(2\sqrt{3}\times\sqrt{3})$R30° structure, due to the formal nonequivalence of the adsorption sites. In any case, the packing density in the TP1-down case as well as the surface unit cell are basically the same as for TP1/Au and TP1-up/Au, in agreement with the spectroscopic data presented above.

4.2.2 Electrostatic effects

4.2.2.1 Photoemission

The C 1s HRXP spectra of the TP1-down and TP1-up SAMs are presented in Figure 4.16, along with the data for the reference TP1 monolayer. The spectra are tentatively decomposed into several individual peaks. The curves for a PE of 350 eV can be directly compared. In accordance with literature data [44, 139], the spectrum of TP1/Au shows a strong and sharp emission at ∼284.25 eV accompanied by a weak shoulder at ∼284.95 eV assigned to the terphenyl backbone and shake-up processes in the aromatic matrix, respectively [139]. The major emission contains contributions from all carbon atoms along the molecular chain, merging in a single sharp line [113], but its BE position is mostly representative of the ambient-adjacent phenyl ring since the photoemission signals from the central and substrate-adjacent rings are strongly attenuated at the given kinetic energy (∼60 eV at a PE of 350 eV) [35, 140]. In contrast, the spectra of the TP1-down and TP1-up SAMs exhibit much more complex patterns that cannot be explained by the presence of the pyrimidine ring within the standard concept of a chemical shift. Indeed, according to the reference measurements on 2-mercaptopyrimidine (2-MPM/Au, a single "pyrimidine-up" unit bearing a thiol; see the Supporting Information, Figures S6 and S7) which, in terms of the branching, agree with the literature data for pyrimidine in the gas phase [128], the spectrum of the pyrimidine moiety comprises two emissions at BEs of 285.0 and 286.4 eV having an intensity relation of 3:1. In the case of TP1-down/Au and TP1-up/Au, the respective emissions can appear at somewhat different binding energies but, most importantly, should be weak compared to the contribution from the ambient-adjacent phenyl ring. The latter is naturally associated with the prevalent peak (shaded in blue) in the 350 eV spectra of the TP1-down and TP1-up SAMs with a BE of 283.83 eV and 284.90 eV, respectively. This association, however, means that the emission of the ambient-adjacent ring shifts by −0.42 eV for TP1-down/Au and +0.65 eV for TP1-up/Au compared to TP1/Au. The origin of this shift cannot be chemical but only electrostatic since the only difference between the TP1-down and TP1-up molecules is the direction of the polar pyrimidine moiety. Note that a weak electron withdrawing effect, associated with the adjacent nitrogen atoms in the case of the TP1-down SAM, cannot produce a BE shift of such a magnitude over the entire ambient-adjacent ring. As far as the signals originating from carbon atoms

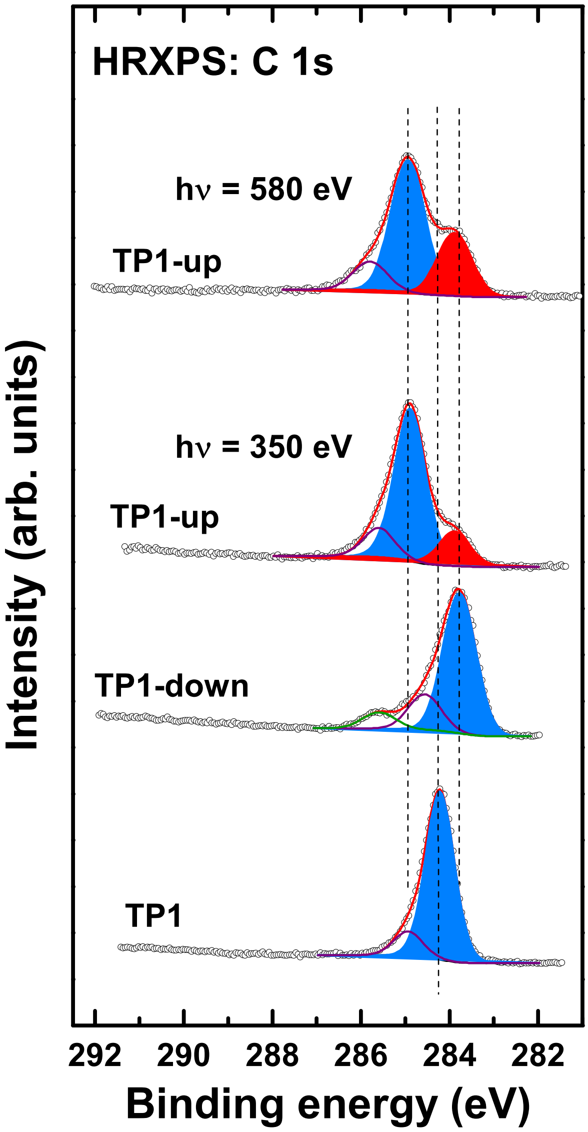

FIGURE 4.16: C 1s HRXP spectra of the TP1, TP1-down and TP1-up SAMs acquired at photon energies of 350 eV and 580 eV (top spectrum; for TP1-up/Au only). The spectra are tentatively decomposed in several individual components (see text for details). The components predominantly associated with the ambient-adjacent and substrate-adjacent phenyl rings are marked by blue and red colors, respectively. The components associated with the pyrimidine ring are drawn by thin solid lines, as far as they do not overlap completely with the other features. The vertical dashed lines are guides for the eyes.

residing in the other rings are concerned, features at higher binding energies are tentatively associated with the pyrimidine and shake-up processes (vide supra). The low BE peak at 283.85 eV that is clearly resolved in the TP1-up spectrum is associated with the substrate-adjacent ring. Screening of the photoemission hole by the electrons in the metal substrate is particularly strong and relevant for the energetic position of that peak [113] resulting in a shift to lower binding energies. Conversely, the position of that peak is not subject to electrostatic shifts caused by the pyrimidines, as these reside at larger distances from the substrate (see below for a detailed discussion). This observation explains, why the 283.85 eV peak is best resolved in the TP1-up case, where the screening induced shift of the peak associated with the substrate-adjacent ring and the electrostatic shifts affecting the BE position of the dominant feature associated with the ambient-adjacent ring go in opposite directions. In the TP1-down case, where both shifts go in the same direction, those two features overlap. The assignment that the lowest-binding energy peak originates from the carbon atoms “buried” in the monolayer is in fact supported by the spectrum shown in the top panel of Figure 4.16. There, the intensity of the lowest BE emission is shown to increase significantly upon increasing the kinetic energy of the photoelectrons (PE = 580 eV) due to a weaker attenuation of the respective signal [140].

4.2.2.2 Work function

Work function (WF) values for TP1/Au, TP1-down/Au, and TP1-up/Au with respect to the WF of freshly sputtered gold, measured with a Kelvin probe and derived from the secondary electron cutoffs of the ultraviolet photoemission spectra, are presented in Figure 4.17 and compiled in Table 4.3, together with the theoretical values obtained from the DFT calculations (vide infra). The experimentally observed WF change upon the assembly of the TP1 monolayer compared to clean Au(111) correlates well with the literature value for the analogous molecular films, viz. $-(0.8\text{-}1.0)$ eV [141]. Most significantly, compared to the WF of TP1/Au, TP1-down/Au and TP1-up/Au exhibit changes of $+0.55$ and -0.43 eV according to the Kelvin probe, and $+0.58$ and -0.41 eV, according to the ultraviolet photoemission spectroscopy (UPS). This clearly manifests the electrostatic effect of the embedded dipoles.

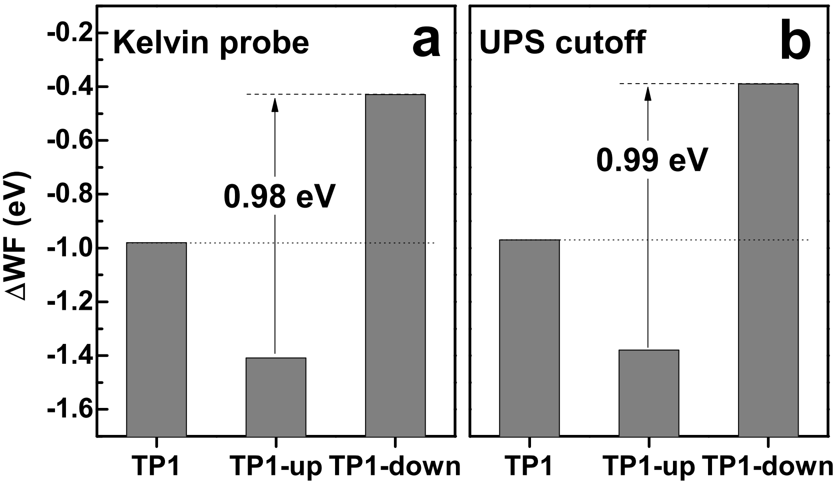

FIGURE 4.17: Work function values for TP1/Au, TP1-down/Au, and TP1-up/Au measured with a Kelvin probe (a) and as the cutoff of the UP spectra (b). The values are references to the WF of freshly sputtered gold. The difference between the values for TP1-down/Au and TP1-up/Au is highlighted by blue arrows and precisely marked.

Monolayer	Kelvin Probe [eV]	UPS cutoff [eV]	DFT [eV]
TP1	-0.98	-0.97	1.30
TP1-down	-0.43 (+0.55)	-0.39 (+0.58)	-0.54 (+0.76)
TP1-up	-1.41 (-0.43)	-1.38 (-0.41)	-1.99 (-0.69)

TABLE 4.3: Experimental (Kelvin probe and secondary electron cutoff in UPS) and calculated (DFT) WF changes induced by the TP1, TP1-down, and TP1-up SAMs, with respect to the WF of pristine gold. The WF shifts with respect to TP1/Au are presented in parentheses. The DFT values were calculated by David A. Egger and Prof. Egbert Zojer from the Graz University of Technology.

4.2.2.3 Band-Structure-Calculations

This work was performed by David A. Egger from the group of Prof. Egbert Zojer from the Graz University of Technology (Austria) [108].

The main impact of the pyrimidine rings on the electronic structure of the SAM-substrate interface can be seen in Figure 8a, where the calculated plane-averaged electrostatic energies of TP1, TP1-up, and TP1-down SAMs on Au(111) are shown. For the substrate-adjacent phenyl ring the electrostatic energies in the three systems coincide, while the electronic landscape experienced by the ambient-adjacent ring is shifted considerably in the TP1-up and TP1-down SAMs due to the aligned pyrimidine dipoles. This has two consequences of direct relevance for the properties discussed here: First, the vacuum level above the SAM is shifted significantly, with SAM-induced WF shifts (ΔWF) of -1.30 eV for the TP1 SAM, -0.54 eV for the TP1-down SAM, and -1.99 eV for the TP1-up SAMs, respectively. These values, summarized in Table 3, are in good semi-quantitative agreement with the experimental results. More importantly, from the electrostatic energies shown in Figure 8a, one can understand why embedding the dipole in the TP1-down fashion leads to an increase of the WF compared to TP1 (the reference system containing no pyrimidine unit), while inserting it in the TP1-up orientation yields a more pronounced WF decrease. Quantitatively, the effect of reversing the orientation of the embedded pyrimidine dipole results in a WF difference between the TP1-down and TP1-up layers amounting to $\Delta \mathrm{WF}^{calc}$=1.45 eV. This shift is somewhat larger than the one measured in the UPS experiments ($\Delta \mathrm{WF}^{UPS}$=0.99 eV) and Kelvin probe measurements (ΔWFKP=0.98 eV). Possible reasons for this deviation are discussed in the next section. The second immediate consequence of the shift in the electrostatic energy induced by the pyrimidine dipoles is a change in the energies of the core-levels along the backbone of the SAM constituents. The calculated energies of the C 1s states in the aromatic system relative to that of the carbon atom in the methylene linker are shown in Figure 8b. One sees that the energies of the core levels are shifted between the substrate-adjacent and ambient-adjacent rings in accordance with the shift in the potential energy shown in Figure 4.18a. The core-levels of the carbon atoms bound to nitrogens are shifted to larger binding energies, which is a consequence of the changed bonding situation of those atoms (cf. data points in Figure 4.18b highlighted by rectangles). Consequently, these shifts can be regarded as standard "chemical shifts" while the energy differences between the carbon atoms comprising the ambient-adjacent and substrate-adjacent phenyl rings must be regarded as "electrostatic shifts". For a quantitative comparison of the calculated core-level energies to the binding energies measured by HRXPS, in general, screening effects associated with the core-hole produced in the photoionization process also need to be considered. For signals arising from the ambient-adjacent ring, these effects are, however, comparably small keeping in mind the highly non-linear dependence of screening on the distance from the metal surface. A first estimate of the energy correction can be obtained by means of a classical image potential [142], using an image plane position that is located at 0.09 nm above the top row of the gold atoms [143]. This yields only comparably small and, most importantly, very similar screening-induced shifts of 0.30 eV for the lowest and 0.24 eV for the topmost C atom of the ambient-adjacent ring of the TP1 system (these numbers change to 0.10 V and 0.08 eV when using

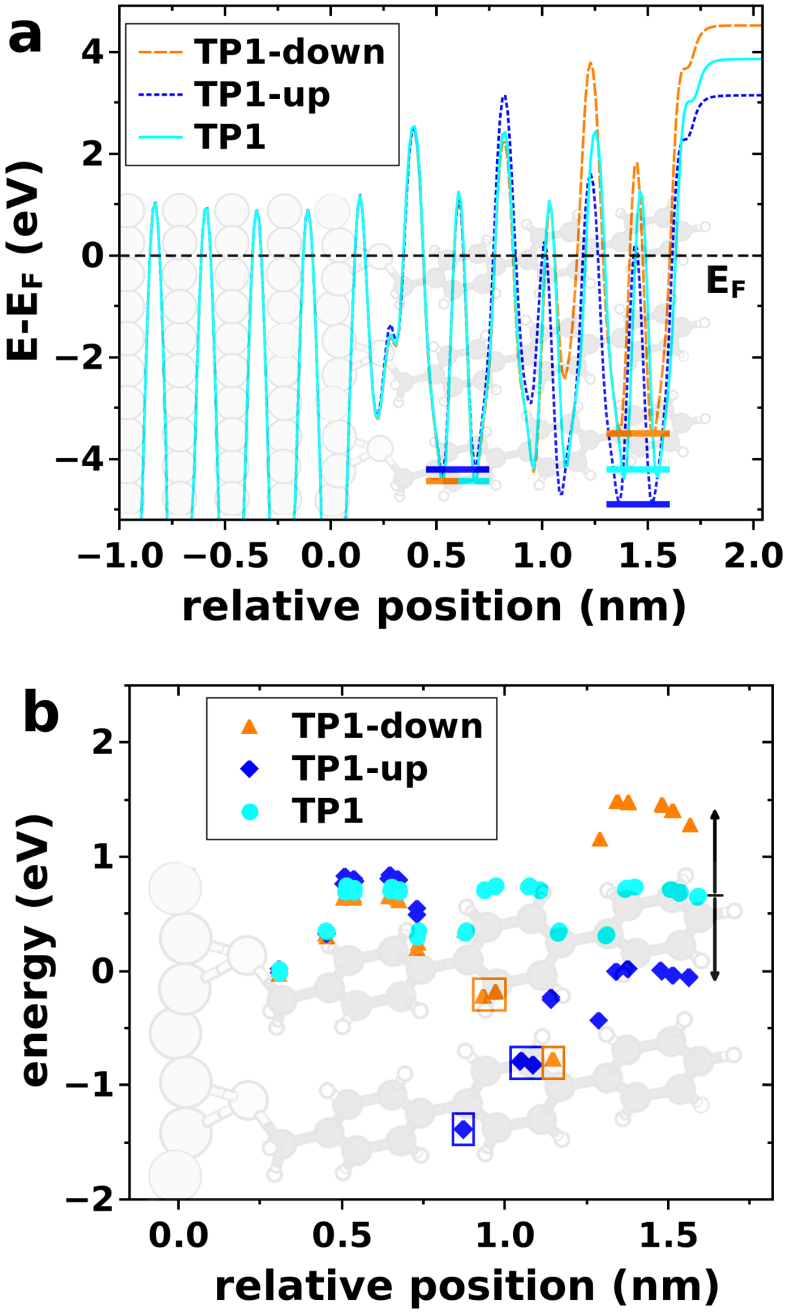

FIGURE 4.18: (a) Calculated plane-averaged electrostatic energy of an electron across TP1/Au (cyan solid line), TP1-up/Au (blue dotted line), and TP1-down/Au (orange dashed line). The origin of the x-axis is set to the topmost metal layer while the energy scale is aligned to the Fermi energy of the substrate (see dashed horizontal line). Thick, color-coded, horizontal lines serve to illustrate the difference in electrostatic energy below and above the pyrimidine ring. (b) Calculated C 1s core-level energies of TP1/Au (cyan circles), TP1-up (blue diamonds), and TP1-down/Au (orange triangles). The origin of the x-axis is set to the top metal layer while the energy scale is aligned to the C 1s energy of the first carbon atom in each system. Framed data points correspond to the carbon atoms bound to nitrogen, and the vertical arrows indicate the difference in the core-level energies corresponding to the ambient-adjacent phenyl ring of the TP1-up and TP1-down SAMs. [courtesy of David A. Egger and Prof. Egbert Zojer from the Graz University of Technology]

a scalar dielectric constant of 3 for the SAM instead of only using the vacuum permittivity). Moreover, it needs to be kept in mind that these shifts do not affect a comparison of the features of the various SAMs that arise from C atoms at equivalent distances to the substrate. Thus, a comparison of the relative core-level shifts in the ambient-adjacent ring to the measured shifts of the dominant HRXPS feature appears sensible. The calculated upward-shifts of the core-levels by +0.74 (+0.62) eV for TP1-down/Au (resulting in a reduction of the C 1s binding energies) and the downward shift by -0.73 (-0.71) eV in the TP1-up/Au case (effectively increasing the C 1s binding energies) are in good agreement with the experimental data. Note that the shifts quoted here are obtained by averaging over the core-level energies of the C atoms in the ambient-adjacent ring, while the values in parentheses are obtained, when just considering the topmost C atom of this ring. In passing we note that as far as the intra-molecular structure within the SAMs is concerned, no major differences between TP1 and TP1-up and also TP1-down are observed: In particular the inter-ring twist-angles are essentially the same in all systems and between all rings. I.e., they vary between 12° and 6° with the largest values occurring in systems, where ortho-hydrogens cause some repulsion. This overall close-to-planar structure is a consequence of the significant intermolecular interactions in the densely packed layers. For example, biphenyl (as an example for oligophenylenes) displays an inter-ring twist angle of 42° in the gas phase [133], while experimental data on terphenyl in the crystalline state indicate an interring twist of only 12° [134], fully consistent with band-structure calculations [144]. The dominant role of intermolecular interactions for the twist angles in the SAMs considered here is supported by simulations of isolated TP1-up and TP1-down molecules, for which we find that the steric repulsion between ortho-hydrogens results in an inter-ring twist of 36°-37° between the respective rings. Conversely, parts of the molecules where the N-atoms of the pyrimidines are engaged in H-bonds with opposing ortho-hydrogens, are planar.

4.2.3 Mixed films

In order to further tune the work function on metal surfaces, we prepared mixed films of certain ratios of TP1-up and TP1-down. As visible in Figure 4.19 the work function of the mixed films can be tuned in a more precise way by choosing a certain ratio. Depending on the mixing ratio the work function is changing. With an increasing amount of TP1-down the work function is increasing. The increase

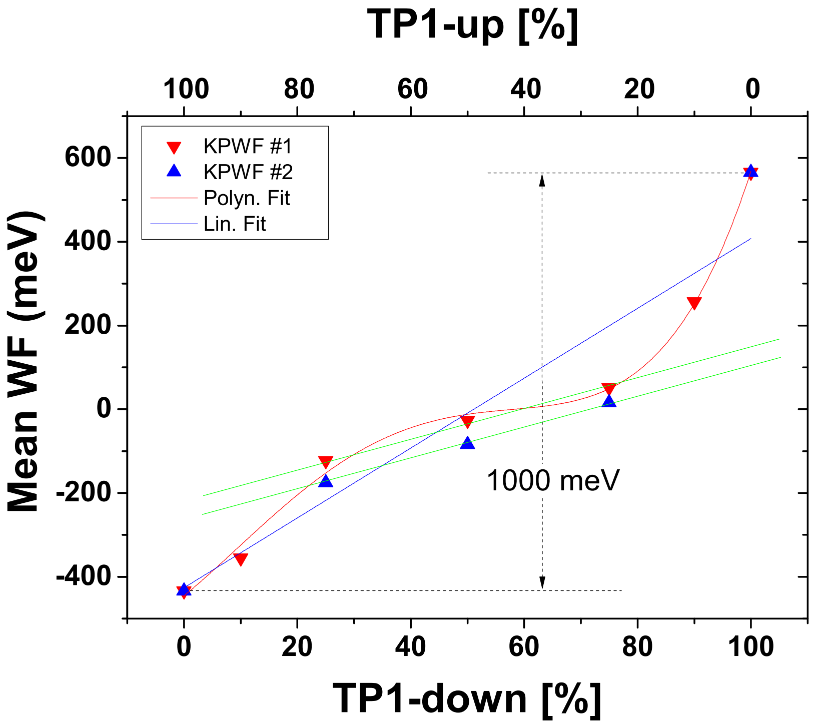

FIGURE 4.19: Work function of TP1-up/down mixed films

shown in Figure 4.19 is, however, not linear (only to some extent). Work function measurements were performed twice, to verify the results. The measured HRXP spectra of the mixed films are shown in Figure 4.20a. In Figure 4.20b calculated spectra of the mixed films, based on the 100% TP1-up/down spectra, are shown, as they theoretically should be expected. But the measured photoemission spectra (Figure 4.20a) are completely different from the expected, calculated ones (Figure 4.20b). The measured spectra give us the information that the existing homogeneous electric field in the SAM-ambient interface is changing with the increasing amount of TP1-down like shown in Figure 4.20a and thus there is a shift in binding energy of each film to lower binding energies, visible in the C 1s HRXP spectra.

4.2.4 Discussion

As stated in the introduction, the major goal of this study was to realize a model SAM-mediated interface that permits control of the work function while retaining the surface chemistry and basic structural motif of the SAM-forming compounds. It was particularly important to deal with aromatic monolayers since they possess

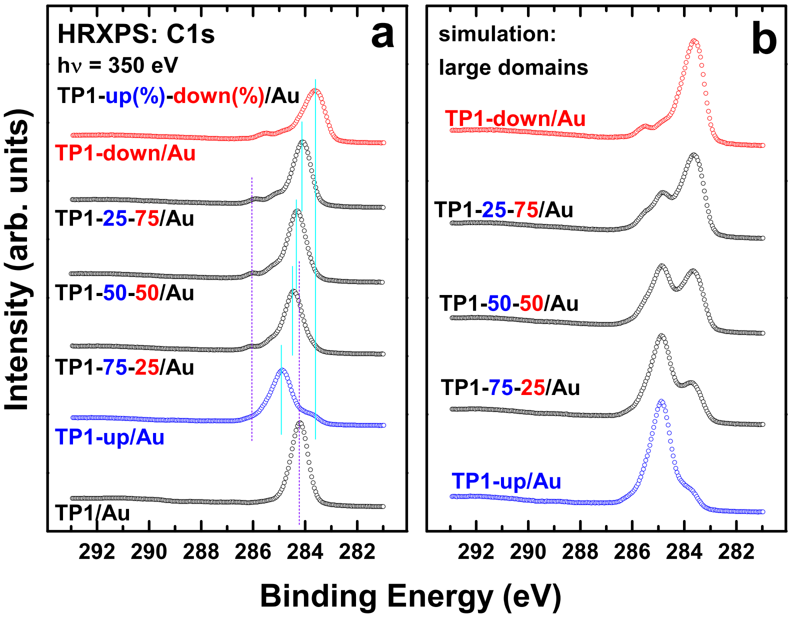

FIGURE 4.20: HRXP spectra of the TP1-up/down mixed films. In (a) the measured photoemission spectra are plotted for each mixing ratio; in (b) calculated spectra of the mixed films based on the measured TP1-up/down references

superior transport properties and provide a good match to organic semiconductors. As shown above, such monolayers can be successfully formed in a well-defined fashion. Significantly, the results of the complementary experimental techniques agree well with each other providing a consistent and detailed description of the systems studied. According to the HRXPS data (Figure 4.14 and Table 4.2), all molecules in the TP1-down and TP1-up SAMs are bound to the substrate via the thiolate anchor. The monolayers are densely packed and exhibit effective thicknesses close to the molecular length of the respective precursors (∼1.5 nm), with addition of the S-Au bond length (0.24 nm) [145, 146]. This suggests an almost upright orientation for the TP1-down and TP1-up molecules in their respective SAMs, similar to TP1/Au [45, 46]. Indeed, both IRRAS and NEXAFS data confirm that orientation. In particular, the analysis of the IR data yields tilt angles of 12° and 18° and twist angles of 28° and 37° for the TP1-down and TP1-up monolayers, respectively. In agreement, the evaluation of the NEXAFS data (Figure 4.15) results in an average tilt angle of 17°-18° for both TP1-down and TP1-up SAMs, making a reasonable assumption regarding the value of the twist angle, viz. 32°, which is characteristic of bulk terphenyl [131] and close to the average of the IR derived angles. Significantly, the tilt angles derived from the spectra representative of the phenyl and pyrimidine rings (C and N K-edges, respectively) practically coincide (Figure 4.15), which suggests a planar or close-to-planar molecular conformation in both TP1-down and TP1-up monolayers, as expected for densely packed aromatic SAMs[137]. The calculated tilt angles of 13° (TP1-up) and 12° (TP1-down) also agree well to the experimental ones. In the context of this manuscript it is important that these tilt angles are practically identical to that of the reference TP1 monolayer because it implies that the inclusion of a pyrimidine moiety into the terphenyl backbone does not significantly change the molecular orientation in the respective SAMs. The consequences of the dense packing triggered by van der Waals and electrostatic interactions between the molecular backbones are obviously stronger than the dipole-dipole repulsions favoring a significant tilt[147, 148]. Certain differences in the details of the lateral packing between the TP1-down and TP1-up SAMs do, however, occur as can be seen in the STM data. At the same time, the acquired data confirm high quality and dense molecular packing in the TP1-down and TP1-up monolayers. The SAMs are shown to exhibit ordered molecular lattices on the Au(111) surface that are close to the $(2\sqrt{3}\times\sqrt{3})R30°$ "parent" structure of the TP1 monolayer[41–43, 45]. This results for all three SAMs in packing densities of $\sim 4.6\times 10^{14}$ molecules/cm^{-2}, corresponding to 0.216 nm^2 per molecule. For the TP1 SAMs, these STM derived packing densities are fully consistent with the insight gained from the XPS/HRXPS and ellipsometry data (Table 4.2). In the latter two experiments, a slightly reduced packing density is, however, observed for the TP1-up and TP1-down SAMs compared to the reference TP1 monolayer. In conjunction with the STM data, we attribute this to the high number of etch pits seen for the TP1-up and TP1-down SAMs, giving rise to a larger amount of domain boundaries that are potentially packed less densely. This directly affects the packing density values obtained in the XPS/HRXPS and ellipsometry experiments, which average over macroscopic sample areas. In contrast, STM typically focuses on the properties within highly ordered domains for quantitative evaluation. The above analysis qualifies the TP1-up and TP1-down SAMs along with the reference TP1 monolayer as well defined model systems to study the electrostatic effects of the embedded dipole in aromatic monolayer films. The most important electrostatic effect, defined as a major goal of the present study and observed here for the first time, is a WF variation induced by the embedded dipole that can be varied by changing the orientation of the pyrimidine ring. As listed in Table 4.3, the TP1-up and TP1-down SAMs yield WF changes of +0.55 (+0.58) and −43 (−0.41) eV with respect to the non-polar TP1 monolayer, as determined by the Kelvin probe (UPS cutoff) measurements. The directions of the WF changes correlate perfectly with the orientations of the dipole moment of the embedded pyrimidine moiety, which is one more evidence that this moiety is the cause of the observed changes. This is also fully confirmed by the DFT calculations (Figure 4.18a and Table 4.3). These simulations intrinsically consider an optimized tilt angle of the molecular dipoles as well as depolarization effects originating from the polarization of the molecular electron cloud due to the combined electrical fields of the surrounding dipoles. The latter effect has been shown to severely limit the achievable WF changes when assembling dipoles in parallel arrays [149–151]. For example, Wang et al. [152] have estimated the depolarization-induced reduction of ΔWF in -NH_2 tail group substituted oligophenylene SAMs to amount to a factor of ca. 3.5. In the present case, where a polarizable medium is located below and above the embedded dipoles, this effect could even be larger. Nevertheless, simulations predict sizable WF shifts of +0.76 and -69 eV for the TP1-down and TP1-up films, respectively. These values are somewhat larger than the experimental values in spite of similar tilt angles and packing densities. We attribute that, on the one hand, to the fact that the boundaries between the monocrystalline domains and other film imperfections caused, e.g., by etch pits cannot be accounted for in the simulations (cf., above discussion of reduced packing density of the TP1-up and TP1-down films). That this is related to the too large calculated WF shifts is supported by the observation that especially for the TP1-up SAM, where the dipoles due to the thiolate docking group and the pyrimidine point in the same direction, the absolute magnitude of ΔWF is overestimated most severely (cf., Table 4.3). On the other hand, certain methodological shortcomings cannot be excluded bearing in mind that (semi)local functionals are known to yield a less than perfect description of molecular dipole moments and polarizabilities (for a recent benchmarking study for organic molecules see reference [153]). Another electrostatic effect of the embedded dipole is the shifts in the BE position of the C 1s emission associated with the ambient-adjacent phenyl ring in the molecular backbone (Figure 4.16). As mentioned in the introductory section, a similar effect has been observed for alkanethiolate SAMs with a mid-chain embedded ester group (upward dipole direction only)[30]. This, in fact, underlines the generality of this phenomenon and its independence of the backbone character. The values of BE shifts are -0.42 eV and +0.65 eV for the TP1-down and TP1-up SAMs compared to the reference TP1 film, while the calculated BE shifts amount to

-0.74 eV and +0.73 eV, when averaging over all C atoms in the ambient-adjacent ring, and -0.62 and +0.71 eV, when considering only the topmost C atom (cf., Figure 4.18b; note that a downward shift of the energy of a core level results in an increase of the binding energy and vice versa). Again, the direction of the shift correlates perfectly with the direction of the embedded dipole. As mentioned above, the occurrence of this shift (along with the electrostatic effects observed in XP spectra of several different SAM systems) [31–34] cannot be explained solely on the basis of chemical shifts, where the only origin for differences in the binding energies is assumed to lie in the local chemical environment of an atom. This applies perfectly to conductive samples connected electrically to the spectrometer, where no electric fields (and, thus, local potential energy gradients) can occur. In dielectric samples, the situation is fundamentally different: There, for example, aligned dipole layers can induce a shift of the electrostatic energy between different regions of the sample as illustrated in Figure 4.18a. This change in the local energy results in a concomitant local shift of the positions of the core levels (see Figure 4.18b). Accordingly, a decrease in the electrostatic energy results in a shift of the photoemission line to higher binding energies, with the opposite being true for an increase in the electrostatic energy. This is exactly what we observe in the C 1s HRXP spectra of the TP1-down and TP1-up SAMs in Figure 4.16. In that sense, XPS core levels act as an efficient probe of the local electrostatic environments for a particular chemical species. The electrostatic shifts are superimposed with "traditional" chemical shift associated in our case with the nitrogen atoms of the pyrimidine ring. Interestingly, in the present case, the shift in the photoemission peaks associated with the ambient-adjacent ring correlates well with the WF changes induced by the pyrimidine-containing SAMs (compared to the TP1 SAM as a reference). In view of the model described above, this observation can be rationalized by the fact that both the shifts in the photoemission peaks as well as the respective relative WF changes are caused by the parallel arrangement of the pyrimidine dipoles and the resulting modification of the potential-energy landscape. That this works out so smoothly is related to two additional effects that have not been mentioned so far: First, these potential energy shifts occur quite abruptly, which is an electrostatic peculiarity: Natan et al. [122] have shown that the decay length of the electric field caused by an arrangement of point dipoles is nearly an order of magnitude shorter than the inter-dipole distance. Secondly, the charge transfer between the substrate and the core hole is a comparably slow process on the timescale of the photoemission both in aliphatic [154] and aromatic

[155] SAMs. Especially, when considering photoionization of the carbon atoms in the ambient-adjacent ring it is reasonable to assume that the filling of the core-hole will happen at even longer timescales. Thus, the primary source of screening is polarization of the conducting substrate (see above). Metal-to-molecule charge transfer processes are not expected to affect the measured XPS binding energies. Consequently, the electrostatic shift of the energetic positions of the C 1s orbitals, that can be inferred from the calculated potential energy distributions, directly maps onto shifts of the measured binding energies.

4.3 Azobenzene-Substituted Alkanethiolate Self-Assembled Monolayers

4.3.1 High-Resolution X-ray Photoelectron Spectroscopy

S 2p, C 1s, and N 1s HRXP spectra of H-azo-C3/Au and H-azo-C4/Au are presented in Figure 4.21. The S 2p spectra in Figure 4a exhibit a single S $2p_{3/2,1/2}$ doublet at 162.0 eV (S $2p_{3/2}$) commonly assigned to the thiolate moieties [113, 123], with no traces of atomic sulfur, disulfide, unbound thiol, or oxidative species. This means that all the molecules in the H-azo-Cn films are attached to the substrate over the thiolate anchor, corresponding to the typical SAM architecture. The C 1s spectra of H-azo-Cn/Au in Figure 4.21b exhibit a single, slightly asymmetric emission at a BE of 284.1-284.2 eV, with no trace of contamination such as CO or COOH. The emission stems predominantly from the azobenzene moiety since the signal from the short aliphatic linker is strongly attenuated at the given photon energy [35]. The asymmetry of the C 1s emission is most likely related to the electronegativity of nitrogen affecting the adjacent carbon atoms, which results in the appearance of a shoulder at the high BE side of the main peak [156]. A superposition of the main peak and the shoulder results then in an appearance of the joint asymmetric peak. The N 1s spectra of H-azo-Cn/Au in Figure 4.21c exhibit a single, symmetric emission at a BE of 399.3-399.4 eV, assigned to the nitrogen atoms of the azobenzene moiety [59, 156]. The intensities of both C 1s and N 1s signals for H-azo-C3/Au are somewhat higher than the respective intensities for H-azo-C4/Au, which suggest, in agreement with the STM data (see previous Section), higher packing density for the former monolayer. Accordingly, a

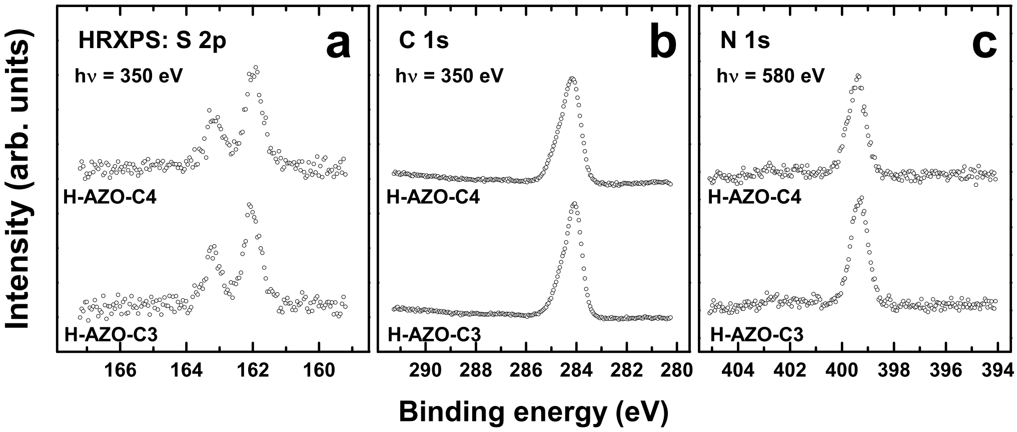

FIGURE 4.21: S 2p (a), C 1s (b), and N 1s (c) HRXP spectra of H-azo-C3/Au and H-azo-C4/Au. The photon energies are given in the panels.

fingerprint of the packing density - effective thickness - was found to be ∼15.0 and ∼13.0 Å for H-azo-C3/Au and H-azo-C4/Au, respectively, with the former value being noticeably higher than the latter in spite of the shorter molecular length of H-azo-C3 (14.6 Å) compared to H-azo-C4 (15.8 Å). On the basis of the above values, the difference in the packing density between H-azo-C3/Au and H-azo-C4/Au could be estimated at ca. 14-15%, in excellent agreement with the STM-derived value (∼14.2%). Note that, apart from the packing density difference, the effective thickness values for H-azo-C3/Au and H-azo-C4/Au are more or less close to the respective molecular lengths plus the length of S-Au bond (2.4 Å) [145, 146], assuming an upright molecular orientation in both monolayers. The difference between the thickness and molecular length is larger for H-azo-C4/Au as compared to H-azo-C3/Au suggesting a larger molecular inclination.

4.3.2 NEXAFS Spectroscopy

C and N K-edge NEXAFS spectra of the H-azo-Cn films on Au(111) are presented in Figures 4.22 and 4.23, respectively. In Figures 4.22a and 4.23a, the spectra acquired at the so-called magic angle of X-ray incidence (55°) are shown; these spectra are not affected by any effects related to molecular orientation and are, therefore, exclusively representative of the chemical composition of the investigated samples [89]. In Figures 4.22b and 4.23b, the difference between the spectra collected at X-ray incidence angles of 90° and 20° is shown for both H-azo-C3/Au and H-azo-C4/Au; such difference curves are a convenient way to monitor

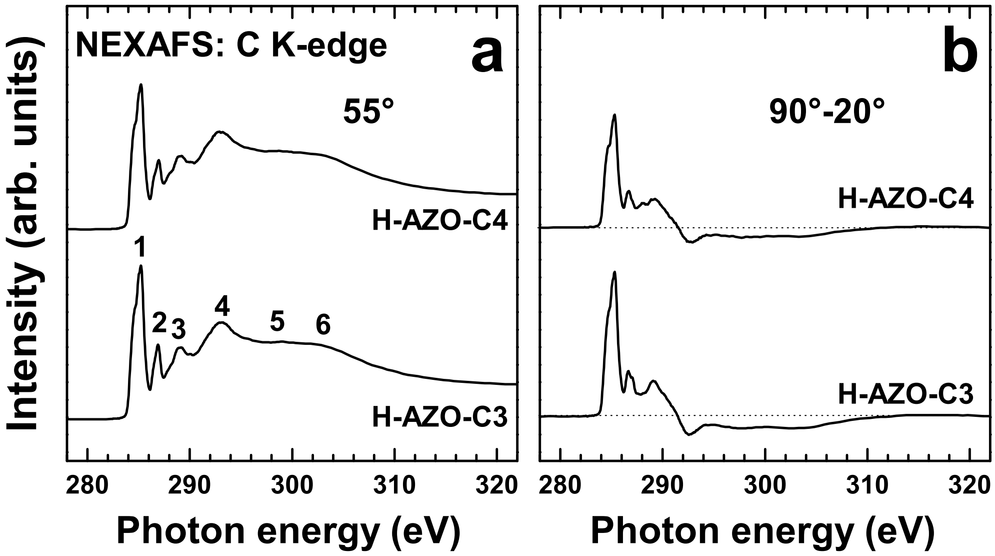

Figure 4.22: C K-edge NEXAFS spectra of H-azo-C3/Au and H-azo-C4/Au acquired at an X-ray incident angle of 55° (a), along with the respective difference between the spectra collected under the normal (90°) and grazing (20°) incidence geometry (b). Individual resonances are marked by numbers (see text for assignments). The horizontal dashed lines in (b) correspond to zero.

molecular orientation in molecular films, relying on the linear dichroism effects in X-ray absorption experiments (see Section 3) [89].

The 55° C K-edge spectra of the H-azo-Cn films in Figure 4.22a exhibit an absorption edge related to the excitation of the C 1s electrons into the continuum states and the characteristic absorption resonances. The spectra are dominated by the pronounced, asymmetric π^* resonance of the azobenzene moiety at ~285.15 eV (**1**). Such an asymmetry is typical for azobenzene [59, 156–158] and is related to a superposition of the C1s to LUMO, LUMO+1, and LUMO+2 transitions merged in the joint resonance [158, 159]. This feature is accompanied by a Rydberg resonance (R*) near 287.0 eV (**2**) [59, 156], a further π^*-like resonance of azobenzene at ~289.0 eV (**3**; C1s →LUMO+4) [158], as well as several broad σ^* resonances at higher photon energies (**4**-**6**). Note that the resonance at 287.0 eV (**2**) can be alternatively described as a π^* feature and assigned to the C1s →LUMO+3 transition [158]. Note also that the resonances associated with the aliphatic linkers are hardly perceptible in the C K-edge spectra because of the short length of this unit and the attenuation of the respective signal by the azobenzene moiety. Characteristic absorption features of the azobenzene moiety were also observed at the N K-edge. The spectra of the H-azo-Cn films in Figure 4.23a are dominated by a strong π^*

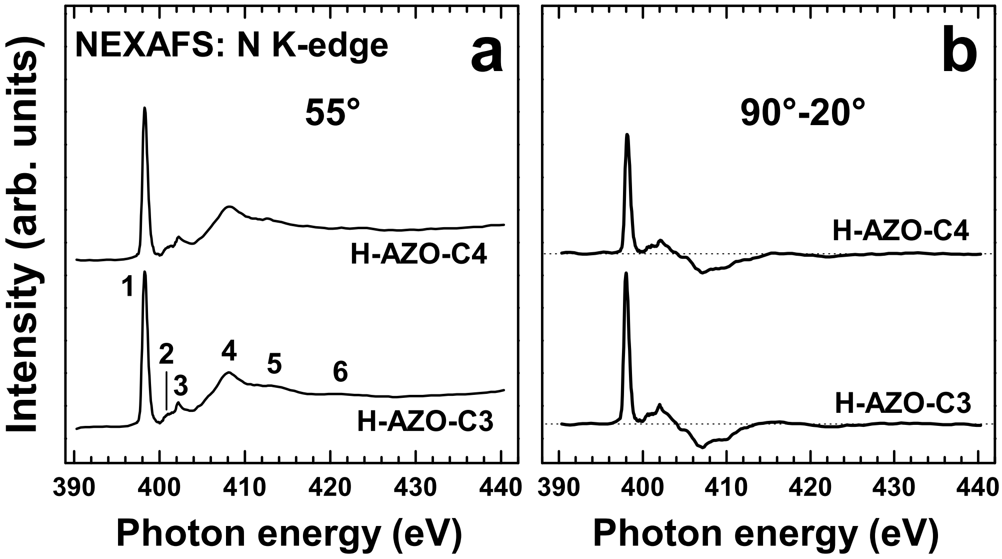

FIGURE 4.23: N K-edge NEXAFS spectra of H-azo-C3/Au and H-azo-C4/Au acquired at an X-ray incident angle of 55° (a), along with the respective difference between the spectra collected under the normal (90°) and grazing (20°) incidence geometry (b). Individual resonances are marked by numbers (see text for assignments). The horizontal dashed lines in (b) correspond to zero.

resonance at eV ∼398.3 eV (**1**) associated with the N1s →LUMO transition [158]. This feature is accompanied by several weaker π^* resonances at ∼400.9 eV (**2**) and 402.3 eV (**3**) corresponding to the N1s →LUMO+3 (**2**) and N1s →LUMO+4 (**3**) transitions [158] as well as by several broad σ^* resonances at higher photon energies (**4**-**6**). In contrast, the N1s →LUMO+2 and N1s →LUMO+3 features are not observed at the N K-edge, which suggests that the respective orbitals are located mainly at the phenyl rings and not at the azo-bridge [159]. Both C and N K-edge NEXAFS spectra of the H-azo-Cn films exhibit pronounced linear dichroism as evidenced by the characteristic peaks at the positions of the absorption resonances in Figures 4.22a and 4.23a. This is a clear signature of orientational order. In addition, the positive sign of the observed difference peaks for the π^* resonances implies an upright orientation of the molecular constituents in the monolayers in view of the fact that the π^* orbitals are directed perpendicular to the molecular backbone. Opposite situation, with a negative sign of the difference peaks, occurs for the σ^* orbitals, directed along the molecular backbone, supporting the statement about upright molecular orientation, in good agreement with the HRXPS and XPS data (see previous section). Along with the above qualitative considerations, a quantitative analysis of the entire set of the C and N-K-edge NEXAFS

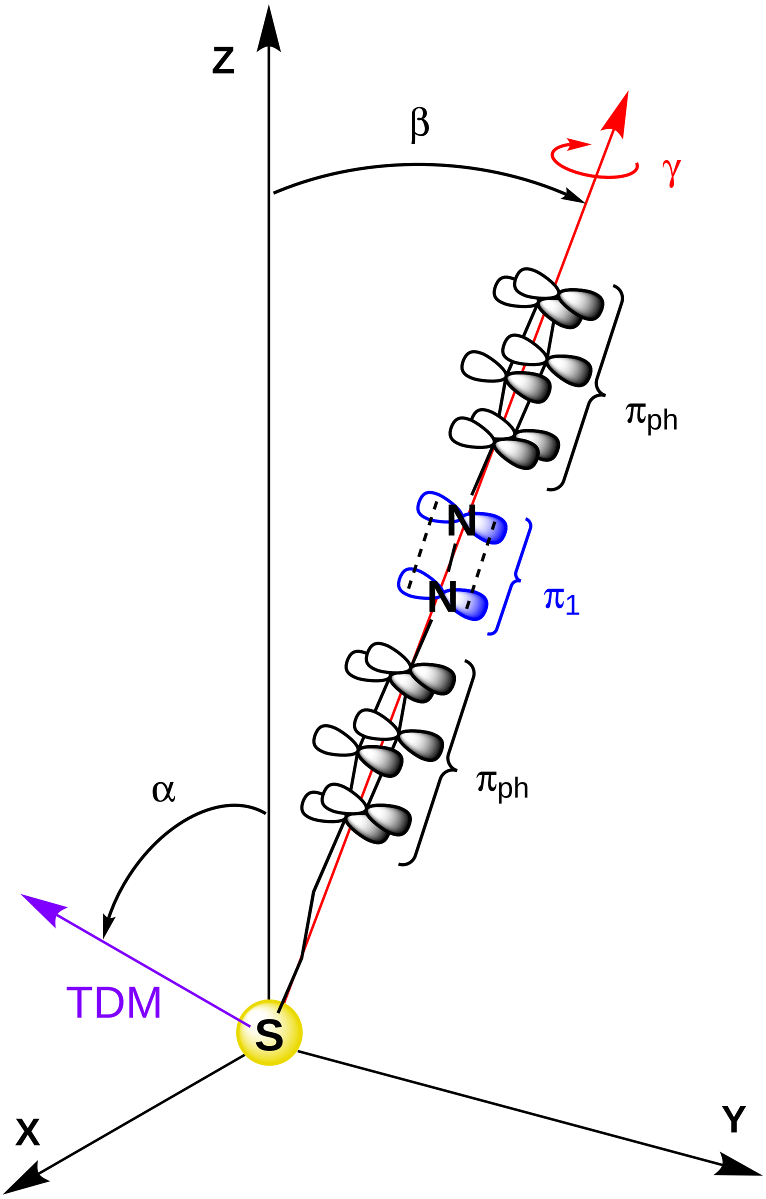

FIGURE 4.24: A schematic drawing of the orientation of the H-azo-C3 molecules in the trans conformation, representative also of H-azo-C4/Au. The phenyl rings and N=N bridge are considered to be coplanar, so that the π^* orbitals of the bridge (blue) are parallel to the π^*_{ph} orbitals of the rings (black). The backbone tilt angle β and twist angle γ describe the molecular orientation. The π^* orbitals are perpendicular to the molecular plane; the respective transition dipole moment TDM$_\pi$ is shown as a violet arrow; its orientation is given by the angle α. At γ= 0, TDM$_\pi$ lies in the plane spanned by the z-axis and the axis of the azobenzene unit (red arrow). The angles are related by the equation, $cos\alpha = sin\beta \times cos\gamma$ [69]

.

System	Molecular footprint (Å)	Effective thickness (Å)	Tilt π_1^* phenyl (°)	Tilt π^* N=N (°)	Molecular tilt (°)
H-azo-C3/Au	25.9	15.0	70.5	75.7	20.0
H-azo-C4/Au	28.6	13.0	57.0	60.0	37.0
H-azo-C3/Ag	-	12.9	63.5	64.5	31.0
H-azo-C4/Ag	-	15.5	70.5	70.5	23.0

TABLE 4.4: Overview of the parameters for H-azo-Cn/Au and H-azo-Cn/Ag. Molecular lengths of H-azo-C3 and H-azo-C4/Au are 14.6 and 15.8Å, respectively. The error of the angle values is ±3°.

spectra of the H-azo-Cn films acquired at different angles of X-ray incidence was performed. For this analysis we used the most prominent π_1^* resonances at both edges and standard theoretical framework for vector-type orbitals [89, 130]. The derived average tilt angles of the π^* orbitals representative mostly of the phenyl rings (from the C K-edge data) and exclusively of the N=N bridge (from the N K-edge data) are compiled in Table 4.4, together with some STM and XPS/HRXPS results. There are two important findings related to the angle values. First, the average tilt angle of the ring orbitals is close to that of the N=N bridge for both H-azo-C3/Au and H-azo-C4/Au assuming a close-to-planar, trans conformation for the majority of the molecules in the respective monolayers. Second, the tilt angles for the π^* orbitals of H-azo-C3/Au are noticeably larger than those for H-azo-C4/Au, suggesting a smaller molecular inclination in the former case - in full agreement with the XPS/HRXPS data. The tilt angles for the π^* orbitals can be used to calculate the average tilt angles of the molecular backbones as far as so called twist angle γ [69, 94], describing the rotation of the backbone along the molecular axis in relation to the tilt direction, is known; see Figure 4.24 where a schematic drawing of the H-azo-C3 molecule is given, representative also of H-azo-C4. The twist angle can only be measured directly or derived indirectly in selected cases [94, 118, 158, 160] but can be reasonably assumed to be close to that derived for similar azobenzene-substituted monolayers, viz. ∼32° [158]. Surprisingly, this value coincides practically with the analogous value for the bulk biphenyl (32°) [161]. The average tilt angles of the azobenzene backbones in H-azo-Cn films on Au(111) calculated within the above assumption regarding the molecular twist are compiled in Table 4.4. Accordingly, the molecular inclination in H-azo-C3/Au (∼20°) is noticeably smaller than that in H-azo-C4/Au (37°), in full agreement with the smaller molecular footprint and larger effective thickness (see Table 4.4).

4.3.3 Scanning tunneling microscopy

In addition to our spectroscopic experiments, complementary STM measurements were performed for the SAMs on Au(111) by Dominika Gnatek from the group of Dr. Piotr Cyganic from the Jagiellonian University (Krakow, Poland) [162]. The H-azo-C3 was found to adopt a 2D ordered incommensurate oblique $(2\sqrt{3} \times 1.14\sqrt{3})R30^\circ$ lattice with a packing density of ∼24.6 $Å^2$/molecule. The H-azo-C4 formed a 2D ordered incommensurate oblique $(2\sqrt{3} \times 1.3\sqrt{3})R30^\circ$ lattice with a packing density of ∼28.1 $Å^2$/molecule.

4.3.4 SAMs on Ag(111)

Analogous spectroscopic experiments were also performed for H-azo-C3/Ag and H-azo-C4/Ag. The XPS/HRXPS and NEXAFS spectra of the films on Ag were very similar to the analogous spectra for the monolayers on Au (Figures 4.21-4.23), apart from the intensity relations (XPS/HRXPS) and linear dichroism behavior (NEXAFS spectroscopy). The most important (in context of the present study) spectroscopic data for H-azo-C3/Ag and H-azo-C4/Ag are compiled in Figure 4.25. As seen in Figure 4.25a, where the C 1s HRXP spectra are presented, the intensity of the C 1s signal is noticeably higher for H-azo-C4/Ag compared to H-azo-C3/Ag. The derived effective thicknesses, compiled in Table 4.4, are 15.5 and 12.9Å, respectively. The difference between these values is too large to be explained by the presence of the additional methylene group in the alkyl linker of H-azo-C4/Ag compared to H-azo-C3/Ag. Consequently, the XPS/HRXPS data suggests a higher packing density in the former case than in the latter, which is inverse behavior compared to the films on the Au(111) substrate (see Table 4.4).

The difference NEXAFS spectra, at both C and N K-edge, in Figures 4.25a and 4.25b, respectively, exhibit a similar, inverse behavior compared to the films on the Au(111) substrate (see Figure 4.22b and 4.23b). Indeed, the amplitude of the difference peaks at the positions of the characteristic absorption resonances is higher for H-azo-C4/Ag compared to H-azo-C3/Ag, suggesting smaller molecular inclination in the former case. The derived angles of the π_1^* orbitals are compiled in Table 4.4. Similar to the Au(111) case, the C-edge and N-K-edge derived values are close to each other for the both monolayers studied, suggesting a close-to-planar, trans conformation for the majority of the SAM constituents on Ag(111) as well. At the same time, in contrast to the films on Au(111), the tilt angle of the

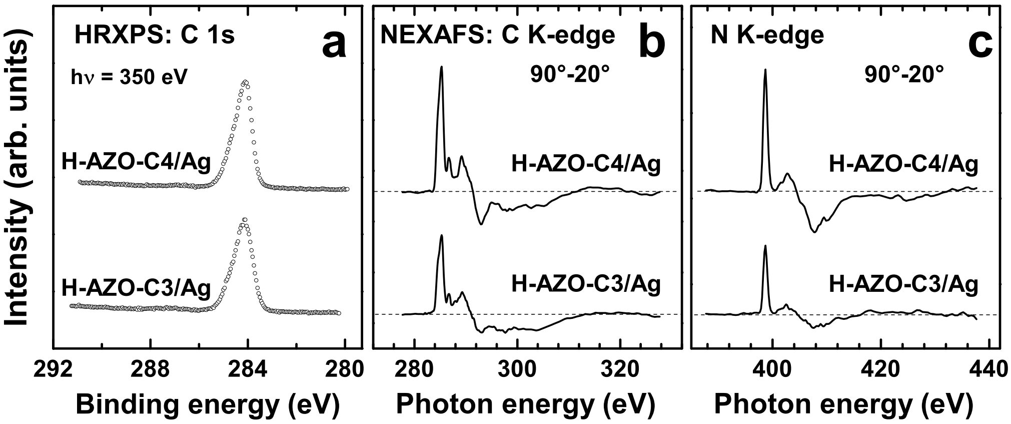

FIGURE 4.25: C 1s HRXP spectra (a) as well as the difference between the C K-edge (b) and N K-edge (c) NEXAFS spectra collected under the normal (90°) and grazing (20°) incidence geometry for H-azo-C3/Ag and H-azo-C4/Ag.

π_1^* orbitals in H-azo-C4/Ag is larger than in H-azo-C3/Ag, implying, in view of the orientation of these orbitals, a smaller molecular inclination in the former case. Accordingly, the average molecular tilt angles in H-azo-C3/Ag and H-azo-C4/Ag were estimated at 31° and 23°, respectively (see Table 4.4), exhibiting inverse behavior with respect to the parity of the aliphatic linker as compared to the films on Au(111).

4.4 Photoisomerization

4.4.1 H-azo-C3/C4

The photoisomerization experiments with the monolayers of the unsubstituted systems, H-azo-C3/C4, were performed as already described in Section 3. In the diagram shown in Figure 4.26 a change in the work function due to the conformation change caused by UV/vis irradiation is clearly visible, which means that the monolayers of the azobenzene functionalized alkanethiols show photoresponsive properties (as expected). The value of the work function change itself is about ∼30-40 meV in case of H-azo-C3 and ∼20 meV in the case of H-azo-C4. In comparison to the studies of Tamada et al.[163, 164] and Samori et al. [20], representing a benchmark in the given field (∼100meV), the work function change is somewhat lower. The reason for the low work function variation is most likely the strong steric hindrance effects due to the high packing density of the molecules on the gold substrate. Regretfully, also the variation of the packing density due to different lengths of the aliphatic linker (odd-even effect) causes almost no difference.

Apart from these results there is an interesting point to stress: the work function does not change upon first UV exposure. Theoretically, the work function of the pristine SAM should be lower due to *trans* conformation (thermodynamically more stable conformation) than the one after UV irradiation due to higher molecular dipole moment in z-direction in *cis* conformation. This implicates that the work function change is presumably mediated by *cis* conformers presented in the *trans* matrix which means that there is a certain amount of azobenzene molecules already in *cis* conformation.

4.4.2 H-azo-C3/C4 diluted with the spacer molecules

In order to reduce the strong steric hindrance effects the azobenzene molecules were diluted with the spacer molecules resulting in mixed SAMs as described in Chapter 3. In the following subsections the results for two different spacer molecules are presented (AT and PT). Theoretically the work function change/switching behaviour should generally be improved due to the created "free" space between the azobenzene molecules by dilution with the spacer molecules.

4.4.2.1 Short alkanethiols

In the case of alkanethiols we expected to obtain a significant improvement in conformation change of the azobenzene molecules. As already described in Chapter 3, octanethiol (C8) was used as a matrix. The results of the photoisomerization experiments are shown in Figure 4.27. Here, the work function changes of the samples re-immersed into H-azo-Cn (n=3,4) thiol solution for 6h and 12h, respectively, are illustrated. The values of the work function changes are almost the same (∼10-20 meV) for H-azo-C3 and H-azo-C4 respectively. Thus the odd-even effect does not affect the work function change (for the diluted H-azo-Cn SAMs as well). Compared to the pure H-azo-Cn SAMs the work function of the diluted films changes upon first UV exposure to higher values (see Figure 4.27), as theoretically expected. This implicates that the azobenzene molecules are predominantly in *trans* conformation before the first UV exposure and that the spacer molecules

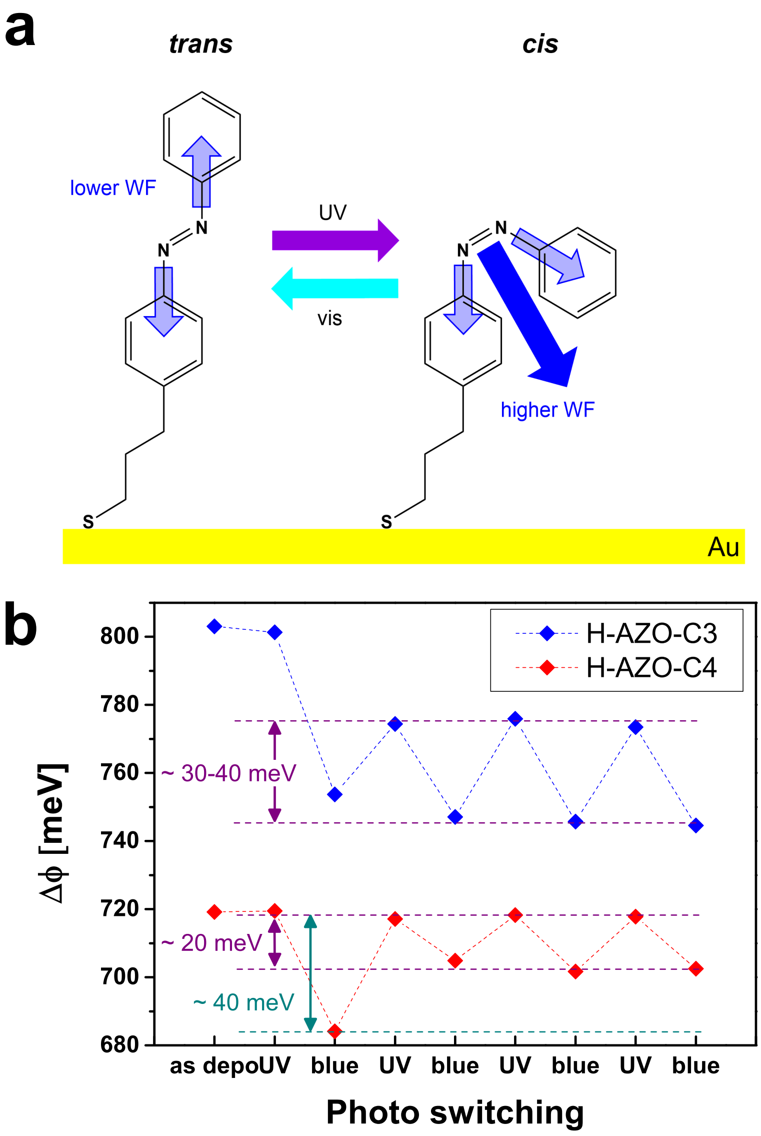

FIGURE 4.26: H-azo-Cn isomerization principle (a) and WF change from photoisomerization experiments

successfully create additional "free" space between the azobenzene molecules in order to obtain a reliable switching process.

4.4.2.2 Phenylthiol

Alternatively phenylthiol (PT) was used as the spacer molecule to obtain an improvement in switching behaviour of the azobenzene moelcules. In Figure 4.28 the results of the respective photoisomerization experiments are presented. The work function change in this case is about ~30-40 meV for H-azo-C3 and H-azo-C4 respectively. Again, like shown for alkanethiols as spacer molecule, the work

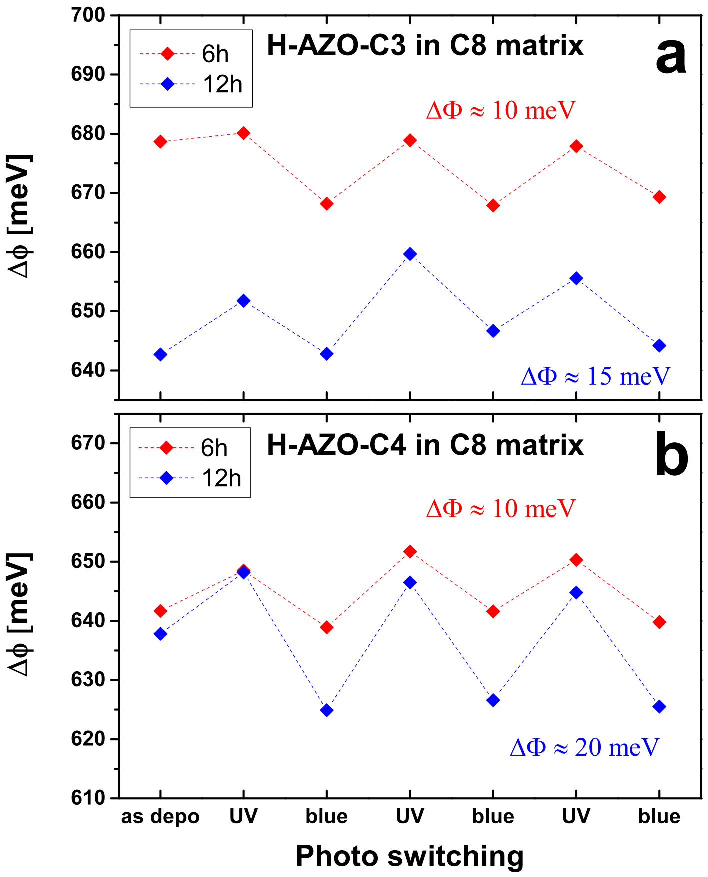

FIGURE 4.27: Azobenze alkanethiols in C8 matrix work function change

function of the pristine SAM is lower than that after first UV irradiation. This again implicates that the azobenzene molecules are predominantly in the *trans* conformation before the first UV exposure. Also an improvement in the photoswitchable properties was obtained, even more significant than using AT as the spacer molecule.

4.4.2.3 WF change vs. concentration

In order to compare the results of the photoisomerization experiments with different spacer molecules, the work function changes are plotted versus the concentration of the azobenzene molecules on the gold substrate compared to the 100% reference sample (see Figure 4.29). In both cases, H-azo-C3 and H-azo-C4, the most significant work function changes were obtained by using the phenylthiol

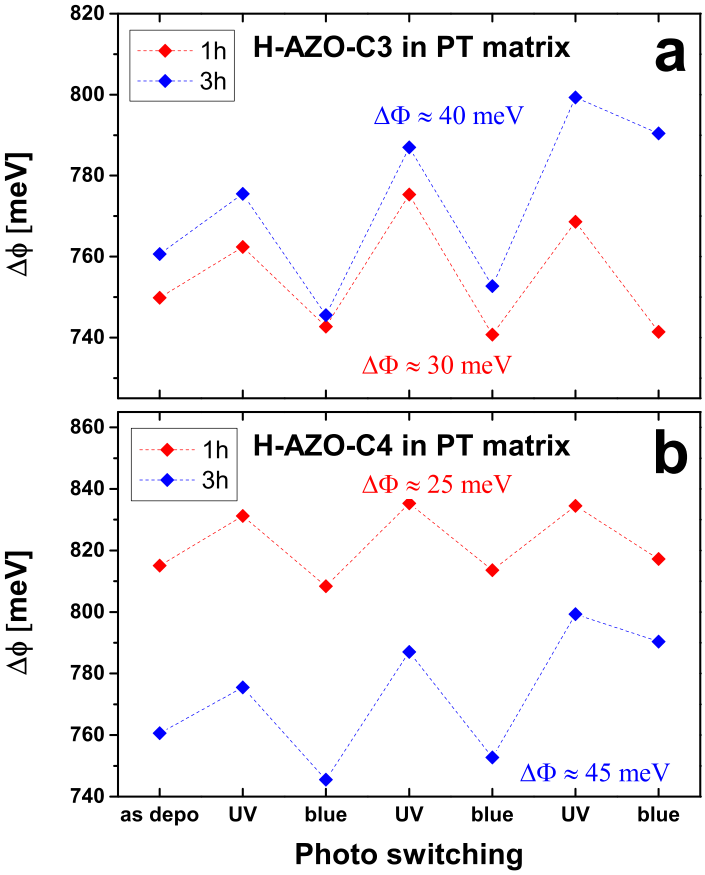

FIGURE 4.28: Azobenze alkanethiols in PT matrix work function change

(PT) matrix. The concentration of the azobenzene molecules for the most efficient WF changes of about ∼40-45 eV was ∼50-60% in the case of H-azo-C3 and ∼70-80% in the case of H-azo-C4.

4.4.3 CH_3-azo-C3/C4

In order to potentially improve the work function change, substituted systems having a higher molercular dipole moment upon the isomerization were used. The same photoisomerization experiments were performed using the analogous azobenzene molecule functionalized with the -CH_3 tail group (see Figure 4.30).

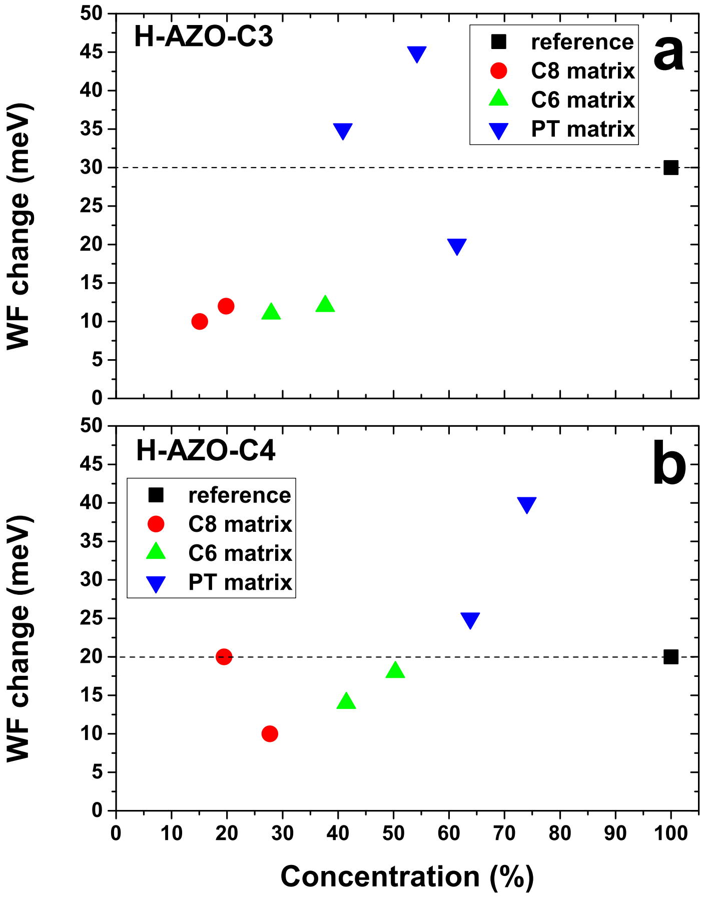

FIGURE 4.29: Work function vs. concentration of H-AZO-Cn

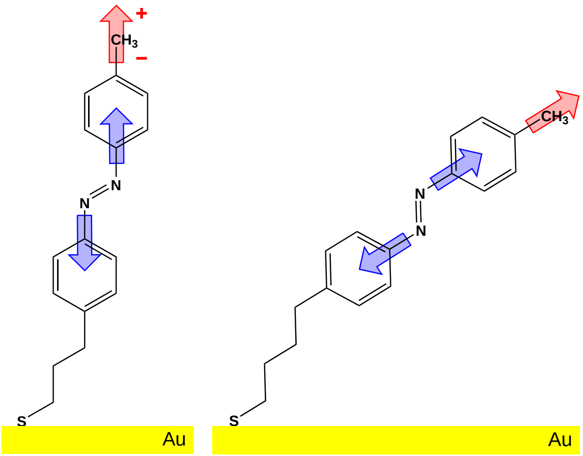

(a) CH_3-azo-C3 (b) CH_3-azo-C4

FIGURE 4.30: Azobenzene alkanethiols functionalized with -CH_3 tailgroup

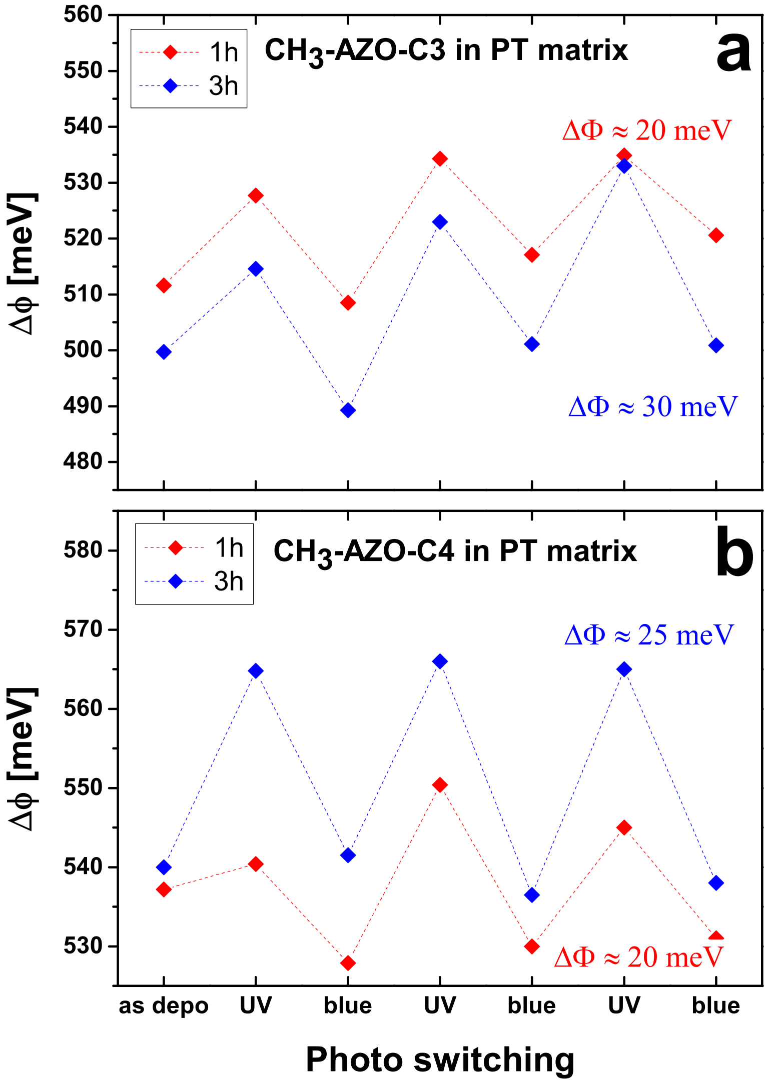

FIGURE 4.31: CH_3-azo-Cn in PT matrix

4.4.4 CH_3-azo-C3/C4 diluted with spacer molecules

The mixed SAMs were prepared in the same way like those with the unsubstituted azobenzene molecules. The results of the respective photoisomerization experiments using the phenylthiol matrix are shown in Figure 4.31. The value of the work function change for both CH_3-azo-C3 and CH_3-azo-C4 is approximately ∼20-30 meV, which is no significant improvement compared to the unsubstituted systems.

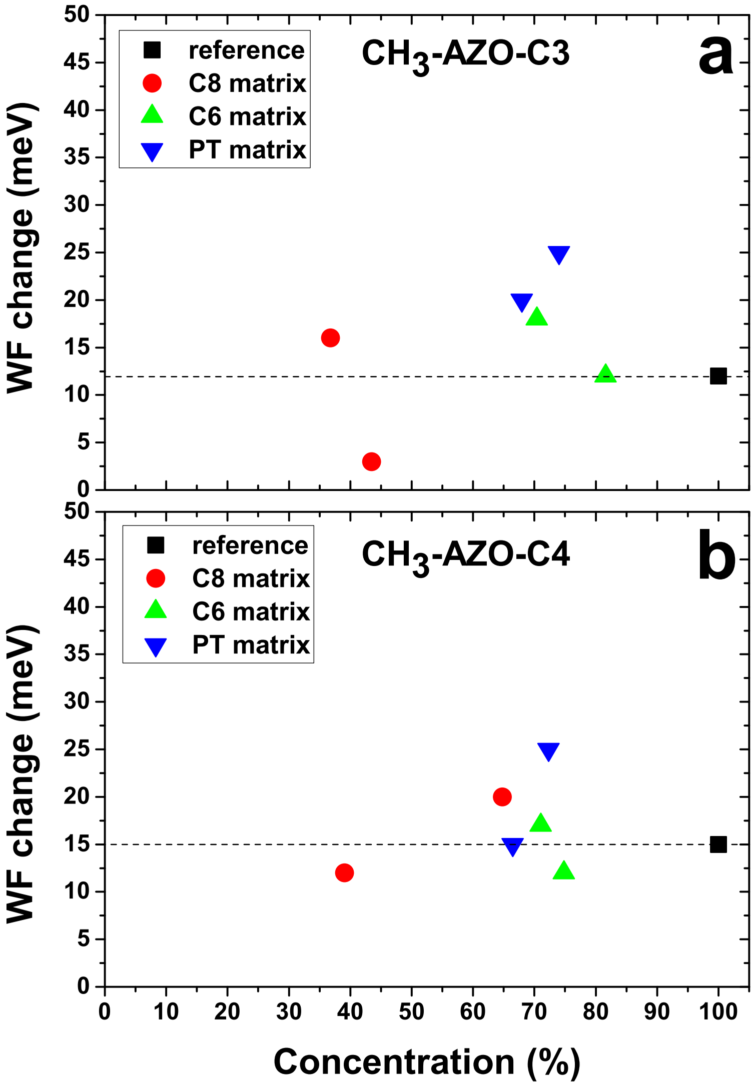

Figure 4.32: Work function vs. concentration of CH_3-azo-Cn

4.4.4.1 WF change vs. concentration

To compare the results of the performed experiments with the CH_3-azo-C3/C4 films we plotted the WF change versus the concentration of the azobenzene molecules in the mixed monolayers, like we did for the unsubstituted systems (see Figure 4.32).

Compared to the WF change of the 100% reference sample, again, the phenylthiol matrix looks more suitable compared to the alkanethiol one, similar to the case of the unsubstituted systems.

4.4.5 Discussion

In general the photoisomerization experiments show promising results. In comparison to a study from the group of Samori et al. [51] our obtained work function changes of about ∼10-50 meV is not that far away from their work function change of ∼70-125 meV. In their study, they used biphenyl AZO SAMs of highly ordered and tightly packed structure with ab isomerization yield of almost 100% [50]. Due to the fact that we have no information of the isomerization yield of our systems, it is possible to achieve a higher work function change than this benchmark value (∼70-125 meV).

Chapter 5

Conclusions

The goal of this work was to look for new ways to control the work function of metal substrates by using molecular self-assembly. Two different strategies were carried out. The first strategy was to use aliphatic and aromatic molecules which contain an embedded dipolar group (mid-chain functionalization). Within the second strategy, we used photoresponsive systems, viz. azobenzene substituted alkanethiols, having a specially designed architecture to control the packing density and carrying an additional dipolar tail group.

For the molecules with an embedded dipolar element, the dipole control and the chemistry at the SAM-ambient interface are decoupled. As the first relevant system, we studied a series of aliphatic SAMs on Au(111) prepared from mid-chain ester functionalized thiols, HS-$(CH_2)_mCO_2(CH_2)_{n-1}CH_3$ (C$m$EC$n$) with different combinations of m and n as well as with different dipolar group orientations. The electronic properties of these systems were analyzied by high resolution X-ray photoelectron spectroscopy (HRXPS), near edge X-ray absorption fine structure (NEXAFS) spectroscopy, work function measurements and theoretical simulations with supporting characterization by infrared spectroscopy and atomic force microscopy (AFM). From a fundamental point of view, the most interesting observation was a strong electrostatic effect in the X-ray photoelectron spectra. In the presence of embedded esters, the C 1s photoelectron kinetic energies were found to be consistently shifted by 0.85 eV between the chemically identical -(CH_2)- alkyl segments above and below the ester moiety, regardless of the relative lengths of the segments. This shift correlates well with simple electrostatic estimates based on dipole moment of the ester groups at their orientation in the SAMs. Significantly, this observation, along with few others [31–34], contradicts the generally accepted assumption that the photoemission spectra of SAMs can be described entirely within the general concept of a chemical shift [35].

As the second relevant system within the embedded dipole strategy, we studied a set of aromatic, terphenyl based SAMs, carrying an embedded pyrimidine dipolar group, with the orientation of the dipole being varied. Using a variety of complementary experimental characterization techniques, supported by DFT calculations, we investigated in detail a model system of self-assembled monolayers on gold comprising aromatic thiolates with embedded dipoles. The dipoles were introduced into the SAM precursor molecules, TP1 (terphenyl-4-methanethiol), by substituting the central phenyl ring by a 2,5-pyrimidine moiety. Altering the orientation of the pyrimidine moiety allows the realization of monolayers in which the dipole moments either point away from (TP1-up/Au) or towards the substrate (TP1-down/Au). The results of the spectroscopic and microscopic techniques imply that the molecular orientation and the structure of the substituted films closely resemble those of the non-polar benchmark system, TP1/Au. Characterization of the electronic properties of these reveals that the embedded dipoles significantly shift the substrate work function in a systematic manner: a dipole moment pointing towards the Au substrate increases the WF, while a dipole moment pointing away decreases the WF compared to the TP1/Au benchmark system. The accessible WF range spans ~1 V, while, at the same time, maintaining the chemical identity and structural properties of the SAM-ambient interface. This implies that the strategy of embedded dipoles in interfacial, monomolecular layers indeed opens up the possibility to decouple control over charge-injection from control over the nucleation and growth of organic semiconductor layers. Thus, such films have high potential in organic electronics, where they can be used for the interface engineering. Also in molecular electronics they allow the study of electrostatic effects independently from the (top) contact properties. Specific electrostatic properties of such systems go beyond work function control, leading, in particular, to interesting effects in photoemission, calling into question the commonly applied concept that chemical shifts are the only cause for certain values of the core-level binding energies. Finally, the observation that dipole-induced electrostatic shifts within monolayers can be realized and efficiently characterized experimentally raises the question, whether also considerably more complex, electrostatically designed structures will become available as "real-world" systems already in the near future. Such structures can comprise, for example, monolayer quantum-wells and quantum-cascades realized by a deliberate combination of dipolar and semiconducting elements within one molecule, as suggested recently on the basis of quantum-mechanical simulations [165].

In order to control the work function in a more precise way, mixed films consisting of molecules carrying embedded dipoles with the opposite orientations were used. These films provide a fine tuning of the work function between the ultimate values, associated with a particular dipole orientation.

Further within the second strategy to tune the work function on metals, we created stimuli-responsive interfaces by designing novel azobenzene-based monolayers carrying dipolar groups. We started with the characterization of the unsubstituted films as a basic system. We have performed detail structural analysis of prototypical SAMs containing azobenzene moiety linked to the thiol head group via aliphatic spacer in the form C_6H_4-N-N-C_6H_4-$(CH_2)_n$-SH at n = 3 and 4). Our data show that depending on either odd or even number of the methylene units in this spacer, two different structures can be formed. For the Au(111) substrate, higher surface packing density and lower inclination of the azobenzene moiety towards surface normal is achieved for the odd-numbered system. In case of the Ag(111) substrate, this relation is reversed and higher packing density and lower inclination of the molecular axis is achieved for the even-numbered system. This structural odd-even effect is fully correlated with the odd-even effect in the stability of the film probed by the exchange and ion desorption experiments. Higher stability of the odd-numbered film on the Au(111) substrate and even-numbered film on the Ag(111) substrate is a consequence of higher stability of the molecule-substrate bonding, higher surface coverage, and most probably, lower surface stress value. The odd-even effect in the film stability is much less pronounced for the Ag(111) substrate as compared to the Au(111) substrate what could be explained by lower corrugation of the S-Ag(111) binding energy hypersurface as compared to the S-Au(111). The odd-even structure and stability modification of azobenzene terminated SAMs may have potential importance for their applications in molecular electronics and interfacial engineering. Light-induced work function variations of about 20-40 meV were obtained, limited, presumably, by strong seric hindrance effects. By dilution of the azobenzene molecules with short spacer molecules, the photoswitchable properties could be improved to some extent.

In addition, experiments with substituted systems were performed, in order to improve the photoswitchable response due to the additional dipolar tail group (i.e.-CH_3). The irradiation-induced work function variation was found to be approximately 20-30 meV after the dilution with spacer molecules.

The obtained results regarding the photoisomerization are quite promising and show a certain potential to further improvements, further experiments will be performed using different dipolar tail groups and specially designed spacer molecules in order to improve the photoswitchable properties.

Appendix A

Additional Data

A.1 Reference HRXPS data for 2-MPM

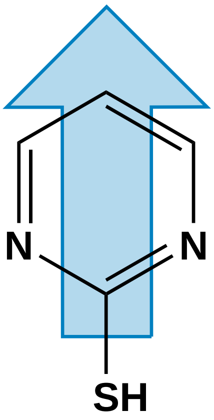

2-MPM

Figure A.1: A schematic drawing of the reference molecule along with its acronym. The directions of the dipole moment associated with the embedded pyrimidine group are shown. The molecules are named accordingly.

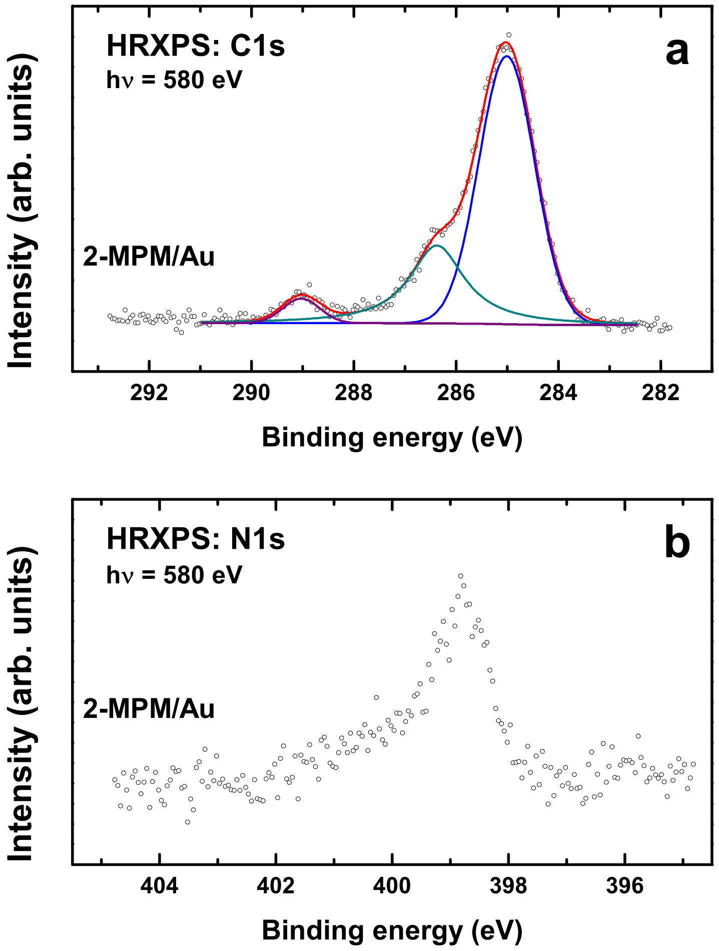

FIGURE A.2: C 1s (a) and N 1s (b) HRXP spectra of the 2-MPM SAM acquired at a photon energy of 580 eV. The C 1s spectrum is tentatively decomposed in several individual components. The emission at 289 eV is presumably related to contamination (COO-).[Cebula2013]

Appendix B

Experimental Setups

B.1 Kelvin Probe

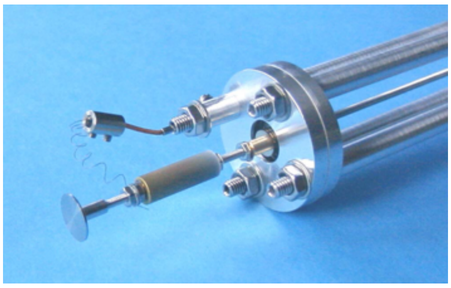

Figure B.1: Picture of the UHV Kelvin Probe

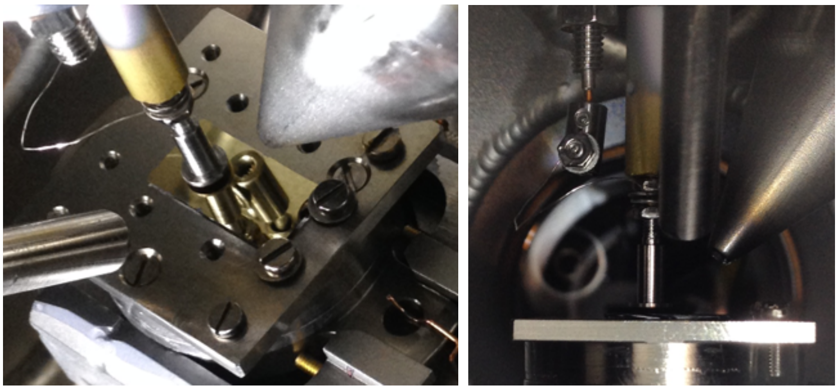

(a) top view

(b) side view

Figure B.2: Pictures of the UHV Kelvin Probe setup from top view (a) and from side view (b).

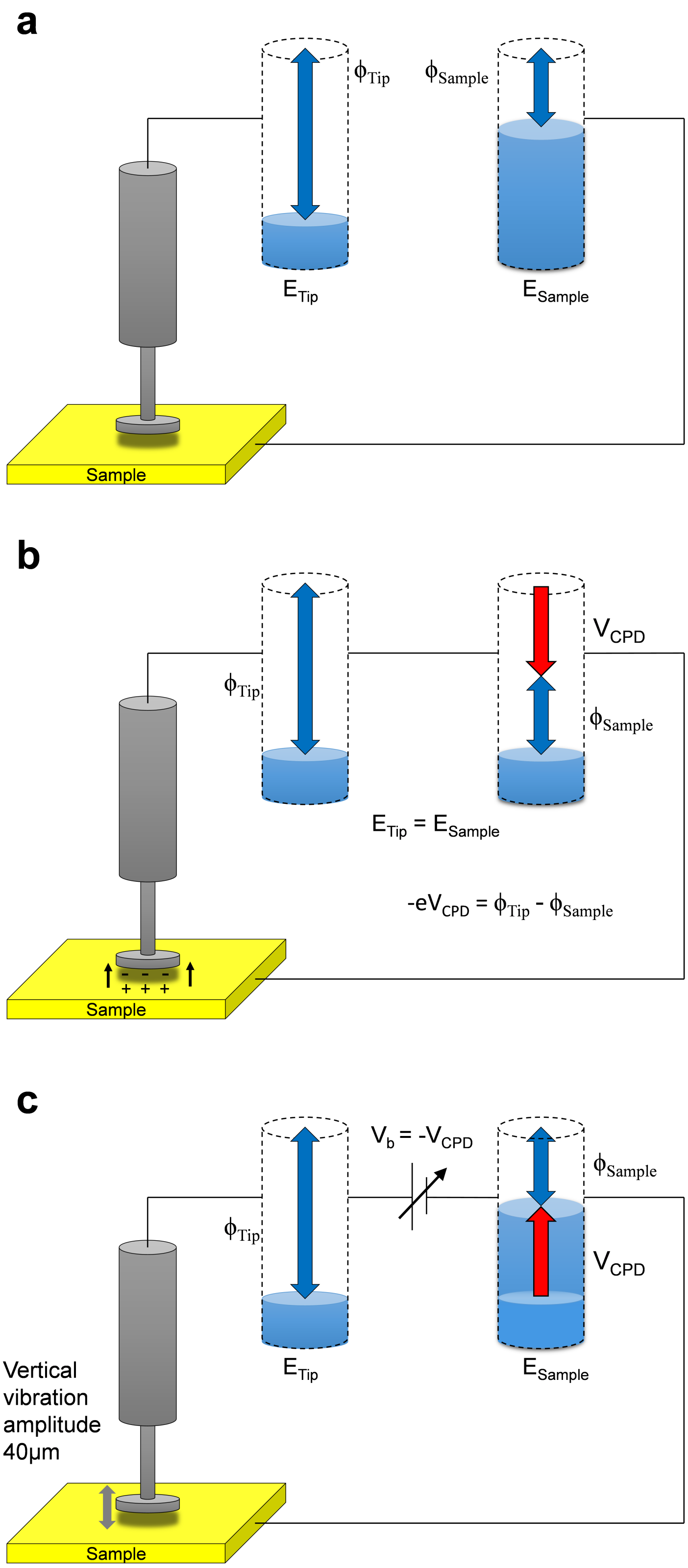
a
ϕ_{Tip}
ϕ_{Sample}
E_{Tip}
E_{Sample}
Sample
b
V_{CPD}
ϕ_{Tip}
ϕ_{Sample}
$E_{Tip} = E_{Sample}$
$-eV_{CPD} = \phi_{Tip} - \phi_{Sample}$
- - -
+ + +
Sample
c
$V_b = -V_{CPD}$
ϕ_{Sample}
ϕ_{Tip}
V_{CPD}
E_{Tip}
E_{Sample}
Vertical
vibration
amplitude
40µm
Sample

FIGURE B.3: Schematic drawing of the basic principles of the Kelvin Probe work function measurements.

B.2 LED irradiation setup

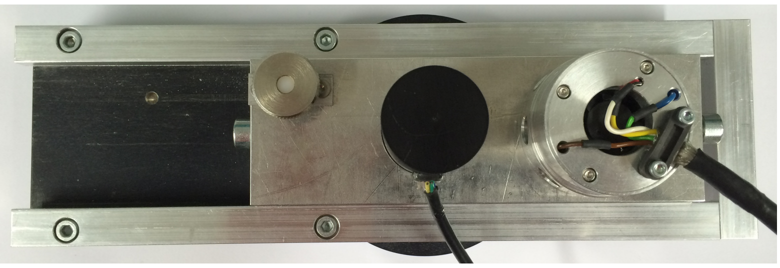

Figure B.4: Picture of the LED setup which provides switching between two LED lamps (without any daylight irradiation during the change of the LED lamp). It is designed to be mounted on a UV window of a UHV chamber for UV/vis irradiation experiments.

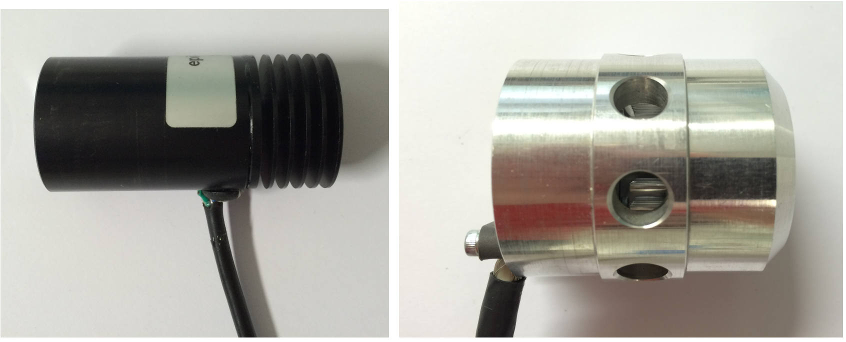

(a) UV LED

(b) blue LED

Figure B.5: Pictures of the UV LED (365 nm) (a) and the blue LED (440 nm) (b).

Appendix C

Lists

C.1 List of Publications

1. Musumeci, C.; Zappala, G.; Martsinovich, N.; Orgiu, E.; Schuster, S.; Quici, S.; Zharnikov, M.; Troisi, A.; Licciardello, A.; Samori, P., Nanoscale electrical investigation of layer-by-layer grown molecular wires. *Adv. Mater.* **2014**, *26* (11), 1688-1693.

2. Khan, M.; Schuster, S.; Zharnikov, M., Effect of Humidity on Electrical Conductivity of Pristine and Nanoparticle-Loaded Hydrogel Nanomembranes. *J. Phys. Chem. C* **2015**, *119*, 14427-14433.

3. Abu-Husein, T.; Schuster, S.; Egger, D. A.; Kind, M.; Santowski, T.; Wiesner, A.; Chiechi, R.; Zojer, E.; Terfort, A.; Zharnikov, M., The Effects of Embedded Dipoles in Aromatic Self-Assembled Monolayers. *Adv. Funct. Mater.* **2015**, *25* (25), 3943-3957.

4. Gnatek, D.; Schuster, S.; Ossowski, J.; Khan, M.; Rysz, J.; Terfort, A.; Zharnikov, M.; Cyganik, P., Odd-even Effects in the Structure and Stability of Azobenzene-Substituted Alkanethiolates on Au(111) and Ag(111) Substrates. *submitted*

5. Cabarcos, O.; Schuster, S.; Hehn, I.; Sullivan, N.; Zhang, P. P.; Maitani, M.; Morin, J.-F.; Weiss, P. S.; Zojer, E.; Zharnikov, M.; Allara, D. L., Effects of Embedded Electric Dipole Layers in Alkanethiolate Self-Assembled Monolayers. *in preparation*

C.2 List of conference contributions

1. Schuster, S.; Khan, M.; Cyganik, P.; Terfort, A.; Zharnikov, M., *Functional Azobenzene based Self-Assembled Monolayers: molecular composition effects and photo switchable properties*, DPG Spring Meeting, April 2014, Dresden, Germany.

2. Hehn, I.; Vieider, M.; Roscioni, O. M.; Muccioli, L.; Egger, D.; Schuster, S.; Zharnikov, M.; Zannoni, C.; Zojer, E., *Simulating the electronic and structural properties of self-assembled monolayers with embedded dipoles*, May 25-30, 2014, EMRS, Lille, France.

3. Schuster, S.; Sullivan, N.; Cabarcos, O.; Hehn, I.; Morin, J.-F.; Zojer, E.; Zharnikov, M.; Allara, D. L., *Embedded dipole in alkanethiolate self-assembled monolayers: Electronic structure and work function effects*, AVS 61st International Symposium & Exhibition, November 2014, Baltimore, MD, USA.

4. Ossowski, J.; Noworolska, A.; Schuster, S.; Rysz, J., Terfort, A.; Zharnikov, M., Cyganik, P., *Relative stability of S-Au and Se-Au bonding in aromatic and aliphatic self-assembled monolayers - exchange and ion desorption experiments*, AVS 61st International Symposium & Exhibition, November 2014, Baltimore, MD, USA.

5. Schuster, S., Khan, M., Cyganik, P., Terfort, A., Zharnikov, M., *Azobenzene based self-assembled monolayers as a means to control the work function*, DPG Spring Meeting, March 2015, Berlin, Germany.

6. Schuster, S.; Sullivan, N.; Cabarcos, O.; Hehn, I.; Morin, J.-F.; Zojer, E.; Allara, D. L., Zharnikov, M., *Effects of embedded dipole in alkanethiolate self-assembled monolayers*, DPG Spring Meeting, March 2015, Berlin, Germany.

7. Hehn, I.; Vieider, M.; Roscioni, O. M.; Muccioli, L.; Egger, D. A.; Schuster, S.; Zharnikov, M.; Zannoni, C.; Zojer, E., *Including depolarization effects in molecular dynamics simulations of self-assembled monolayers*, DPG Spring Meeting, March 2015, Berlin, Germany.

8. Hehn, I.; Roscioni, O. M.; Muccioli, L.; Egger, D. A.; Schuster, S.; Zharnikov, M.; Zannoni, C.; Zojer, E., *Effect of depolarization in the packing of self-assembled*

monolayers, 7th Summer School on Organic Electronics, September 2015, Como, Italy.

9. Schuster, S.; Abu-Husein, T.; Egger, D. A.; Hehn, I., Kind, M.; Zojer, E.; Terfort, A.; Zharnikov, M., *The Effects of Embedded Dipoles in Aromatic Self-Assembled Monolayers*, AVS 62nd International Symposium & Exhibition, October 2015, San Jose, CA, USA (accepted)

Bibliography

[1] A. Ulman. *An Introduction to Ultrathin Organic Films. From Langmuir-Blodgett to Self-Assembly*, volume 8. Academic Press: New York, New York, 1991.

[2] C. L. Love, L. A. Estroff, J. K. Kriebel, R. G. Nuzzo, and G. M. Whitesides. Self-assembled monolayers of thiolates on metals as a form of nanotechnology. *Chem. Rev.*, 105:1103–1169, 2005.

[3] R. G. Nuzzo and D. A. Allara. Adsorption of bifunctional organic disulfides on gold surfaces. *J. Am. Chem. Soc.*, 105(13):4481–4483, 1983.

[4] X. J. Feng and L. Jiang. Design and creation of superwetting/antiwetting surfaces. *Adv. Mater.*, 18(23):3063–3078, 2006.

[5] S. L. Gras, T. Mahmud, G. Rosengarten, A. Mitchell, and K. Kalantar-Zadeh. Intelligent control of surface hydrophobicity. *Chem. Phys. Chem.*, 8 (14):2036–2050, 2007.

[6] P. M. Mendes. Stimuli-responsive surfaces for bio-applications. *Chem. Soc. Rev.*, 37(11):2512–2529, 2008.

[7] A. Rosenhahn, S. Schilp, H. J. Kreuzer, and M. Grunze. The role of inert surface chemistry in marine biofouling prevention. *Phys. Chem. Chem. Phys.*, 12(17):4275–4286, 2010.

[8] L. Srisombat, A. C. Jamison, and T. R. Lee. Stability: A key issue for self-assembled monolayers on gold as thin-film coatings and nanoparticle protectants. *Colloids and Surfaces A*, 390(1-3):1–19, 2011.

[9] J. Landoulsi, K. E. Cooksey, and V. Dupres. Review - interactions between diatoms and stainless steel: focus on biofouling and biocorrosion. *Biofouling*, 27(10):1105–1124, 2011.

[10] M. Halik, H. Klauk, U. Zschieschang, G. Schmid, C. Dehm, M. Schutz, S. Maisch, F. Effenberger, M. Brunnbauer, and F. Stellacci. Low-voltage organic transistors with an amorphous molecular gate dielectric. *Nature*, 431(7011):963–966, 2004.

[11] H. Klauk, U. Zschieschang, J. Pflaum, and M. Halik. Ultralow-power organic complementary circuits. *Nature*, 445(7129):745–748, 2007.

[12] M. Salinas, C. M. Jager, A. Y. Amin, P. O. Dral, T. Meyer-Friedrichsen, A. Hirsch, T. Clark, and M. Halik. The relationship between threshold voltage and dipolar character of self-assembled monolayers in organic thin-film transistors. *J. Am. Chem. Soc.*, 134(30):12648–52, 2012.

[13] M. Burkhardt, A. Jedaa, M. Novak, A. Ebel, K. Voitchovsky, F. Stellacci, A. Hirsch, and M. Halik. Concept of a molecular charge storage dielectric layer for organic thin-film memory transistors. *Adv. Mater.*, 22(23):2525–2528, 2010.

[14] P. Pacher, A. Lex, V. Proschek, H. Etschmaier, E. Tchernychova, M. Sezen, U. Scherf, W. Grogger, G. Trimmel, C. Slugovc, and E. Zojer. Chemical control of local doping in organic thin-film transistors: From depletion to enhancement. *Adv. Mater.*, 20(16):3143–3148, 2008.

[15] E. C. P. Smits, S. G. J. Mathijssen, P. A. van Hal, S. Setayesh, T. C. T. Geuns, K. A. H. A. Mutsaers, E. Cantatore, H. J. Wondergem, O. Werzer, R. Resel, M. Kemerink, S. Kirchmeyer, A. M. Muzafarov, S. A. Ponomarenko, B. de Boer, P. W. M. Blom, and D. M. de Leeuw. Bottom-up organic integrated circuits. *Nature*, 455(7215):956–959, 2008.

[16] I. H. Campbell, S. Rubin, T. A. Zawodzinski, J. D. Kress, R. L. Martin, D. L. Smith, N. N. Barashkov, and J. P. Ferraris. Controlling schottky energy barriers in organic electronic devices using self-assembled monolayers. *Phys. Rev. B*, 54(20):14321–14324, 1996.

[17] I. H. Campbell, J. D. Kress, R. L. Martin, D. L. Smith, N. N. Barashkov, and J. P. Ferraris. Controlling charge injection in organic electronic devices using self-assembled monolayers. *Appl. Phys. Lett.*, 71(24):3528–3530, 1997.

[18] B. de Boer, A. Hadipour, M. M. Mandoc, T. van Woudenbergh, and P. W. M. Blom. Tuning of metal work functions with self-assembled monolayers. *Adv. Mater.*, 17(5):621–625, 2005.

[19] C. Bock, D. V. Pham, U. Kunze, D. Käfer, G. Witte, and C. Wöll. Improved morphology and charge carrier injection in pentacene field-effect transistors with thiol-treated electrodes. *J. Appl. Phys.*, 100(11):114517, 2006.

[20] N. Crivillers, S. Osella, C. Van Dyck, G. M. Lazzerini, D. Cornil, A. Liscio, F. Di Stasio, S. Mian, O. Fenwick, F. Reinders, M. Neuburger, E. Treossi, M. Mayor, V. Palermo, F. Cacialli, J. Cornil, and P. Samori. Large work function shift of gold induced by a novel perfluorinated azobenzene-based self-assembled monolayer. *Adv. Mater.*, 25(3):432–436, 2013.

[21] I. Lange, S. Reiter, M. Pätzel, A. Zykov, A. Nefedov, J. Hildebrandt, S. Hecht, S. Kowarik, C. Wöll, G. Heimel, and D. Neher. Tuning the work function of polar zinc oxide surfaces using modified phosphonic acid self-assembled monolayers. *Adv. Funct. Mater.*, 24(44):7014–7024, 2014.

[22] J. Kim, Y. S. Rim, Y. S. Liu, A. C. Serino, J. C. Thomas, H. J. Chen, Y. Yang, and P. S. Weiss. Interface control in organic electronics using mixed monolayers of carboranethiol isomers. *Nano Letters*, 14(5):2946–2951, 2014.

[23] E. Margapoti, J. Li, O. Ceylan, M. Seifert, F. Nisic, T. L. Anh, F. Meggendorfer, C. Dragonetti, C. A. Palma, J. V. Barth, and J. J. Finley. A 2d semiconductor-self-assembled monolayer photoswitchable diode. *Adv. Mater.*, 27(8):1426–1431, 2015.

[24] B. H. Hamadani, D. A. Corley, J. W. Ciszek, J. M. Tour, and D. Natelson. Controlling charge injection in organic field-effect transistors using self-assembled monolayers. *Nano Lett.*, 6(6):1303–1306, 2006.

[25] G. Heimel, L. Romaner, J. L. Bredas, and E. Zojer. Interface energetics and level alignment at covalent metal-molecule junctions: pi-conjugated thiols on gold. *Phys. Rev. Lett.*, 96(19):196806, 2006.

[26] K. Heister, S. Frey, A. Ulman, M. Grunze, and M. Zharnikov. Irradiation sensitivity of self-assembled monolayers with an introduced ”weak link”. *Langmuir*, 20(4):1222–1227, 2004.

[27] Jr. Petoral, R. M. and K. Uvdal. Structure of tert-butyl carbamate-terminated thiol chemisorbed to gold. *J. Phys. Chem. B*, 109(33):16040–16046, 2005.

[28] S. Krakert, N. Ballav, M. Zharnikov, and A. Terfort. Adjustment of the bioresistivity by electron irradiation: self-assembled monolayers of oligo(ethyleneglycol)-terminated alkanethiols with embedded cleavable group. *Phys. Chem. Chem. Phys.*, 12(2):507–515, 2010.

[29] P. A. Lewis, C. E. Inman, F. Maya, J. M. Tour, J. E. Hutchison, and P. S. Weiss. Molecular engineering of the polarity and interactions of molecular electronic switches. *J. Am. Chem. Soc.*, 127(49):17421–17426, 2005.

[30] O. M. Cabarcos, A. Shaporenko, T. Weidner, S. Uppili, L. S. Dake, M. Zharnikov, and D. L. Allara. Physical and electronic structure effects of embedded dipoles in self-assembled monolayers: Characterization of mid-chain ester functionalized alkanethiols on au111. *J. Phys. Chem. C*, 112(29): 10842–10854, 2008.

[31] H. Ahn, M. Zharnikov, and J. E. Whitten. Abnormal pinning of the fermi and vacuum levels in monomolecular self-assembled films. *Chemical Physics Letters*, 428(4-6):283–287, 2006. ISSN 0009-2614.

[32] Y. Ge, T. Weidner, H. Ahn, J. E. Whitten, and M. Zharnikov. Energy level pinning in self-assembled alkanethiol monolayers. *J. Phys. Chem. C*, 113 (11):4575–4583, 2009.

[33] N. Ballav, A. Terfort, and M. Zharnikov. Mixing of nonsubstituted and partly fluorinated alkanethiols in a binary self-assembled monolayer. *J. Phys. Chem. C*, 113(9):3697–3706, 2009.

[34] N. V. Venkataraman, S. Zürcher, A. Rossi, S. Lee, N. Naujoks, and N. D. Spencer. Spatial tuning of the metal work function by means of alkanethiol and fluorinated alkanethiol gradients. *J. Phys. Chem. C*, 113(14):5620–5628, 2009.

[35] B. D. Ratner and D. G. Castner. *Surface Analysis - The Principle Techniques*, book section Electron Spectroscopy for Chemical Analysis. Wiley & Sons Chichester, 1997.

[36] D. A. Egger, F. Rissner, G. M. Rangger, O. T. Hofmann, L. Wittwer, G. Heimel, and E. Zojer. Self-assembled monolayers of polar molecules on au(111) surfaces: distributing the dipoles. *Phys. Chem. Chem. Phys.*, 12 (17):4291–4294, 2010.

[37] N. J. Tao. Electron transport in molecular junctions. *Nature Nanotechn.*, 1 (3):173–181, 2006.

[38] S. Karthäuser. Control of molecule-based transport for future molecular devices. *J. Phys. Condens. Matter*, 23(1):013001, 2011.

[39] C. Querebillo, A. Terfort, D. A. Allara, and M. Zharnikov. Static conductance of nitrile-substituted oligophenylene and oligo(phenylene ethynylene) self-assembled monolayers studied by mercury-drop method. *J. Phys. Chem. C*, 117(48):25556–25561, 2013.

[40] C. Bock, D. V. Pham, U. Kunze, D. Käfer, G. Witte, and A. Terfort. Influence of anthracene-2-thiol treatment on the device parameters of pentacene bottom-contact transistors. *Appl. Phys. Lett.*, 91(5):052110, 2007.

[41] T. Ishida, W. Mizutani, U. Akiba, K. Umemura, A. Inoue, N. Choi, M. Fujihira, and H. Tokumoto. Lateral electrical conduction in organic monolayer. *J. Phys. Chem. B*, 103(10):1686–1690, 1999.

[42] T. Ishida, W. Mizutani, N. Choi, U. Akiba, M. Fujihira, and H. Tokumoto. Structural effects on electrical conduction of conjugated molecules studied by scanning tunneling microscopy. *J. Phys. Chem. B*, 104(49):11680–11688, 2000.

[43] C. Fuxen, W. Azzam, R. Arnold, G. Witte, A. Terfort, and C. Wöll. Structural characterization of organothiolate adlayers on gold: The case of rigid, aromatic backbones. *Langmuir*, 17(12):3689–3695, 2001.

[44] A. Shaporenko, M. Brunnbauer, A. Terfort, M. Grunze, and M. Zharnikov. Structural forces in self-assembled monolayers: Terphenyl-substituted alkanethiols on noble metal substrates. *Journal of Physical Chemistry B*, 108 (38):14462–14469, 2004.

[45] W. Azzam, A. Bashir, A. Terfort, T. Strunskus, and C. Wöll. Combined stm and ftir characterization of terphenylalkanethiol monolayers on au(111): effect of alkyl chain length and deposition temperature. *Langmuir*, 22(8): 3647–55, 2006.

[46] H. Weiler-Feilchenfeld and E. D. Bergmann. The dipole moments of some purine and pyrimidine derivatives. *Israel J. Chem.*, 6(5):823–826, 1968.

[47] G. L. Blackman, R. D. Brown, and F. R. Burden. The microwave spectrum, dipole moment, and nuclear quadrupole coupling constants of pyrimidine. *J. Mol. Spectrosc.*, 36(3):444–454, 1970.

[48] E. Orgiu and P. Samori. 25th anniversary article: organic electronics marries photochromism: generation of multifunctional interfaces, materials, and devices. *Adv. Mater.*, 26(12):1827–1845, 2014.

[49] M. M. Russew and S. Hecht. Photoswitches: from molecules to materials. *Adv. Mater.*, 22(31):3348–3360, 2010.

[50] G. Pace, V. Ferri, C. Grave, M. Elbing, C. von Hanisch, M. Zharnikov, M. Mayor, M. A. Rampi, and P. Samori. Cooperative light-induced molecular movements of highly ordered azobenzene self-assembled monolayers. *Proc. Nat. Acad. Sci.*, 104(24):9937–9942, 2007.

[51] N. Crivillers, A. Liscio, F. Di Stasio, C. Van Dyck, S. Osella, D. Cornil, S. Mian, G. M. Lazzerini, O. Fenwick, E. Orgiu, F. Reinders, S. Braun, M. Fahlman, M. Mayor, J. Cornil, V. Palermo, F. Cacialli, and P. Samori. Photoinduced work function changes by isomerization of a densely packed azobenzene-based sam on au: a joint experimental and theoretical study. *Phys. Chem. Chem. Phys.*, 13(32):14302–14310, 2011.

[52] J. M. Mativetsky, G. Pace, M. Elbing, M. A. Rampi, M. Mayor, and P. Samori. Azobenzenes as light-controlled molecular electronic switches in nanoscale metal-molecule-metal junctions. *J. Am. Chem. Soc.*, 130(29): 9192–9193, 2008.

[53] N. Crivillers, E. Orgiu, F. Reinders, M. Mayor, and P. Samori. Optical modulation of the charge injection in an organic field-effect transistor based on photochromic self-assembled-monolayer-functionalized electrodes. *Adv. Mater.*, 23(12):1447–1452, 2011.

[54] V. Faramarzi, C. Raimondo, F. Reinders, M. Mayor, P. Samori, and B. Doudin. Optically switchable molecular device using microsphere based junctions. *Appl. Phys. Lett.*, 99(23):233104, 2011.

[55] V. Ferri, M. Elbing, G. Pace, M. D. Dickey, M. Zharnikov, P. Samori, M. Mayor, and M. A. Rampi. Light-powered electrical switch based on cargo-lifting azobenzene monolayers. *Angew. Chem. Int. Ed. Engl.*, 47(18): 3407–3409, 2008.

[56] M. Elbing, A. Blaszczyk, C. von Hänisch, M. Mayor, V. Ferri, C. Grave, M. A. Rampi, G. Pace, P. Samori, A. Shaporenko, and M. Zharnikov. Single component self-assembled monolayers of aromatic azo-biphenyl: Influence of the packing tightness on the sam structure and light-induced molecular movements. *Adv. Funct. Mater.*, 18(19):2972–2983, 2008.

[57] N. Heinemann, J. Grunau, T. Leißner, O. Andreyev, S. Kuhn, U. Jung, D. Zargarani, R. Herges, O. Magnussen, and M. Bauer. Reversible switching in self-assembled monolayers of azobenzene thiolates on au (111) probed by threshold photoemission. *Chem. Phys.*, 402:22–28, 2012.

[58] U. Jung, O. Filinova, S. Kuhn, D. Zargarani, C. Bornholdt, R. Herges, and O. Magnussen. Photoswitching behavior of azobenzene-containing alkanethiol self-assembled monolayers on au surfaces. *Langmuir*, 26(17):13913–13923, 2010.

[59] T. Weidner, F. Bretthauer, N. Ballav, H. Motschmann, H. Orendi, C. Bruhn, U. Siemeling, and M. Zharnikov. Correlation between the molecular structure and photoresponse in aliphatic self-assembled monolayers with azobenzene tailgroups. *Langmuir*, 24(20):11691–700, 2008.

[60] D. T. Valley, M. Onstott, S. Malyk, and A. V. Benderskii. Steric hindrance of photoswitching in self-assembled monolayers of azobenzene and alkane thiols. *Langmuir*, 29(37):11623–11631, 2013.

[61] T. Moldt, D. Brete, D. Przyrembel, S. Das, J. R. Goldman, P. K. Kundu, C. Gahl, R. Klajn, and M. Weinelt. Tailoring the properties of surface-immobilized azobenzenes by monolayer dilution and surface curvature. *Langmuir*, 31(3):1048–1057, 2015.

[62] G. K. Joshi, K. N. Blodgett, B. B. Muhoberac, M. A. Johnson, K. A. Smith, and R. Sardar. Ultrasensitive photoreversible molecular sensors of azobenzene-functionalized plasmonic nanoantennas. *Nano Lett.*, 14(2):532–540, 2014.

[63] Y. B. Zheng, J. L. Payton, C. H. Chung, R. Liu, S. Cheunkar, B. K. Pathem, Y. Yang, L. Jensen, and P. S. Weiss. Surface-enhanced raman spectroscopy to probe reversibly photoswitchable azobenzene in controlled nanoscale environments. *Nano Lett.*, 11(8):3447–3452, 2011.

[64] U. Jung, B. Baisch, D. Kaminski, K. Krug, A. Elsen, T. Weineisen, D. Raffa, J. Stettner, C. Bornholdt, R. Herges, and O. Magnussen. Structure and redox behavior of azobenzene-containing monolayers on au(111): A combined stm, x-ray reflectivity, and voltammetry study. *J. Electroanal. Chem.*, 619-620: 152–158, 2008.

[65] W. Azzam, P. Cyganik, G. Witte, M. Buck, and C. Wöll. Pronounced odd-even changes in the molecular arrangement and packing density of biphenyl-based thiol sams: A combined stm and leed study. *Langmuir*, 19(20):8262–8270, 2003.

[66] P. Cyganik, M. Buck, W. Azzam, and C. Wöll. Self-assembled monolayers of ω-biphenylalkanethiols on au(111): Influence of spacer chain on molecular packing. *J. Phys. Chem. B*, 108(16):4989–4996, 2004.

[67] K. Heister, M. Zharnikov, M. Grunze, and L. S. O. Johansson. Adsorption of alkanethiols and biphenylthiols on au and ag substrates - a high resolution x-ray photoelectron spectroscopy study. *J. Phys. Chem. B*, 105(19):4058–4061, 2001.

[68] K. Heister, M. Zharnikov, M. Grunze, L. S. O. Johansson, and A. Ulman. Characterization of x-ray induced damage in alkanethiolate monolayers by high-resolution photoelectron spectroscopy. *Langmuir*, 17(1):8–11, 2001.

[69] H. T. Rong, S. Frey, Y.-J. Yang, M. Zharnikov, M. Buck, M. Wühn, Ch. Wöll, and G. Helmchen. On the importance of the head group substrate bond in thiol monolayers: A study of biphenyl based thiols on gold and silver. *Langmuir*, 17(5):1582–1593, 2001.

[70] I. Thom and M. Buck. Electrochemical stability of self-assembled monolayers of biphenyl based thiols studied by cyclic voltammetry and second harmonic generation. *Surf. Sci.*, 581(1):33–46, 2005.

[71] F. Vervaecke, S. Wyczawska, P. Cyganik, J. Bastiaansen, Z. Postawa, R. E. Silverans, E. Vandeweert, and P. Lievens. Odd-even effects in ion-beam-induced desorption of biphenyl-substituted alkanethiol self-assembled monolayers. *ChemPhysChem*, 12(1):140–144, 2011.

[72] T. Felgenhauer, H. T. Rong, and M. Buck. Electrochemical and exchange studies of self-assembled monolayers of biphenyl based thiols on gold. *J. Electroanal. Chem.*, 550-551:309–319, 2003.

[73] K. Szelagowska-Kunstman, P. Cyganik, B. Schüpbach, and A. Terfort. Relative stability of thiol and selenol based sams on au(111) - exchange experiments. *Phys. Chem. Chem. Phys.*, 12(17):4400–4406, 2010.

[74] P. Cyganik and M. Buck. Polymorphism in biphenyl-based self-assembled monolayers of thiols. *J. Am. Chem. Soc.*, 126(19):5960–5961, 2004.

[75] P. Cyganik, M. Buck, T. Strunskus, A. Shaporenko, J. D. Wilton-Ely, M. Zharnikov, and C. Woll. Competition as a design concept: polymorphism in self-assembled monolayers of biphenyl-based thiols. *J. Am. Chem. Soc.*, 128(42):13868–13878, 2006.

[76] P. Cyganik, M. Buck, T. Strunskus, A. Shaporenko, G. Witte, M. Zharnikov, and C. Woll. Influence of molecular structure on phase transitions: A study of self-assembled monolayers of 2-(aryl)-ethane thiols. *J. Phys. Chem. C*, 111(45):16909–16919, 2007.

[77] M. Dendzik, A. Terfort, and P. Cyganik. Odd–even effect in the polymorphism of self-assembled monolayers of biphenyl-substituted alkaneselenolates on au(111). *J. Phys. Chem. C*, 116(36):19535–19542, 2012.

[78] R. Bock. *Nachweis- und Bestimmungsmethoden*, volume 2, book section 3.9.4. Verlag Chemie, Weinheim, 1984.

[79] T. A. Carlson. *Photoelectron and Auger Spectroscopy.* Plenum Press, New York, 1955.

[80] N. Martensson and A. Nilsson. On the origin of core-level binding energy shifts. *Journal of Electron Spectroscopy and Related Phenomena*, 75:209–223, 1995.

[81] P. H. Citrin, G. K. Wertheim, and Y. Baer. Core-level binding energy and density of states from the surface atoms of gold. *Phys. Rev. Lett.*, 41(20): 1425–1428, 1978.

[82] D. A. Shirley. High-resolution x-ray photoemission spectrum of the valence bands of gold. *Phys. Rev. B*, 5(12):4709–4714, 1972.

[83] S. Tanuma, C. J. Powell, and D. R. Penn. Calculations of electron inelastic mean free paths (imfps). iv. evaluation of calculated imfps and of the predictive imfp formula tpp-2 for electron energies between 50 and 2000 ev. *Surf. Interface Anal.*, 20(1):77–89, 1993.

[84] A. Jablonski. The electron attenuation length revisited. *Surface Science Reports*, 47(2-3):33–91, 2002.

[85] C. L. A. Lamont and J. Wilkes. Attenuation length of electrons in self-assembled monolayers of n-alkanethiols on gold. *Langmuir*, 15(6):2037–2042, 1999.

[86] P. E. Laibinis, C. D. Bain, and G. M. Whitesides. Attenuation of photoelectrons in monolayers of n-alkanethiols adsorbed on copper, silver, and gold. *J. Phys. Chem.*, 95(18):7017–7021, 1991.

[87] E. Cartier, P. Pfluger, J. J. Pireaux, and M. Rei Vilar. Mean-free paths and scattering processes for 0.1-4500 ev electrons in saturated hydrocarbon films. *Appl. Phys. A*, 44(1):43–53, 1987.

[88] J. Thome, M. Himmelhaus, M. Zharnikov, and M. Grunze. Increased lateral density in alkanethiolate films on gold by mercury adsorption. *Langmuir*, 14 (26):7435–7449, 1998.

[89] J. Stöhr. *NEXAFS Spectroscopy*, volume 25 of *Springer Series in Surface Science*. Springer-Verlag: Berlin, Germany, 1992. ISBN 978-3540544227.

[90] M. Piantek, J. Miguel, M. Bernien, C. Navío, A. Krüger, B. Priewisch, K. Rück-Braun, and W. Kuch. Adsorption of carboxymethylester-azobenzene on copper and gold single crystal surfaces. *Appl. Phys. A*, 93(2): 261–266, 2008.

[91] M. Ohno. Deexcitation processes in adsorbates. *Phys. Rev. B*, 50(4):2566–2575, 1994.

[92] O. Björneholm, A. Nilsson, E. O. F. Zdansky, A. Sandell, B. Hernnäs, H. Tillborg, J. N. Andersen, and N. Martensson. 2π-resonance broadening in x-ray-absorption spectroscopy of adsorbed co. *Phys. Rev. B*, 46(16):10353–10365, 1992.

[93] P. S. Bagus, K. Weiss, A. Schertel, Ch Wöll, W. Braun, C. Hellwig, and C. Jung. Identification of transitions into rydberg states in the x-ray absorption spectra of condensed long-chain alkanes. *Chem. Phys. Lett.*, 248 (3-4):129–135, 1996.

[94] N. Ballav, B. Schüpbach, O. Dethloff, P. Feulner, A. Terfort, and M. Zharnikov. Direct probing molecular twist and tilt in aromatic self-assembled monolayers. *J. Am. Chem. Soc.*, 129(50):15416–15417, 2007.

[95] V. Palermo, M. Palma, and P. Samori. Electronic characterization of organic thin films by kelvin probe force microscopy. *Adv. Mater.*, 18(2):145–164, 2006.

[96] F. Schreiber. Structure and growth of self-assembling monolayers. *Prog. Surf. Sci.*, 65(5-8):151–256, 2000.

[97] F. Schreiber. Organic molecular beam deposition: Growth studies beyond the first monolayer. *physica status solidi (a)*, 201(6):1037–1054, 2004.

[98] A. Ulman. Formation and structure of self-assembled monolayers. *Chem. Rev.*, 96:1533–1554, 1996.

[99] M. Mrksich and G. M. Whitesides. Using self-assembled monolayers to understand the interactions of man-made surfaces with proteins and cells. *Annu. Rev. Biophys. Biomol. Struct.*, 25:55–78, 1996.

[100] J. Sagiv. Organized monolayers by adsorption, i. formation and structure of oleophobic mixed monolayers on solid surfaces. *J. Am. Chem. Soc.*, 102(1): 92–98, 1980.

[101] X. Torrelles, E. Barrena, C. Munuera, J. Rius, S. Ferrer, and C. Ocal. New insights in the c(4x2) reconstruction of hexadecanethiol on au(111) revealed by grazing incidence x-ray diffraction. *Langmuir*, 20:9396–9402, 2004.

[102] F. Schreiber, A. Eberhardt, T. Y. B. Leung, P. Schwartz, S. M. Wetterer, D. J. Lavrich, L. Berman, P. Fenter, P. Eisenberger, and G. Scoles. Adsorption mechanisms, structures, and growth regimes of an archetypal self-assembling system - decanethiol on au(111). *Phys. Rev. B*, 57(19):12476–12481, 1998.

[103] N. Camillone, T. Y. B. Leung, P. Schwartz, P. Eisenberger, and G. Scoles. Chain length dependence of the striped phases of alkanethiol monolayers self-assembled on au(111): An atomic beam diffraction study. *Langmuir*, 12: 2737–2746, 1996.

[104] N. Camillone, P. Eisenberger, T. Y. B. Leung, P. Schwartz, G. Scoles, G. E. Poirier, and M. J. Tarlov. New monolayer phases of n-alkane thiols self-assembled on au(111): Preparation, surface characterization, and imaging. *J. Chem. Phys.*, 101(12):11031, 1994.

[105] P. Fenter, A. Eberhardt, and P. Eisenberger. Self-assembly of n-alkyl thiols as disulfides on au(111). *Science*, 266:1216–1218, 1994.

[106] P. Fenter, P. Eisenberger, and K. Liang. Chain-length dependence of the structures and phases of ch3(ch2)n-1 sh self-assembled on au(111). *Phys. Rev. Lett.*, 70(16):2447–2450, 1993.

[107] F. Tao and S. L. Bernasek. Understanding odd-even effects in organic self-assembled monolayers. *Chem. Rev.*, 107(5):1408–1453, 2007.

[108] T. Abu-Husein, S. Schuster, D. A. Egger, M. Kind, T. Santowski, A. Wiesner, R. Chiechi, E. Zojer, A. Terfort, and M. Zharnikov. The effects of embedded dipoles in aromatic self-assembled monolayers. *Adv. Funct. Mater.*, 25(25):3943–3957, 2015.

[109] H. J. Himmel, A. Terfort, and C. Wöll. Fabrication of a carboxyl-terminated organic surface with self-assembly of functionalized terphenylthiols: The importance of hydrogen bond formation. *J. Am. Chem. Soc.*, 120(46):12069–12074, 1998.

[110] B. Schüpbach and A. Terfort. A divergent synthesis of oligoarylalkanethiols with lewis-basic n-donor termini. *Org. Biomol. Chem.*, 8(15):3552–3562, 2010.

[111] K. T. Wong, T. S. Hung, Y. Lin, C. C. Wu, G. H. Lee, S. M. Peng, C. H. Chou, and Y. O. Su. Suzuki coupling approach for the synthesis of phenylene-pyrimidine alternating oligomers for blue light-emitting material. *Org. Lett.*, 4(4):513–516, 2002.

[112] M. Colombo, M. Giglio, and I. Peretto. Simple microwave-assisted ligand-free suzuki cross-coupling: Functionalization of halo-pyrimidine moieties. *J. Heterocycl. Chem.*, 45(4):1077–1081, 2008.

[113] M. Zharnikov. High-resolution x-ray photoelectron spectroscopy in studies of self-assembled organic monolayer. *J. Electron. Spectr. Relat. Phenom.*, 178-179:380–393, 2010.

[114] J.F. Moulder and J. Chastain. *Handbook of X-ray Photoelectron Spectroscopy: A Reference Book of Standard Spectra for Identification and Interpretation of XPS Data*. Physical Electronics Division, Perkin-Elmer Corporation, 1992.

[115] J. F. Moulder, W. E. Stickle, P. E. Sobol, and K. D. Bomben. *Handbook of X-ray Photoelectron Spectroscopy*. Perkin-Elmer Corp.: Eden Prairie, MN, 1992.

[116] H. A. Biebuyck, C. D. Bain, and G. M. Whitesides. Comparison of organic molecules on polycrystalline gold spontaneously assembled from solutions containing dialkyl disulfides or alkanethiols. *Langmuir*, 10(12):1825–1831, 1994.

[117] F. Chesneau, B. Schüpbach, K. Szelagowska-Kunstman, N. Ballav, P. Cyganik, A. Terfort, and M. Zharnikov. Self-assembled monolayers of perfluoroterphenyl-substituted alkanethiols: Specific characteristics and odd-even effects. *Phys. Chem. Chem. Phys.*, 12(38):12123–12127, 2010.

[118] H. Hamoudi, K. Döring, F. Chesneau, H. Lang, and M. Zharnikov. Self-assembly of pyridine-substituted alkanethiols on gold: the electronic structure puzzle in the ortho- and para-attachment of pyridine to the molecular chain. *J. Phys. Chem. C*, 116(1):861–870, 2012.

[119] F. Chesneau, J. L. Zhao, C. Shen, M. Buck, and M. Zharnikov. Adsorption of long-chain alkanethiols on au(111): A look from the substrate by high resolution x-ray photoelectron spectroscopy. *J. Phys. Chem. C*, 114(15):7112–7119, 2010.

[120] P. E. Batson. Carbon-1s near-edge-absorption fine-structure in graphite. *Phys. Rev. B*, 48(4):2608–2610, 1993.

[121] M. Domke, T. Mandel, A. Puschmann, C. Xue, D. A. Shirley, G. Kaindl, H. Petersen, and P. Kuske. Performance of the high-resolution sx700/ii monochromator. *Rev. Sci. Instrum.*, 63(1):80–89, 1992.

[122] A. Natan, L. Kronik, H. Haick, and R. T. Tung. Electrostatic properties of ideal and non-ideal polar organic monolayers: Implications for electronic devices. *Adv. Mater.*, 19(23):4103–4117, 2007.

[123] P. E. Laibinis, G. M. Whitesides, D. L. Allara, Y. T. Tao, A. N. Parikh, and R. G. Nuzzo. Comparison of the structures and wetting properties of self-assembled monolayers of n-alkanethiols on the coinage metal surfaces, copper, silver, and gold. *J. Am. Chem. Soc.*, 113(19):7152–7167, 1991.

[124] M. Zharnikov and M. Grunze. Spectroscopic characterization of thiol-derived self-assembled monolayers. *J. Phys.: Condens. Matter*, 13(49):11333–11365, 2001.

[125] J. A. Horsley, J. Stöhr, A. P. Hitchcock, D. C. Newbury, A. L. Johnson, and F. Sette. Resonances in the k-shell excitation spectra of benzene and pyridine: Gas phase, solid and chemisorbed states. *J. Chem. Phys.*, 83(12): 6099–6107, 1985.

[126] T. Yokoyama, K. Seki, I. Morisada, K. Edamatsu, and T. Ohta. X-ray absorption spectra of poly-p-phenylenes and polyacenes: Localization of p* orbitals. *Phys. Scr.*, 41(1):189–192, 1990.

[127] S. Frey, V. Stadler, K. Heister, W. Eck, M. Zharnikov, M. Grunze, B. Zeysing, and A. Terfort. Structure of thioaromatic self-assembled monolayers on gold and silver. *Langmuir*, 17(8):2408–2415, 2001.

[128] P. Bolognesi, P. O'Keeffe, V. Feyer, O. Plekan, K. Prince, M. Coreno, G. Mattioli, A. Amore Bonapasta, W. Zhang, V. Carravetta, Y. Ovcharenko, and L. Avaldi. Inner shell excitation, ionization and fragmentation of pyrimidine. *J. Phys.: Confer. Ser.*, 212(1):012002, 2010.

[129] P. Bolognesi, P. O'Keeffe, Y. Ovcharenko, M. Coreno, L. Avaldi, V. Feyer, O. Plekan, K. C. Prince, W. Zhang, and V. Carravetta. Pyrimidine and halogenated pyrimidines near edge x-ray absorption fine structure spectra at c and n k-edges: experiment and theory. *J. Chem. Phys.*, 133(3):034302, 2010.

[130] M. Zharnikov, A. Küller, A. Shaporenko, E. Schmidt, and W. Eck. Aromatic self-assembled monolayers on hydrogenated silicon. *Langmuir*, 19(11):4682–4687, 2003.

[131] H. M. Rietvield, E. N. Maslen, and C. J. B. Clews. An x-ray and neutron diffraction refinement of the structure of p-terphenyl. *Acta Cryst.*, B26(6): 693–706, 1970.

[132] O. Bastiansen. The molecular structure of biphenyl and some of its derivatives. *Acta Chem. Scand.*, 3(4):408–414, 1949.

[133] A. Almenningen, O. Bastiansen, L. Fernholt, B. N. Cyvin, S. J. Cyvin, and S. Samdal. Structure and barrier of internal rotation of biphenyl derivatives in the gaseous state: Part 1. the molecular structure and normal coordinate analysis of normal biphenyl and pedeuterated biphenyl. *J. Mol. Struct.*, 128 (1-3):59–76, 1985.

[134] P. J. L. Baudour, Y. Delugeard, and H. Cailleau. Transition structurale dans les polyphényles. i. structure cristalline de la phase basse température du p-terphényle à 113 k. *Acta Cryst.*, B32(1):150–154, 1976.

[135] H. Cailleau, J. L. Baudour, J. Meinnel, A. Dworkin, Moussa F., and C. M. E. Zeyen. Double-well potentials and structural phase transitions in polyphenyls. *Faraday Discuss. Chem. Soc.*, 69:7–18, 1980.

[136] P. Bordat and R. Brown. A molecular model of p-terphenyl and its disorder-order transition. *Chem. Phys.*, 246(1-3):323–334, 1999.

[137] A. Shaporenko, M. Elbing, A. Blaszczyk, C. von Hanisch, M. Mayor, and M. Zharnikov. Self-assembled monolayers from biphenyldithiol derivatives: Optimization of the deprotection procedure and effect of the molecular conformataion. *J. Phys. Chem. B*, 110(9):4307–4317, 2006.

[138] J. Liu, B. Schüpbach, A. Bashir, O. Shekhah, A. Nefedov, M. Kind, A. Terfort, and C. Wöll. Structural characterization of self-assembled monolayers of pyridine-terminated thiolates on gold. *Phys. Chem. Chem. Phys.*, 12(17): 4459–4472, 2010.

[139] A. Shaporenko, M. Brunnbauer, A. Terfort, L. S. Johansson, M. Grunze, and M. Zharnikov. Odd-even effects in photoemission from terphenyl-substituted alkanethiolate self-assembled monolayers. *Langmuir*, 21(10): 4370–4375, 2005.

[140] D. Briggs and M. P. Seah. *Practical Surface Analysis by Auger and X-ray Photoelectron Spectroscopy.* John Wiley, Chichester, 2nd edition, 1990.

[141] L. Kong, F. Chesneau, Z. Zhang, F. Staier, A. Terfort, P. A. Dowben, and M. Zharnikov. Electronic structure of aromatic monomolecular films: The

effect of molecular spacers and interfacial dipoles. *J. Phys. Chem. C*, 115 (45):22422–22428, 2011.

[142] J. B. Neaton, M. S. Hybertsen, and S. G. Louie. Renormalization of molecular electronic levels at metal-molecule interfaces. *Phys. Rev. Lett.*, 97(21): 216405, 2006.

[143] D. A. Egger, Z. F. Liu, J. B. Neaton, and L. Kronik. Reliable energy level alignment at physisorbed molecule-metal interfaces from density functional theory. *Nano Lett.*, 15(4):2448–2455, 2015.

[144] P. Puschnig, C. Ambrosch-Draxl, G. Heimel, E. Zojer, R. Resel, G. Leising, M. Kriechbaum, and W. Graupner. Pressure studies on the intermolecular interactions in biphenyl. *Synth. Met.*, 116(1-3):327–331, 2001.

[145] H. Kondoh, M. Iwasaki, T. Shimada, K. Amemiya, T. Yokoyama, T. Ohta, M. Shimomura, and S. Kono. Adsorption of thiolates to singly coordinated sites on au(111) evidenced by photoelectron diffraction. *Phys. Rev. Lett.*, 90 (6):066102, 2003.

[146] M. G. Roper, M. P. Skegg, C. J. Fisher, J. J. Lee, V. R. Dhanak, D. P. Woodruff, and R. G. Jones. Atop adsorption site of sulphur head groups in gold-thiolate self-assembled monolayers. *Chem. Phys. Lett.*, 389(1-3):87–91, 2004.

[147] J. Hautman, J. P. Bareman, W. Mar, and M. L. Klein. Molecular-dynamics investigations of self-assembled monolayers. *J. Chem. Soc.,Faraday Trans.*, 87(13):2031–2037, 1991.

[148] S. Frey, A. Shaporenko, M. Zharnikov, P. Harder, and D. L. Allara. Self-assembled monolayers of nitrile-functionalized alkanethiols on gold and silver substrates. *J. Phys. Chem. B*, 107(31):7716–7725, 2003.

[149] A. Natan, Y. Zidon, Y. Shapira, and L. Kronik. Cooperative effects and dipole formation at semiconductor and self-assembled-monolayer interfaces. *Phys. Rev. B*, 73(19):193310, 2006.

[150] D. Cornil, Y. Olivier, V. Geskin, and J. Cornil. Depolarization effects in self-assembled monolayers: A quantum-chemical insight. *Adv. Funct. Mater.*, 17 (7):1143–1148, 2007.

[151] M. L. Sushko and A. L. Shluger. Intramolecular dipole coupling and depolarization in self-assembled monolayers. *Adv. Funct. Mater.*, 18(15):2228–2236, 2008.

[152] L. Wang, G. M. Rangger, L. Romaner, G. Heimel, T. Bucko, Z. Y. Ma, Q. K. Li, Z. Shuai, and E. Zojer. Electronic structure of self-assembled monolayers on au(111) surfaces: The impact of backbone polarizability. *Adv. Funct. Mater.*, 19(23):3766–3775, 2009.

[153] A. L. Hickey and C. N. Rowley. Benchmarking quantum chemical methods for the calculation of molecular dipole moments and polarizabilities. *J. Phys. Chem. A*, 118(20):3678–3687, 2014.

[154] P. Kao, S. Neppl, P. Feulner, D. L. Allara, and M. Zharnikov. Charge transfer time in alkanethiolate self-assembled monolayers via resonant auger electron spectroscopy. *J. Phys. Chem. C*, 114(32):13766–13773, 2010.

[155] H. Hamoudi, S. Neppl, P. Kao, B. Schüpbach, P. Feulner, A. Terfort, D. L. Allara, and M. Zharnikov. Orbital-dependent charge transfer dynamics in conjugated self-assembled monolayers. *Phys. Rev. Lett.*, 107(2):027801, 2011.

[156] E. Ludwig, T. Strunskus, S. Hellmann, A. Nefedov, C. Woll, L. Kipp, and K. Rossnagel. Electronic structure, adsorption geometry, and photoswitchability of azobenzene layers adsorbed on layered crystals. *Phys. Chem. Chem. Phys.*, 15(46):20272–20280, 2013.

[157] C. Gahl, R. Schmidt, D. Brete, E. R. McNellis, W. Freyer, R. Carley, K. Reuter, and M. Weinelt. Structure and excitonic coupling in self-assembled monolayers of azobenzene-functionalized alkanethiols. *J. Am. Chem. Soc.*, 132(6):1831–1838, 2010.

[158] D. Brete, D. Przyrembel, C. Eickhoff, R. Carley, W. Freyer, K. Reuter, C. Gahl, and M. Weinelt. Mixed self-assembled monolayers of azobenzene photoswitches with trifluoromethyl and cyano end groups. *J. Phys. Condens. Matter*, 24(39):394015, 2012.

[159] R. Schmidt, S. Hagen, D. Brete, R. Carley, C. Gahl, J. Dokic, P. Saalfrank, S. Hecht, P. Tegeder, and M. Weinelt. On the electronic and geometrical structure of the trans- and cis-isomer of tetra-tert-butyl-azobenzene on au(111). *Phys. Chem. Chem. Phys.*, 12(17):4488–4497, 2010.

[160] J. F. Kang, A. Ulman, S. Liao, and R. Jordan. Mixed self-assembled monolayers of highly polar rigid biphenyl thiols. *Langmuir*, 15(6):2095–2098, 1999.

[161] J. Trotter. The crystal and molecular structure of biphenyl. *Acta Cryst.*, 14 (11):1135–1140, 1961.

[162] D. Gnatek, S. Schuster, J. Ossowski, M. Khan, J. Rysz, S. Krakert, A. Terfort, M. Zharnikov, and P. Cyganik. Odd-even effects in the structure and stability of azobenzene-substituted alkanethiolates on gold and silver substrates. *J. Phys. Chem.*, submitted, 2015.

[163] T. Nagahiro, H. Akiyama, M. Hara, and K. Tamada. Photoisomerization of azobenzene containing self-assembled monolayers investigated by kelvin probe work function measurements. *J. Electron. Spectr. Relat. Phenom.*, 172 (1-3):128–133, 2009.

[164] L. F. N. Ah Qune, H. Akiyama, T. Nagahiro, K. Tamada, and A. T. S. Wee. Reversible work function changes induced by photoisomerization of asymmetric azobenzene dithiol self-assembled monolayers on gold. *Appl. Phys. Lett.*, 93(8):083109, 2008.

[165] B. Kretz, D. A. Egger, and E. Zojer. A toolbox for controlling the energetics and localization of electronic states in self-assembled organic monolayers. *Advanced Science*, 2(3):1–9, 2015.

Acknowledgements

I would like to express my special appreciation and thanks to my advisor Professor Dr. Michael Zharnikov, he has been a tremendous mentor for me. I would like to thank him for encouraging my research and for allowing me to grow as a research scientist. His advice on both research as well as on my career have been priceless.

I would like to thank our partners for the synthesis of the SAM precursors as well for the experimental and theoretical work relevant for this thesis. Following persons should be acknowledged in this context:
Iris Hehn, Dr. David A. Egger, Prof. Dr. Egbert Zojer (Graz Technical University), Nichole Sullivan, Dr. Orlando Cabarcos and Prof. David L. Allara (Pennsylvania State University), Prof. Jean-François Morin (Laval University), Dominika Gnatek, Jakub Ossowski, Jakub Rysz and Dr. habil. Piotr Cyganik (Jagiellonian University), Dr. Martin Kind, Tarek Abu-Husein, Dr. Simone Krakert and Prof. Dr. Andreas Terfort (Frankfurt University).

A special thanks goes to our technical staff, viz. Reinhold Jehle, Günther Meinusch and Peter Jeschka for always supporting me when help was needed.

I would also like to thank our group members and office mates for their support and productive scientific discussions, in particular Dr. Mustafa Sayin, Tobias Wächter, Can Yildirim, Dr. Musammir Khan and André Brink.

My thanks also go to Prof. Dr. Petra Tegeder for agreeing to be my second examiner.

Finally, I would like to thank my parents for their faith in me and supporting me all my life.